NTNU

Norwegian University of
Science and Technology

Evaluation of Welded Clad Pipe

Properties and Simulations

Andreas Utvær

Mechanical Engineering
Submission date: July 2017
Supervisor: Odd Magne Akselsen, MTP

Norwegian University of Science and Technology
Department of Mechanical and Industrial Engineering

Preface

This thesis is a result of my work in the course TMM4960 Engineering Design and Materials, Master's Thesis at the Department of Mechanical and Industrial Engineering, at the Norwegian University of Science and Technology (NTNU), Spring 2017.

I would like to thank my supervisors Prof. Odd Magne Akselsen at the Department of Mechanical and Industrial Engineering and Dr. Vigdis Olden at SINTEF for their valuable guidance through my work. I would also like to thank Vidar Osen at SINTEF for his help with my simulations. Finally I would like to give a special thanks to PhD candidate Lise Jemblie for her patience and valuable insight in my subject, and for always being available to answer my questions.

Andreas Utvær
Trondheim, Sunday 2nd July, 2017

Abstract

Pipelines are an essential part of the oil and gas offshore industry, for transporting unprocessed oil and gas from the seabed to the oil platform and to the mainland. The unprocessed oil and gas leaves a corrosive environment, which sets a demand for pipes with a corrosion resistant interior. Clad pipes meet this demand with a corrosion resistant, stainless steel interior and an outer carbon steel layer. There is of today no repair contingency for clad pipes. A knowledge basis needs to be established and the risk of hydrogen induced stress cracking (HISC) must be found.

This thesis work has been divided into two parts; One part working on experimentally testing of the triple point in welded clad pipes. Focused on fracture resistance curves, fracture toughness and crack path, with and without hydrogen present. The second part was focused on modelling a FE-model that was able to simulate crack propagation in clad pipe interface samples, experimentally tested by Jemblie [1]. Both with and without hydrogen present during testing.

Fracture mechanical testing of welded clad pipe C(T) samples have been successfully conducted, in air and under cathodic protection (CP). The samples with Ni-interlayer showed almost no reduction in fracture toughness from tests in air to tests under CP, with an average fracture toughness reduction of 0.13%. The small fracture toughness reduction may be explained by the crack path going into the Ni-interlayer which is not much susceptible to hydrogen embrittlement (HE). The samples without Ni-interlayer experienced a high decrease in fracture toughness tested under CP, with an average reduction in fracture toughness equal to 92%. The crack path in the samples without Ni-interlayer was examined in a light optical microscope (LOM). The test done in air showed a crack path shifting between the base material and the clad. The crack propagated mainly in the clad in the sample tested under CP. Not enough samples were tested to establish the fracture resistance curves for the samples without Ni-interlayer. A 2D FE-model with cohesive zone elements was successfully modelled. The FE-model was able to simulate crack propagation along the crack ligament, in a C(T) specimen, both with linear elastic and elastic-plastic materials. The FE-model was however not able to simulate the crack propagation observed in experimentally testing by Jemblie [1]. This was not possible due to numerical problems occurring after a few cohesive elements had failed, when using sufficiently high cohesive element parameter values.

For further work should more tests in both air and under CP be done on welded samples, with and without a Ni-interlayer. To establish the fracture resistance curves for both sample types. The microstructure on the samples without Ni-interlayer needs to be checked, to be sure that the samples are representative for welded clad pipes. The fractography must be studied and the cross section on multiply samples must be examined, on the samples without Ni-interlayer. To establish a more solid basis to explain the crack path and the hydrogen susceptibility on welded clad pipes. A deep root-cause investigation should be done on the FE-simulation, to explain and come up with a possible solution on the numerical crack propagation problem.

Abstract (Norwegian)

Rørledninger er en viktig del av olje- og gassindustrien, for å transportere ubearbeidet olje og gass fra havbunnen opp til oljeplattformen, og til fastlandet. Den ubehandlede olje og gassen etterlater et korrosivt miljø som stiller krav til rør med korrosjonsbestandig interiør. Clad rør møter denne etterspørselen med et korrosjonsbestandig, rustfritt stålinnredning og et ytre karbonstållag. Det er i dag ingen reparasjonsprosedyrer for cladrør. En kunnskapsbasis må etableres og risikoen for hydrogenindusert sprekking (HISC) må bli funnet.

Denne oppgaven var delt inn i to deler; En del med arbeid på eksperimentelt testing av trippelpunktet i sveisede clad-rør. Fokuset har vært på sprekkvekstkurver, bruddseighet og sprekkbane, med og uten hydrogen tilstede. Den andre delen var fokusert på å modellere en FE-modell som kunne simulere sprekkvekst i clad prøver, eksperimentelt testet av Jemblie [1]. Både med og uten hydrogen tilstede under testingen.

Bruddmekanisk testing av sveiste clad rør C(T) prøver har blitt gjennomført i luft og under katodisk beskyttelse (CP). Prøver med Ni-mellomlag viste nesten ingen reduksjon i bruddseighet fra tester i luft til tester under CP. Med en gjennomsnittlig bruddseighetsreduksjon på 0,13%. Den lave reduksjonen i bruddseighet kan forklares av sprekkbanen som går inn i Ni-mellomlaget, som ikke er mye utsatt for hydrogensprøhet (HE). Prøver uten Ni-mellomlag opplevde en høy reduksjon i bruddseighet, testet under CP sammenlignet med luft. Med en gjennomsnittlig reduksjon i bruddseighet lik 92%. Sprekkbanen i prøvene uten Ni-mellomlag ble undersøkt i et optisk lysmikroskop (LOM). Testen i luft viste en sprekkbane som skiftet mellom basematerialet og cladden. Sprekkbanen forplantet seg hovedsakelig i cladden i prøven under CP. Det ble ikke testet nok prøver for å kunne etablere sprekkvekstkurver, for prøvene uten Ni-mellomlag. En FE-modell med kohesive soneelementer ble vellykket modellert. FE-modellen kunne simulere sprekkutbredelse langs sprekk liagementen, i en C(T) prøve, både med lineære elastiske og elastisk-plastiske materialer. FE-modellen var imidlertid ikke i stand til å simulere sprekkutbredelsen observert i eksperimentelt testing av Jemblie [1]. Dette var ikke mulig på grunn av numeriske problemer som oppstod etter at noen kohesive elementer hadde blitt separert, ved bruk av tilstrekkelig høye kohesive sonelement parameterverdier.

For videre arbeid bør flere tester i både luft og under CP gjøres på sveisede prøver, med og uten et Ni-mellomlag. Dette bør gjøres for å etablere sprekkvekstkurver for begge prøvetyper. Mikrostrukturen på prøvene uten Ni-mellomlag bør kontrolleres, for å være sikker på at prøvene er representative for sveisede kledde rør. Fraktografien bør undersøkes, og tverrsnittet på flere prøver bør undersøkes, på prøvene uten Ni-mellomlag. Dette bør gjøres for å etablere et mer solid grunnlag for å forklare sprekkbanen og hydrogenens følsomhet på sveisede clad rør. En grundig undersøkelse bør gjøres på Femodellen for å kunne forklare og komme frem til en mulig løsning på det numeriske sprekkvekstproblemmet.

Contents

List of Figures

List of Tables

Nomenclature

Symbol	Description	Unit
HAZ	Heat affected zone	[-]
HE	Hydrogen Embrittlement	[-]
HISC	Hydrogen induced stress cracking	[-]
HEDE	Hydrogen enhanced decohesion model	[-]
HELP	Hydrogen enhance local plasticity	[-]
NILS	Normal interstitial lattice sites	[-]
BCC	Body centered cubic	[-]
FCC	Face centered cubic	[-]
CZM	Cohesive zone modelling	[-]
CZE	Cohesive zone elements	[-]
CMT	Cold metal transfer	[-]
CP	Cathodic protection	[-]
BM	Base material	[-]
FE	Finite element	[-]
C(T)	Compact tension	[-]
TSL	Traction separation law	[-]
LOM	Light optical microscope	[-]
SEM	Scanning electron microscope	[-]
LEFM	Linear elastic fracture mechanics	[-]
EPFM	Elastic-plastic fracture mechanics	[-]
SCE	saturated calomel electrode	[-]
CTOD	Crack tip opening displacement	[mm]
CMOD	Crack mouth opening displacement	[mm]

Symbol	Description	Unit
t	Geometrical cohesive element stiffness	[mm]
$g(a/W)$	load and geometry function	[-]
r_p	plastic rotational factor	[-]
m	constant dependent on stress state	[-]
ν	Poission‘s ratio	[-]
P	Applied load	[N]
P_{max}	Maximum load	[N]
P_{last}	Last logged load before experiment stop	[N]
E	Young‘s Modulus	[MPa]
E‘	Young‘s Modulus dependent on stress state	[MPa]
E_B	Trap binding energy	[Kj/mol]
K	Stress intensity factor	$[MPa\sqrt{mm}]$
K_I	Stress intensity factor in loading mode I	$[MPa\sqrt{mm}]$
K_e	Equilibrium constant	[-]
k	Stiffness of cohesive elements	[MPa]
k_i	Initial cohesive element stiffness	[MPa]
σ_{ys}	Yield strength	[MPa]
σ_u	Ultimate tensile strength	[MPa]
$\sigma(\delta)$	Cohesive strength	[MPa]
$\sigma_c(\theta_H)$	Crit. cohesive stress, hydrogen dependent	[MPa]
σ_c	Critical cohesive stress	[MPa]
δ	Cohesive element separation	[mm]
δ_c	Critical cohesive separation	[mm]
δ_{corr}	CTOD with stable crack growth	[mm]
δ_{el}	Elastic CTOD	[mm]
δ_p	Plastic CTOD	[mm]
δ_{corr}	CTOD, stable crack growth	[mm]
δ_{max}	CTOD at maximum load	[mm]
δ_{last}	CTOD at last logged load before exp. stop	[mm]
δ_{IC}	Fracture initiation toughness	[mm]
Γ_c	Total energy dissipation at fracture	$[J/m^2]$

Symbol	Description	Unit
ζ	Viscosity parameter	[-]
V_P	Plastic CMOD	[mm]
V_M	Molar volume of host lattice	$[mm^3/mol]$
$\bar{V}_H$	Partial molar volume of hydrogen	$[mm^3/mol]$
T	Temperature	[K]
C_L	Concentration of hydrogen in lattice cites	[ppm]
C_T	Concentration of hydrogen in traps	[ppm]
C_H	Total hydrogen concentration	[ppm]
C_{L0}	Initial hydrogen concentration	[ppm]
R	Gas constant	[J/(mol K)]
ΔG_b^0	Gibbs energy	$[Kj/mol]$
J	Flux diffusion	$[mol/m^2s]$
N_L	Number of lattice sites	$[m^{-3}]$
N_T	Number of trapping sies	$[m^{-3}$
D	Diffusion coefficient	$[m^2/s]$
D_L	Diffusivity	$[m^2/s]$
θ_L	Lattice cites occupied fraction	[-]
θ_L	Trap cites occupied fraction	[-]
θ_H	Total hydrogen coverage	[-]
Δa	Stable crack growth	[mm]

1. Introduction

1.1 Challenges and motivation

Pipelines are an essential part of the oil and gas offshore industry, for transporting unprocessed oil and gas from the seabed to the oil platform and to the mainland. The unprocessed oil and gas gives a corrosive environment that sets a demand for pipelines with a corrosion resistant interior, to avoid material degradation and leakages. Clad pipes meet this demand with a corrosion resistant interior, hereinafter called the clad, and an outer carbon steel layer, hereinafter called the base material. Clad pipes combines the corrosion resistance of stainless steels with the high mechanical strength of carbon steels. Clad pipes is also cost beneficial compared to manufacturing the entire pipe in a corrosion resistant material.

Despite the many advantages of clad pipes, it have some limitations due to the complexity that are presented as a result of the dissimilar materials. There is of today no repair contingency for clad pipes, so a knowledge basis must be established in order to maintain pipeline integrity. Welding of clad pipes may also result in a variety of complex microstructures that may be susceptible to cracking, as a result of different chemical compositions and thermal properties in the base material and clad. This may affect the integrity of the weld. The exterior of offshore clad pipelines are usually protected by coatings and cathodic protection (CP) through sacrificial anodes. The cathodic protection keeps the exterior of the pipeline protected from corrosion but exposes the pipeline to hydrogen. This sets the risk for hydrogen embrittlement (HE) which may lead to hydrogen induced stress cracking (HISC). How hydrogen embrittlement (HE) affects welded clad pipes is an important aspect that needs to be thoroughly studied to understand the risk of hydrogen induced stress cracking (HISC).

1.2 Previous work

Several projects have been completed on the clad pipe subject:

- Project report [2] and paper [3] on "Metallurgical Reactions in Welding of X60/X65 Clad Pipes" by Bjaaland.
- Master thesis on "Evaluation of Welded Clad Pipes - Microstructures and Properties" by Bjaaland [4].
- Paper on "Fracture Toughness and Hydrogen Embrittlement Susceptibility on the Interface of Clad Steel Pipes, with and without a Ni-interlayer" by Jemblie [1].
- Internship report on "Influence of Hydrogen Embrittlement on Welded Clad X60/65 Pipelines" by Degos [5].
- Paper on "Hydrogen Embrittlement Susceptibility of Clad Steel Pipes" by Jemblie [6].

Two main different types of clad pipes have been investigated by the different authors; One with a Ni-interlayer between the base material and the clad, and one without. Pure base material samples with and without Ni-interlayer have also been experimentally tested for comparison by Jemblie [6].

Bjaaland [2][3] measured microhardness on welded clad pipes and investigated the metallurgical changes in microhardness occurring during welding. She discovered a hard zone in the base material close to the interface, in the samples without Ni-interlayer. Cracks were also observed in the clad near the weld, propagating close to the clad-BM interface. No hard zone or cracks were observed in the samples without Ni-interlayer. Bjaaland [2][3] concluded that the hard zone found in the clad was caused by carbon diffusion from the base material and into the clad, which occurred mainly during production but to some extent also during welding. Bjaaland [2][3] assumed that the cracks in the clad was a result of the hard zone which would be more susceptible to cracking, but suggested that there also must be other reasons which are unproven. The Ni-interlayer seemed to have prevented the carbon diffusion, as no hard zone in the base material could be found in the samples with Ni-interlayer.

Bjaaland's master thesis [4] focused on characterization and fracture toughness of the dissimilar interface region between clad and base material. Carbides in the clad close to the interface were investigated. Cr_23C_6 carbides were found in the clad close to the interface. The dissimilar interface also revealed a lath-like structure, but no evidence of martensite were found. The samples without Ni-interlayer showed the highest fracture toughness, but a large reduction (77%) in fracture toughness occurred when hydrogen was present. Only a small reduction (7%) in fracture toughness in the samples with Ni-interlayer could be found, when subjected to hydrogen. Bjaaland concluded that only a small effect from hydrogen could be seen in the samples with Ni-interlayer because the crack propagated mainly along the Ni-interlayer, which is not much effected by hydrogen. An alternating crack path shifting between base material and the dissimilar interface were observed in the samples without Ni-interlayer, both in the presence of hydrogen and without.

A continuation of Bjaaland's work on the interface between clad and base material has been done by Jemblie [1]. Jemblie committed fracture mechanical testing in air and under cathodic protection (CP) to establish fracture resistance curves and find the associated fracture initiation toughness, with and without hydrogen present. Fracture mechanical tests were done for both types of clad pipes, with and without Ni-interlayer. The samples without Ni-interlayer showed a large (85%) reduction in the fracture initiation toughness when subjected to hydrogen. The samples with a Ni-interlayer showed only a small reduction in fracture initiation toughness (20%).

Degos [5] conducted fracture mechanical tests on welded clad samples to investigate the fracture toughness of the heat affected zone and the triple point (meeting point between weld material, base material and clad). A lowered fracture toughness was found compered to Bjaaland's [4] interface sample results. The samples with Ni-interlayer revealed only a small reduction in the fracture toughness subjected to hydrogen. The crack showed a similar path as Bjaaland's [4] samples, propagating through the Ni-interlayer. Unfortunately, pre-cracks in the clad were revealed in Degos samples without Ni-interlayer, so those results were deemed invalid.

A 2D C(T) FE-model has been developed by Jemblie [6], to simulate hydrogen embrittlement on clad pipes. The model is able to simulate crack initiation but the simulations stops due to numerical difficulties shortly after the maximum cohesive stress is reached. One reason for this might be the lack of a sharp crack, so the stress does not become high enough at the initiation cohesive element.

1.3 Problem Description

Despite that several projects have been completed on the clad pipe subject, there are still some crucial information missing. Pre-cracks were discovered in Degos [5] test samples without nickel inter-layer, which makes the tests conducted invalid. Fracture resistance curves for welded clad pipes with and without hydrogen influence are lacking. A FE-model that successfully capture the crack propagation occurring in the clad pipe C(T) samples have yet to be developed.

1.4 Project Scope

The main objectives of the current thesis are:

1. Modelling a 2D FE-model of a C(T) specimen with a sharp crack, to simulate crack propagation and hydrogen influence, with multiple materials inserted in the model.
2. Simulate the crack growth that has been experimentally studied by Jemblie [1][6] on the dissimilar material interface, without Ni-interlayer.
3. Conduct experimental tests on welded C(T) clad pipe samples, with and without Ni-interlayer, in both air and under cathodic protection (CP).
4. Establish fracture resistance curves for samples with Ni-interlayer, based on the experimental results.
5. Compare the fracture toughness results from both environments to evaluate welded clad pipes‘ susceptibility to hydrogen embrittlement (HE), with and without Ni-interlayer.
6. Investigate the crack path in welded clad pipe samples without Ni-interlayer, tested in both environments.
7. Compare the experimental results with previous results.

Degos [5] has already evaluated the hydrogen susceptibility on welded clad pipes with Ni-interlayer, based on fracture toughness results, but a second evaluation will be done as the fracture toughness values are given for ”free” when establishing fracture resistance curves.

1.5 Thesis Structure

Chapter 2 gives a brief summary of the background theory for the current thesis. Chapter 3 describes the materials used and the work done, before the results are presented in chapter 4. The results are discussed and concluded in chapter 5 and 6. Chapter 7 explains what more work needs to be done.

2. Theory

2.1 Clad pipes

A clad pipe is a composite pipe consisting of a thin inner Corrosion resistance alloy (CRA) plate (typically 3mm thick), from now on referred to as the clad, and an outer backing steel plate, from now on refereed to as the base material (BM) [7], see figure 2.1. The two plates are metallurgically bonded together. The base material does typically consist of a high strength carbon steel like X52, X60 or X65, while the clad typically consist of stainless steel like AISI 316L, 825 or 625, depending on the corrosive environment[8].

Clad pipes are made by clad plates that are bended into a pipe by a bending process and then longitudinally welded together [7][8]. There are many different ways to make clad plates. Roll bonding is the cheapest and most productive manufacturing process for large clad plates [9]. The roll bonding is done either by thermomechanical rolling with accelerated cooling, or hot rolling followed by quenching and tempering [8]. The sandwich method is usually used For clad plates thinner than 45 mm [8]. Two BM and two clad material plates are stacked on top of each other and kept together by a welding frame. Two clad plates are made simultaneously, separated by a ceramic powder to avoid unwanted metallurgical bond between the clad plates [8].

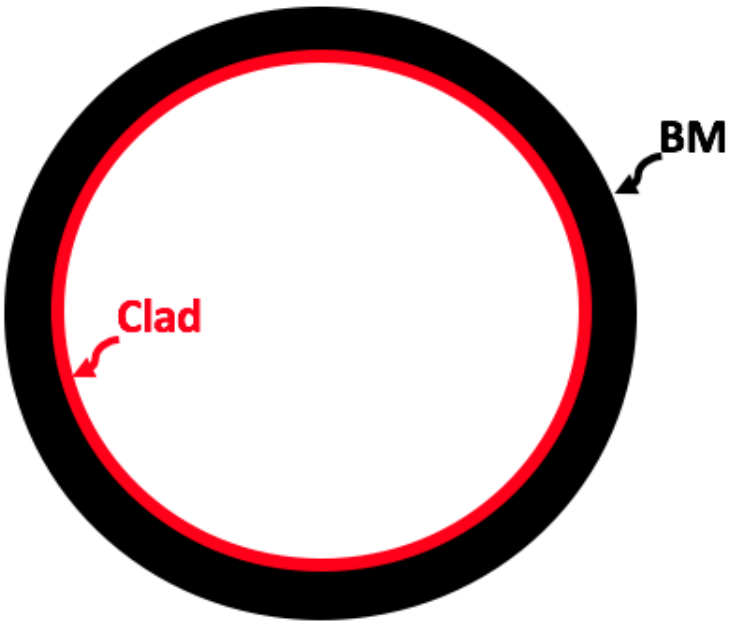

Figure 2.1: A clad pipe consists of an inner corrosion resistant material, referred to as the clad and an outer backing steel, referred to as the base material (BM), which are metallurgically bonded together.

2.2 The heat affected zone

Fusion welding joins materials by increasing the temperature of the materials up to their melting point. Additional metal commonly referred to as the filler metal, or the weld material which it is called in the current thesis, are added during the heating process. The filler material helps the bonding process between the materials. Welding on carbon steel causes a heat affected zone in the carbon steel, illustrated in figure 2.2, followed by a cooling sequence. The peak temperature decreases as the distance from the weld increases, which gives different zones with different properties and compositions. The grain growth zone, often called the coarse grained zone, is the zone which has the highest risk of metallurgical problems, and is therefore the zone which require the most attention. A microstructural change occur in the coarse grained zone, from ferrite to austenite during the heating process, followed by a transformation from austenite to martensite during the cooling sequence [10]. This leaves a microstructure with a local reduced fracture toughness and with an increased sensitivity to hydrogen embrittlement [10].

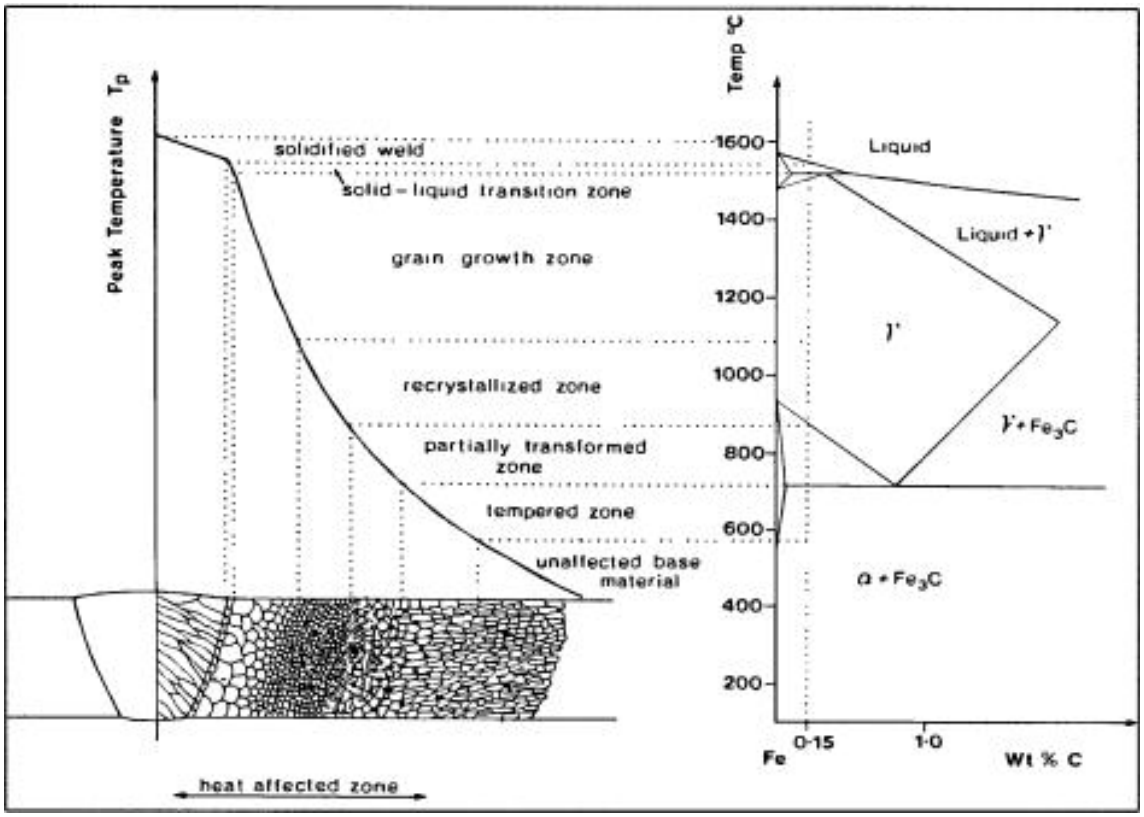

Figure 2.2: The heat affected zone in carbon steel [10].

2.3 Hydrogen Embrittlement

2.3.1 Introduction

Hydrogen is the smallest atom that exists and is quite small compared to metallic atoms. This makes hydrogen able to fit in interstitial sites in metallic crystals [11]. Hydrogen embrittlement (HE) is embrittlement of materials due to hydrogen influence, leading to a degradation of the material strength and fracture toughness. Hydrogen embrittlement inflicts all types of metals but some are more susceptible then others.

Hydrogen induced stress cracking (HISC) is a type of material failure caused by a combination of hydrogen and stress. There are three main elements that must be present simultaneously for HISC to occur:

1. Microstructure, A material with a microstructure susceptible to hydrogen.
2. Tensile stress, Internal or external tensile stress.
3. An environment containing hydrogen.

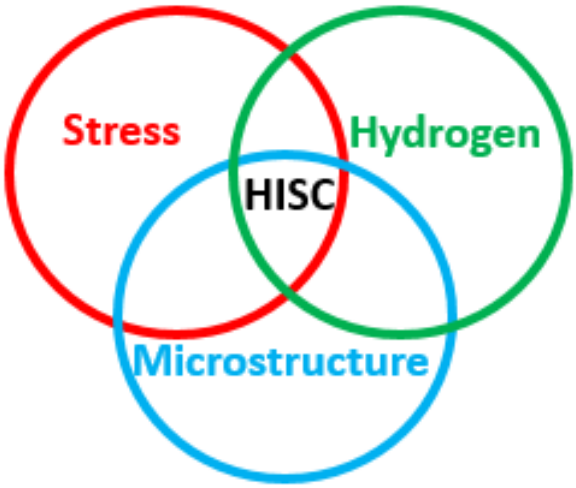

Figure 2.3: Three elements are needed simultaneously for HISC to occur.

2.3.2 Mechanism behind Hydrogen Embrittlement

The atomic mechanism behind HE has been largely researched. This research has lead to two major models that have gained the most recognition in the Scientific community, hydrogen enhanced decohesion model (HEDE) and the hydrogen enhanced local plasticity model (HELP).

Hydrogen Enhanced Decohesion Model (HEDE): The HEDE mechanism was originally proposed by Troiano [12] and further developed by Oriani [13] and Gererich [14]. HEDE propose that HE is caused by weakening of the atomic bonds by atomic discharging between the hydrogen and metal atoms [15]. This causes tensile separation of the metallic atoms (decohesion) to occur in preference to slip [16].

Hydrogen Enhanced Local Plasticity Model (HELP):
The HELP mechanism was first proposed by Birnbaum [17]. HELP proposes that HE occurs due to locally softening at the crack tip (where the hydro static stress is highest) which causes an increased dislocation motion in that area. This gives a local plasticity that results in cracking by micro void coalescence along the enhanced dislocation slip planes [18].

2.3.3 Hydrogen sources

The hydrogen may come from the external environment surrounding the metal like cathodic protection (CP), or it may come from within the metal itself, being introduced during manufacturing or maintenance, like welding.
Cathodic Protection (CP) is a technique used to protect a metal against corrosion by reducing its potential to the immune region of the Pourbaix diagram. This is done by adding an external current to the protected structure, either by an external power source or by a sacrificial anode [19].

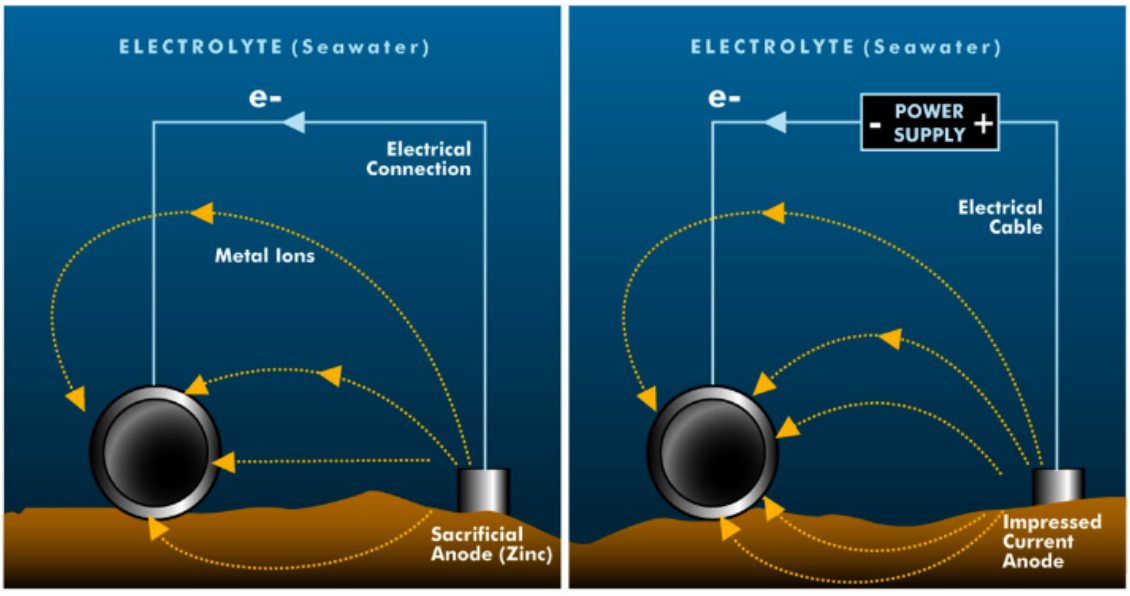

Figure 2.4: Illustration of the principle behind CP with sacrificial anode on the left and impressed current on the right [20].

Sacrificial anodes uses the principle of galvanic corrosion. This means that when materials with different electric potential are linked together in an electrolyte, the material with the lowest potential (less noble) will corrode faster and protect the material with the highest potential (more noble) [19] . As the sacrificial anode corrodes, a reduction process occurs at the protected metal surface, in the form of oxygen Eq. 2.1 and hydrogen reduction, Eq. 2.2 and 2.3 [21].

$$O_2 + 2H_2O + 4e^- \rightarrow 4OH^- \tag{2.1}$$

$$H_2O + e^- \rightarrow H_{ads} + OH^- \tag{2.2}$$

$$H^+_{aq} + e^- \rightarrow H_{ads} \tag{2.3}$$

This creates a film of hydrogen (adsorbed hydrogen) surrounding the protected metal.The adsorbed metal may then be absorbed by the metal through diffusion Eq. 2.4.

$$H_{ads} \rightarrow H_{abs} \tag{2.4}$$

The adsorbed hydrogen may also form hydrogen gas and leave the surface Eq. 2.5 and 2.6

$$H^+ + H_{ads} + e^- \rightarrow H_2 \tag{2.5}$$

$$H_2O + H_{ads} + e^- \rightarrow H_2 + OH^- \tag{2.6}$$

2.3.4 Hydrogen transport

For hydrogen embrittlement to occur, hydrogen must be present at the degradation sites in the metal. The transport to these sites are divided into two contributors, hydrogen diffusion and hydrogen trapping.

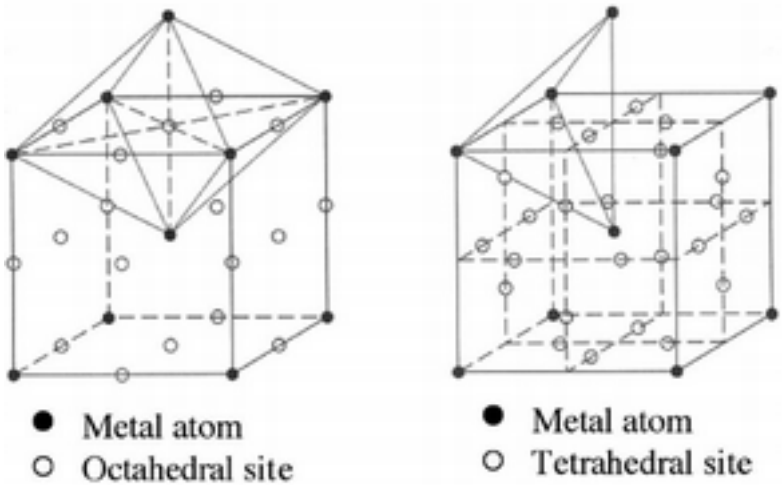

Figure 2.5: Interstitial lattice sites in BCC crystal structure [22].

The small size of hydrogen compared to the size of metallic atoms, makes hydrogen able to diffuse into interstitial sites in the metal lattice, as shown in figure 2.5 for BCC structure. The metal crystal structure are influential on how rapidly the hydrogen can diffuse through the metal. Hydrogen can diffuse faster through BCC then FCC structure, as BCC have a more open crystal structure.

The concentration of hydrogen in the normal interstitial lattice sites (NILS) is defined by the lattice concentration factor C_L. C_L can be expressed as[23]:

$$C_L = \beta \theta_L N_L \tag{2.7}$$

Where β is the number of solvent lattice volume, θ_L is the lattice site occupancy, meaning ratio between occupied lattice sites and the total number of sites, N_L is the density of the solvent lattice. N_L can be calculated by [23]:

$$N_L = \frac{N_A}{V_M} \tag{2.8}$$

Where N_A is the Avrogados number $6.0232 * 10^{23}$ atoms per mole and V_M is the molar volume of the host lattice.

Hydrogen may also be trapped in imperfections in the material, material traps. Typical traps are dislocations, vacancies, grain boundaries, phase boundaries, inclusions and precipitates. The material trap concentration, C_T can be calculated by [23]:

$$C_T = \alpha \theta_T N_T \tag{2.9}$$

Where α is the number of solvent lattice volume, θ_T is the trap site occupancy and N_T is the density of the

The concentrations C_T and C_L gives the total hydrogen concentration C_H:

$$C_H = C_L + C_T \tag{2.10}$$

Oriano [13] proposed an equilibrium between lattice and trapping concentrations which gives:

$$K_e = \frac{1-\theta_L}{\theta_L}\frac{\theta_T}{1-\theta_T} \tag{2.11}$$

Where k_e is the equilibrium constant.

K can also be expressed by the trap binding energy E_B [13]:

$$K = exp\left(\frac{-E_B}{RT}\right) \tag{2.12}$$

Combining Eq. 2.11 and 2.12 gives:

$$\frac{\theta_T}{1-\theta_T} = \frac{\theta_L}{1-\theta_L} exp\left(\frac{E_B}{RT}\right) \tag{2.13}$$

This gives the following relation between C_L and C_T:

$$C_T = \frac{KN_TC_L}{N_L + C_L(K-1)} \tag{2.14}$$

Traps decreases the amount of mobile hydrogen thus reduces the diffusivity and increases the local solubility of the system [24]. A special interest can be focused on dislocations as it could be viewed as moving traps dependent on plastic strain, while grain boundaries and vacancies remains constant. Sofronis and Mcmeeking [23] proposed a relationship between trap density, N_T and equivalent plastic strain $\bar{\varepsilon}^p$ near a blunting crack tip, shown in figure 2.6, based on Kummnic and Johnson‘s [25] results.

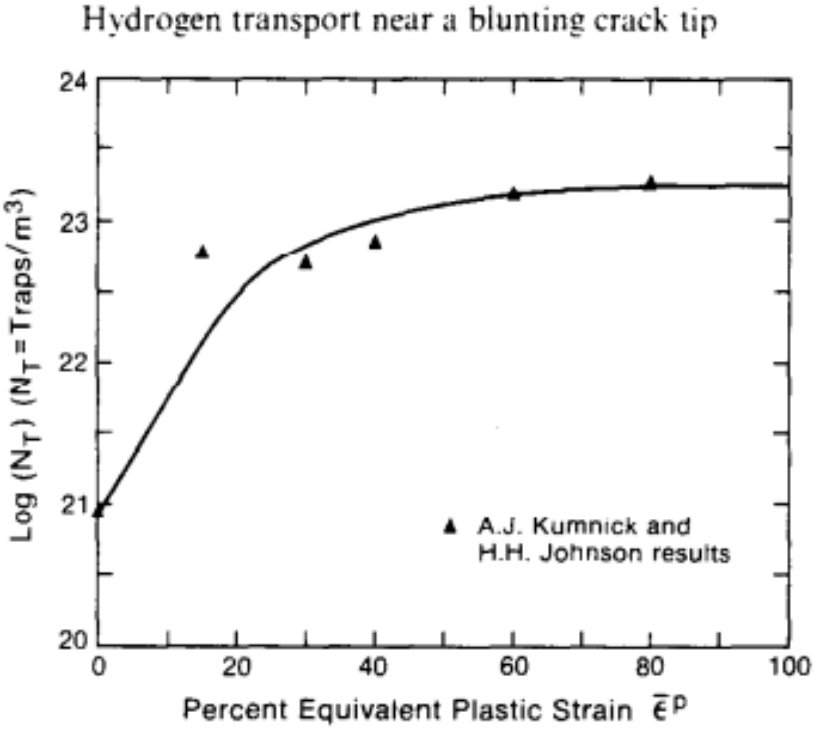

Figure 2.6: Proposed relationship between trap density, N_T equivalent plastic strain, $\bar{\varepsilon}^p$ [23].

The fitting curve in figure 2.6 can be mathematical expressed as:

$$logN_T = 23.26 - 2.33exp(-5.5\bar{\varepsilon}^p) \tag{2.15}$$

Hydrogen transport mainly occur as lattice diffusion by hydrogen jumping between the interstitial sites in the NILS. The hydrogen jumps from sites with high hydrogen concentration to sites with low hydrogen concentration until the hydrogen is evenly distributed in the material[24]. The hydrogen diffusion can be calculated by the metallic flux (Number of particles traversing a unit area per unit time) through Fick‘s First law for three dimensions [26]:

$$\boldsymbol{J} = -D\nabla C \tag{2.16}$$

Where D is the hydrogen diffusion coefficient or diffusivity of the considered species and ∇ is the vector operator. By assuming that the amount of hydrogen is conserved through the diffusion process one can introduce a conservation law[26]:

$$-\nabla * \boldsymbol{J} = \frac{\delta C}{\delta t} \tag{2.17}$$

By combining 2.16 and 2.17 we get Fick‘s second law:

$$\frac{dC}{dt} = \nabla(D\nabla C) \tag{2.18}$$

The hydrogen size is larger then the size of the interstitial sites. Which means that a compression stress is needed for hydrogen to diffuse into the interstitial sites. So a more

complete description of hydrogen diffusion should also account for hydrostatic pressure gradient in Fix second law[26]:

$$\frac{dC_L}{dt} = D\nabla^2 C_L + \frac{D\bar{V}_H}{RT}\nabla C_L * \nabla p + \frac{D\bar{V}_H}{RT} C_L \nabla^2 p \tag{2.19}$$

Where $\bar{V}_H$ is the partial molar volume of hydrogen in the metal and p is the hydrostatic pressure.

By including the influence from hydrogen in traps we get the following Eq. [27]:

$$\frac{dC_L}{dt} + \frac{dC_T}{dt} - \nabla(D\nabla C_L) + \nabla\left(\frac{DC_L\bar{V}_H}{RT}\nabla p\right) = 0 \tag{2.20}$$

2.4 Fracture mechanics

In contrast to the traditional material strength theory, which only consider the applied stress against the yield and ultimate tensile strength, does fracture mechanics include the flaw size in the calculations. Fracture mechanics replaces strength with fracture toughness, the materials ability to withstand fracture when it consists a crack [28]. By including the crack as a parameter a better and safer structural design can be done, as a pre-existing crack may propagate by stresses below the yield strength [28].

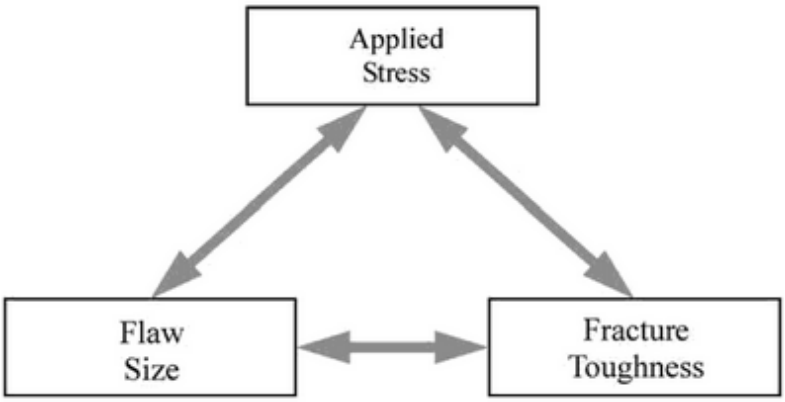

Figure 2.7: Fracture mechanical approach to structural design [11].

A short description of the fracture mechanical parameters used in the current thesis are given bellow.

2.4.1 The Stress Intensity Factor

Linear elastic fracture mechanics (LEFM) is the fracture mechanic theory of materials that behave linear elastic or with only a small degree of plasticity at the crack tip [11]. The stress state at the crack tip can then be defined by a factor called the stress intensity factor, K. By defining a polar axis with origin at the crack tip, the stress field for any linear elastic cracked body may be described by [11]:

$$\sigma_{ij}(r,\theta) = \frac{K}{\sqrt{2\pi r}} f_{ij}(\theta) + \sum_{m=0}^{\infty} A_m r^{\frac{m}{2}} g_{ij}^{(m)}(\theta) \tag{2.21}$$

Where σ_{ij} is the Stress tensor, r and θ is the polar coordinates with origin at the crack tip, K is the stress intensity factor, f_{ij} is a dimensionless constant in the leading term. A_m and $g_{ij}^{(m)}$ is a higher order term, where A_m is the amplitude and $g_{ij}^{(m)}$ is a dimensionless function of θ.

As the stress in Eq. 2.21 is asymptotic to $r = 0$, can it be argued that Eq. 2.21 describes the stress singularity at the crack tip [11]. The loading at the crack tip can be in three different directions. Described as three different modes as shown in figure 2.8. Mode I is a principal load normal to the crack plane, mode II is a in-plane shear loading and Mode

III is out of plane shear. The stress intensity factor is given a subscript which tells the loading mode, so K_I means loading mode I.

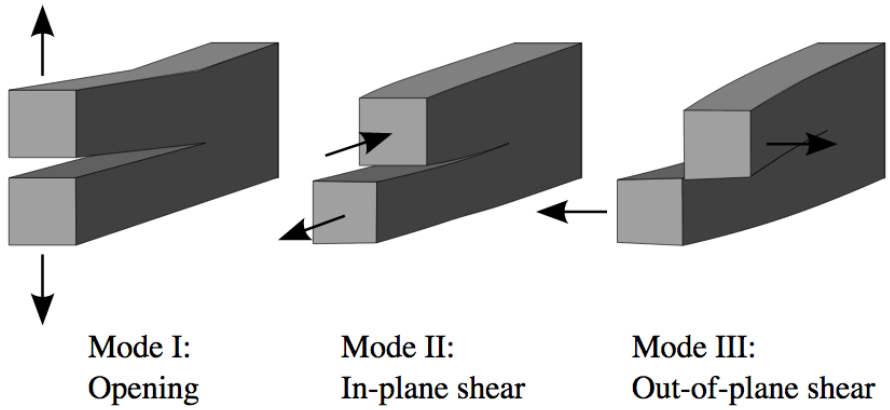

Figure 2.8: Fracture mechanical loading modes [29].

If we only consider loading mode I, with $\theta = 0$ (Only mode I is going to be used in this thesis) and ignore the higher order term, we end up with the following Eq.:

$$\sigma_{yy} = \frac{K_I}{\sqrt{2\pi r}} \tag{2.22}$$

The stress increases in proportion to the stress intensity factor K_I. By knowing the stress intensity factor, the stress may be calculated by the distance from the crack tip, r. Based on this it can be stated that the stress intensity factor defines the crack tip condition, as the amplitude of the crack tip singularity [11].

By consider a global remote loading condition in a body with an internal through crack, K may be written as:

$$K_I = \sigma\sqrt{2\pi a} \tag{2.23}$$

Where a is the crack length in millimeters. For a thoroughly derive of Eq. 2.23 from Eq. 2.22 see Anderson [11] page 92 to 97.

A more general Eq. of the stress intensity factor in loading mode I, can be written as:

$$K_I = \frac{P}{B(W)^{0.5}} * g(a/W) \tag{2.24}$$

Where P is the applied force, W is the width shown in figure 2.9 for a compact tensile (C(T)) specimen, and $g(a/W)$ is a dimensionless function dependent on the specimens geometry and the dimensions relation.

$g(a/W)$ for a C(T) specimen 2.25:

$$g(a/W) = \frac{(2+\frac{a}{W})(0.886+4.64\frac{a}{W}-13.32\frac{a^2}{W^2}+14.72\frac{a^3}{W^3}-5.6\frac{a^4}{W^4})}{1-(\frac{a}{W})^{1.5}} \tag{2.25}$$

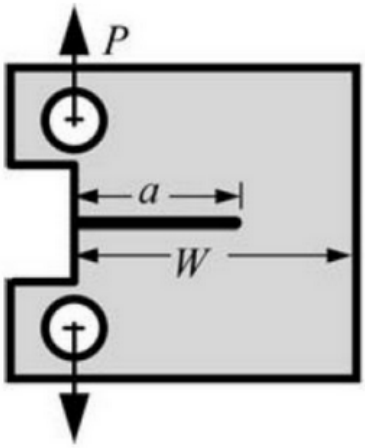

Figure 2.9: Compact tensile (C(T)) specimen [11].

2.4.2 The CTOD

Linear Elastic fracture mechanics is as mentioned earlier only valid as long as there is only a small degree of plasticity surrounding the crack tip. In many materials the plastic deformation is too high to be described by LEFM. Another fracture mechanical model is needed and elastic-plastic Fracture Mechanics (EPFM) comes then into play. This model applies to materials that experiences a plastic deformation at the crack tip before failure, which is known as crack blunting [11]. Wells [30] discovered that the crack blunting increases in relation to the fracture toughness, he then proposed to use the opening at the crack tip as a fracture mechanical parameter. This parameter is today known as the crack tip opening displacement (CTOD). The CTOD can in the limit of small scale yielding be defined as the displacement at the end of the strip-yield zone. It can then be proven that the CTOD can be expressed as [11]:

$$\delta_{el} = \frac{K_I^2}{m\sigma_{ys}E`} \tag{2.26}$$

Where m is a dimensionless constant and E‘is the Young‘s modulus dependent on the stress state. Due to an unique relationship between the J-integral and the CTOD, it can be proven that the CTOD also applies to elastic-plastic materials [11]. There are many different definitions of the CTOD, in the current thesis are the CTOD defined as the displacement of the original crack tip, as shown in figure 2.10.

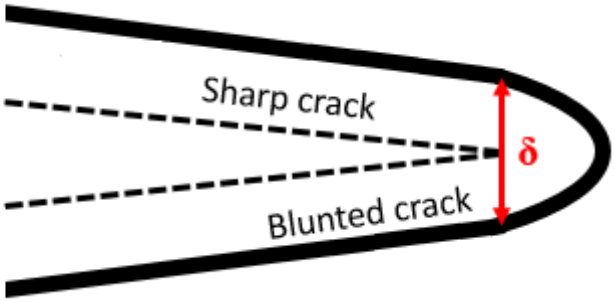

Figure 2.10: The CTOD (δ) is defined in the current thesis as the displacement at the original crack tip.

In regards to laboratory measurements of the CTOD, is the CTOD difficult to measure accurately. The CTOD is instead calculated from the measurement of the displacement of the crack mouth (CMOD) and by assuming that the specimen halves are rigid and rotate about a hinge point. The CTOD is equal to the sum of the elastic, δ_{el} and the plastic δ_p displacement at the original crack tip. A loading mode I specimen gives the following Eq. for the CTOD:

$$CTOD = \delta_{el} + \delta_p = \frac{K_I^2}{m\sigma_{ys}E'} + \frac{r_p(W-a)V_p}{r_p(w-a)+a+z} \tag{2.27}$$

Where r_p is the plastic rotational factor, V_P is the plastic CMOD and z is the knife edge height, see figure 2.11 for the estimation of CTOD for a three point bending specimen.

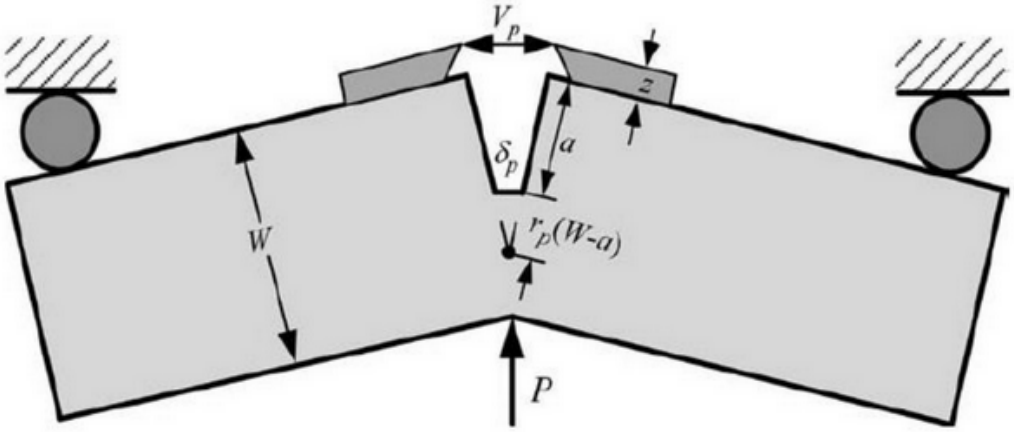

Figure 2.11: Estimation of the CTOD for a three point bending specimen [11].

Similarly the CTOD can be calculated when accounting for stable crack growth [31]:

$$\delta_{corr} = \frac{K_I^2}{\sigma_{ys}} + \frac{0.54\Delta a + r_p(W-a)}{0.54(a+\Delta a) + r_p W + (W_t - W) + z} * V_p \tag{2.28}$$

2.4.3 The R-curve

Most types of steels do not usually fail catastrophically when the crack starts to grow, a stable crack growth can rather be observed. The stable crack growth can be described by a rising fracture resistance curve, also called the R-curve. Figure 2.12 Illustrates the fracture resistance curve for a ductile material [11]. The fracture resistance curve can be used to find the fracture toughness value δ_{IC} and the associated J_{IC}. Which is defined as the CTOD and J value where the initiation of stable crack growth occur [11]. The crack growth are usually stable at initiation, illustrated by a steep R-curve, but as the crack grows the crack growth may become unstable. instability occur in the moment when the driving force rate are higher then the rate of the R-curve.

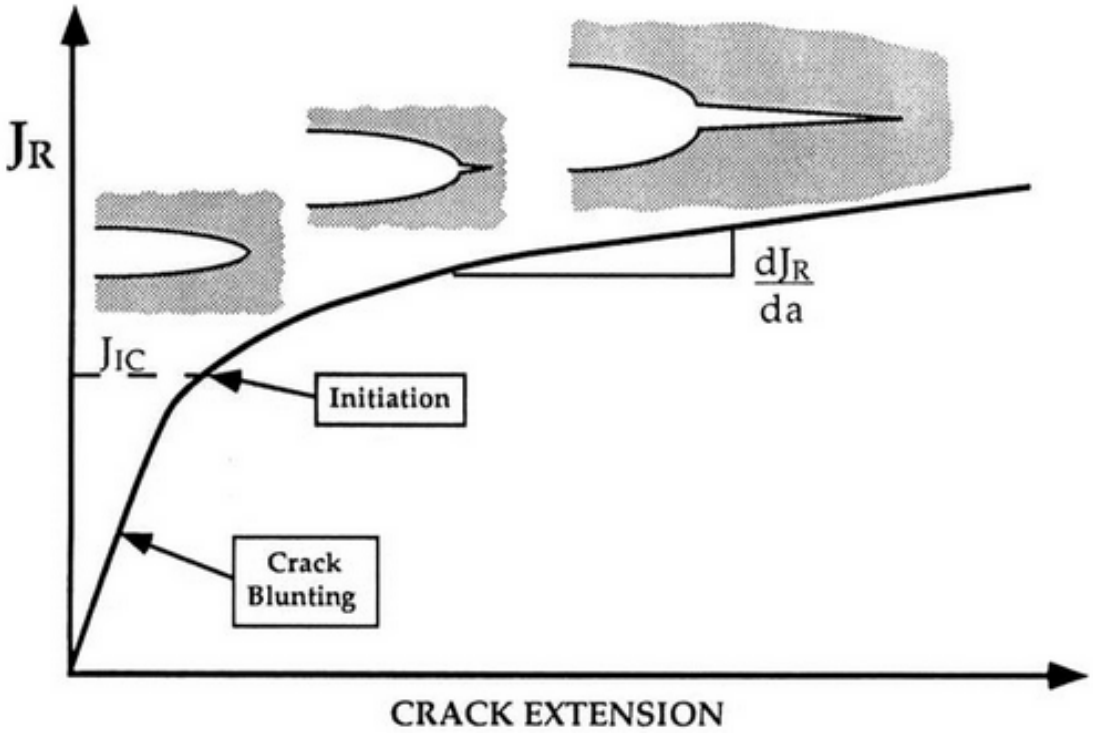

Figure 2.12: Ilustration of the R-curve for a ductile material [11].

2.5 Cohesive Zone Modelling

2.5.1 Background

When a material contains a sharp crack the stress at the crack tip becomes infinite. This means that the material should fail at an infinite small load, as no material can withstand a infinite high stress. This is unrealistic and incorrect in any practical perspective.

Cohesive zone modelling (CZM) is based on the thought that infinite stresses at the crack tip is unrealistic and that fracture is a gradual possess separating the surface adjacent to the crack tip [32][33]. CZM has it‘s origin from the strip yield model developed by Dugdale [34] and Barenblatt [35], shown in figure 2.13. They divide an embedded crack in a infinite wide sheet, into two parts; A stress free part and a loaded part containing a cohesive stress [32].

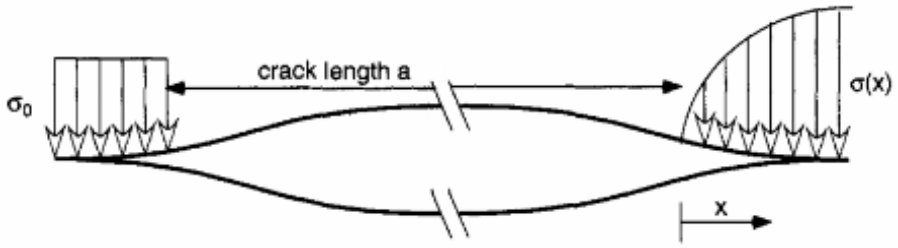

Figure 2.13: Strip yield model, Dugdale‘s model on the left and Barenblatt‘s model on the right [32].

The strip yield model assumes a thin plastic zone at the crack tip [11].This zone is defined by a compression stress, hereinafter called the cohesive strength [11]. The cohesive strength remains finite and keeps the crack from expanding. Dugdale chose to set the cohesive strength equal to the yield strength, while Barenblatt replaced it with a cohesive law[32]. The material will separate when the cohesive strength is exceeded, which means that the stress remains finite at the crack tip. This gives many benefits as we get rid of the infinite stress at the crack tip, which classical fracture mechanics assumes. In application to fracture behavior in FE-analysis, the CZM was first used for concrete by Hillerborg [36]. Later it was expanded for metals by Needleman [37] and Tvergaard and Hutchinson [38]. The key difference between Barenblatt‘s strip yield model and the CZM we use today, is that the cohesive stress is not defined as a function of the distance from the crack tip, but as a function of separation of the crack surfaces. The function of separation of the crack surface is described in the next section.

2.5.2 The Traction Separation Law

One main advantage with cohesive zone modelling is that it can easily be implemented into FE-codes, through interface elements that are already embedded into the code. The constitutive behavior of the interface elements can be controlled by a Traction Separation law (TSL). TSL relates the cohesive stress to the displacement of the element [39]. The continuum elements remains damage free, while the cohesive elements takes up the cohesive stress until a critical displacement is reached. A new free crack surface is then created. The TSL is usual used for material simulations, where the TSL is defined by three parameters, two of them are independent; The critical cohesive stress, σ_c, critical cohesive separation δ_c and the total energy dissipation at fracture Γ_c [40].
Γ_c can be derived by [41]:

$$\Gamma_c = \int_0^{\delta_c} \sigma(\delta) d\delta \tag{2.29}$$

Where $\sigma(\delta)$ is the cohesive strength as a function of the cohesive element separation δ. Several definitions of the TSL have been developed by different authors but some common features can be found [41]:

1. They all consists of the two material parameters, critical cohesive stress, σ_c and critical cohesive separation δ_c
2. Failure, Completely separation of the cohesive element occur when $\delta > \delta_c$ ($\sigma(\delta)$ becomes equal to zero).

Another thing to note is that the TSL is purely phenomenological and is not representative for any physical material[41].

Needleman [37] proposed a polynomial TSL to describe particle matrix dechoesion. When subjected to a pure normal separation the TSL becomes:

$$\sigma(\delta) = \frac{27}{4}\sigma_c \frac{\delta}{\delta_c}\left(1 - \frac{\delta}{\delta_c}\right)^2 \text{ for } \delta < \delta_c, \text{ otherwise } 0 \tag{2.30}$$

Where the critical surface energy becomes:

$$\Gamma_c = \frac{9}{16}\sigma_c \delta_c \tag{2.31}$$

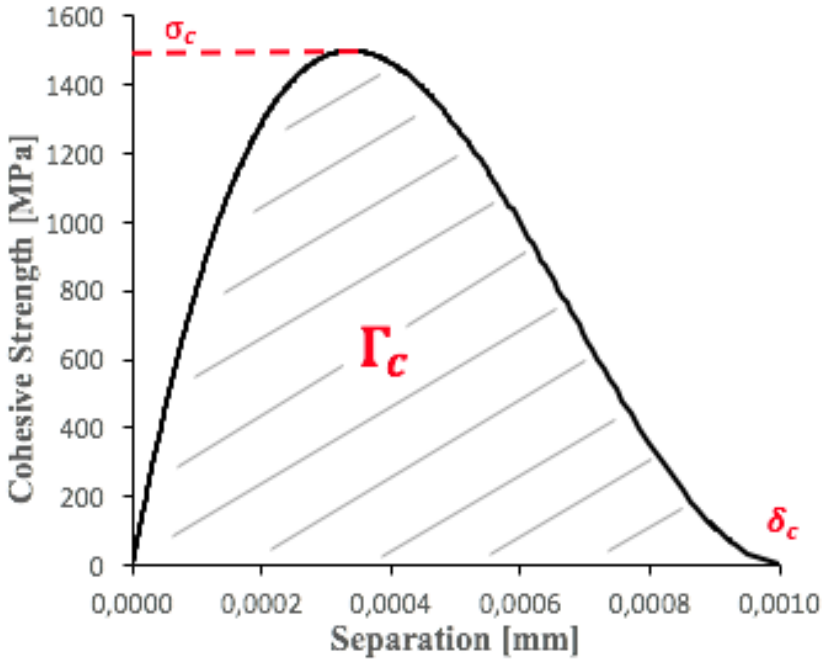

Figure 2.14: Needleman‘s TSL

By defining the cohesive element stiffness, k as the slope of the TSL curve it becomes:

$$k = \frac{d\sigma}{d\delta} * t \tag{2.32}$$

Where t is the thickness of the cohesive element.

By derivation of equation 2.30 and inserting the cohesive stiffness, equation 2.32 we get:

$$k = \sigma`(\delta) = \frac{27}{4}\frac{\sigma_c}{\delta_c}\left(1 - 4\frac{\sigma}{\delta_c} + 3(\frac{\delta}{\delta_c})^2\right) \tag{2.33}$$

The initial stiffness can then be found by setting $\sigma_c = 0$ in equation: 2.33:

$$k_i = \sigma`(0) = \frac{27}{4}\frac{\sigma_c}{\delta_c} * t \tag{2.34}$$

Geubelle [42] proposed a Bilinear TSL to describe delamination of composites subjected to low viscosity impact. The Bilinear TSL is described by:

$$\sigma(\delta) = \begin{cases} k_i\delta & \text{if } \delta \leq \delta_1 \\ \sigma_c(1 - \frac{\delta - \delta_1}{\delta_0 \delta_1}) & \text{if } \delta_1 < \delta < \delta_0 \\ 0 & \text{otherwise} \end{cases} \tag{2.35}$$

Where $\delta_0 = \delta_c$.

The initial stiffness is defined as the slope of the increasing load part of the curve:

$$k_i = \frac{\sigma_c}{\delta_1} * t \tag{2.36}$$

By integrate Eq. 2.35 the critical surface energy Γ_c becomes:

$$\Gamma_c = \frac{1}{2}[\sigma_c \delta_1 + \sigma_c(\delta_0 - \delta_1)] \tag{2.37}$$

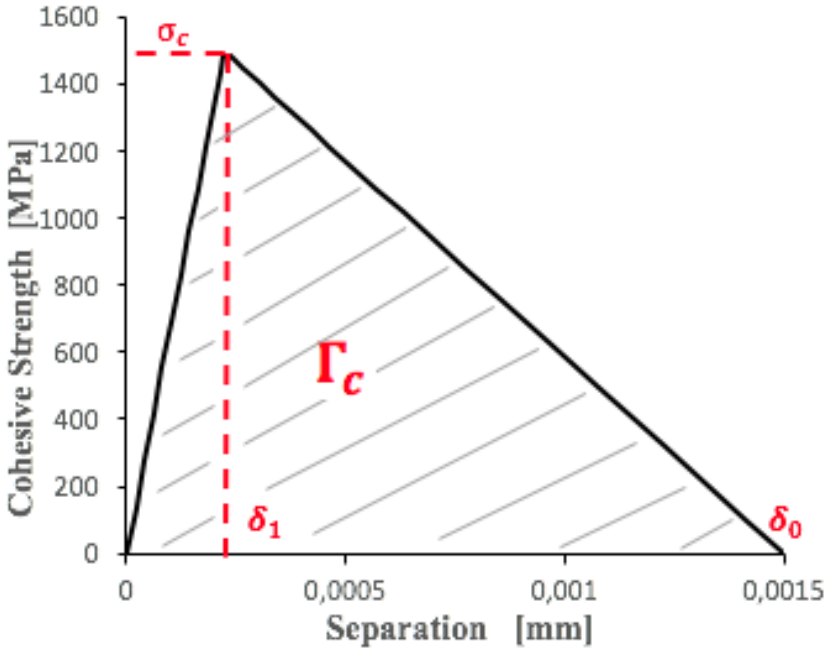

Figure 2.15: Bilinear TSL

2.5.3 Viscous Regularization Scheme

Despite that cohesive elements are quite easy to implement into the FE-model, the computations might encounter numerical difficulties, after the TSL curve has passed the critical cohesive stress. It may not be able to converge an equilibrium solution. This issue can often be explained by the ”snap-back” problem [43]. Where the controlled displacement or loading are violating its predetermined path. The problem occur when the energy needed in separating the cohesive elements, following the TSL, is less then the energy released when creating new surfaces [44].

Gao and Bower [45] has proposed a solution for the convergence problem by including a small viscus term in Needlemans‘s TSL:

$$\sigma(\delta) = \frac{27}{4}\sigma_c \frac{\delta}{\delta_0}\left(1 - \frac{\delta}{\delta_c}\right)^2 + \zeta \frac{d}{dt}\left(\frac{\delta}{\delta_c}\right) \tag{2.38}$$

The viscous regulation scheme keeps the simulation stable by adding a viscosity parameter, ζ dependent on time and separation rate. This keeps the computation stable by absorbing the extra energy that is released when the cohesive elements separates [44]. In a more practical view the viscous regulation scheme can be looked upon as a dashpot. It

is then important to note that the viscosity is not intended for any physical energy dissipation but only as a theoretical coefficient. Another thing one needs to keep in mind is that a high viscosity parameter will delay the failure initiation and absorb more energy, which leads to a higher maximum cohesive stress, then the pre-defined critical cohesive stress [44], so it is important to keep the viscosity parameter as small as possible to get a more accurate result.

2.5.4 Hydrogen influence on the TSL

The hydrogen influence on the TSL curve might be accounted for by decreasing the critical cohesive stress as the total hydrogen coverage θ_H are increasing, following a relationship originally developed by Serebrinsky [46], based on calculations by Jiang and Carter [47].

$$\frac{\sigma_c(\theta_H)}{\sigma_c(0)} = 1 - 1.0467\theta_H + 0.1687\theta_H^2 \tag{2.39}$$

Where $\sigma_c(\theta_H)$ is the critical hydrogen dependent cohesive stress and $\sigma_c(0)$ is the critical cohesive stress without hydrogen influence. The hydrogen coverage is defined by the Langmuir-McLean isotherm [48], relating it to the bulk hydrogen concentration C.

$$\theta_H = \frac{C}{C + exp(-\Delta G_b^0/RT)} \tag{2.40}$$

Where ΔG_b^0 is the Gibbs energy difference between surface and bulk material.

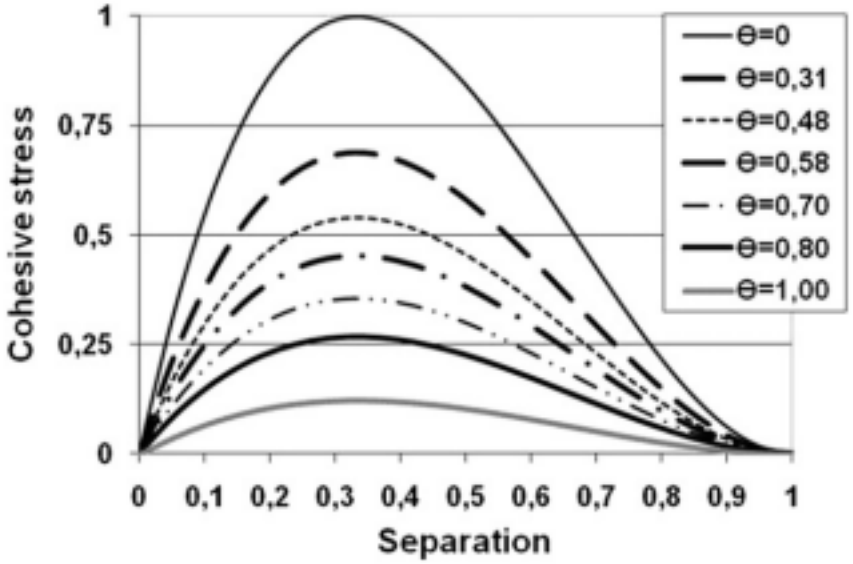

Figure 2.16: Hydrogen influence on the TSL [49].

3. Method and Materials

3.1 Experimental testing

Compact tension (C(T)) fracture mechanical tests were done in air and under cathodic protection (CP). The samples where tested without a sharp pre-crack, but only with a machined round notch, as it was deemed impossible to propagate a sharp fatigue pre-crack exactly along the dissimilar interface. This violates the demand for a sharp pre-crack to obtain the materials true fracture toughness, but the results can still be used to compare the effect of different material combination and hydrogen and weld influence.

3.1.1 Description of the test Specimens

Two different types of samples were tested; one type with a nickel-interlayer (hereinafter called sample A) and one without (hereinafter called sample B):

Sample	**A**	**B**
Ni-interlayer	Yes	No

Table 3.1: Two different types of samples were tested.

The samples were machined by electro-discharge machining after the given dimensions and geometry as shown in figure 3.1. The holes were drilled by a Ø1.25mm drill bit. The holes were later re-machined to Ø1.4mm as the test rig pins did not fit. The holes were increased instead of remaking smaller pins as previous tests had revealed plastic deformation of the pins during testing. The small size of the C(T) samples are caused by the size of the clad, as the clad was only 3mm thick.

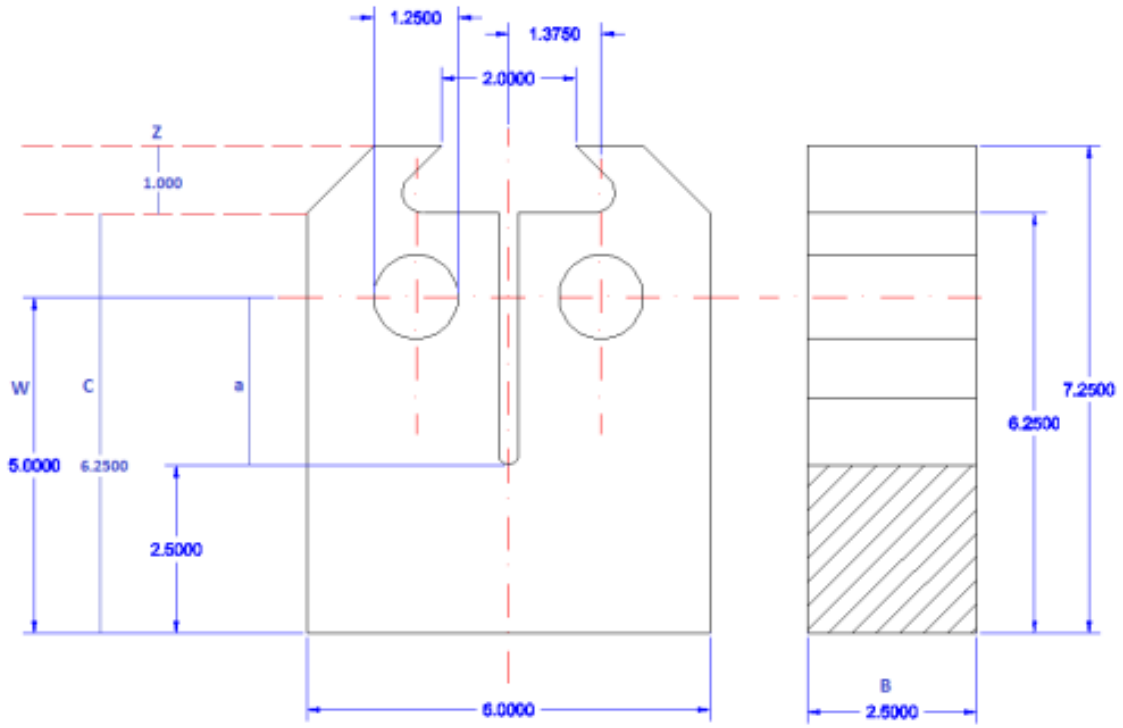

Figure 3.1: Machine drawing of C(T) specimen [4].

The machined notch was placed as shown in figure 3.2 at the point were the base material, clad and weld metal (and nickel interlayer for sample A) met, hereinafter called the triple point.

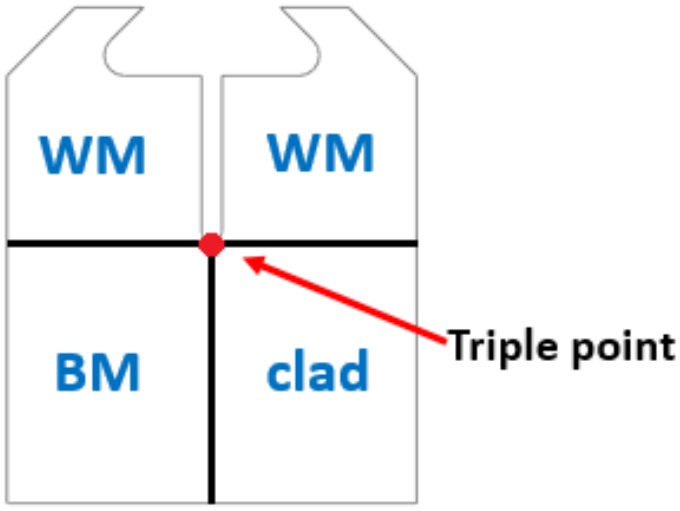

Figure 3.2: Material sections in the test sample. The tip of the notch was placed where the three different materials meets.

A description on where the A and B samples were extracted from are given bellow:

The A samples came from the same batch of samples as Degos [5] used in his internship. The A samples were extracted from a Girth welded clad pipe as shown in figure 3.3.

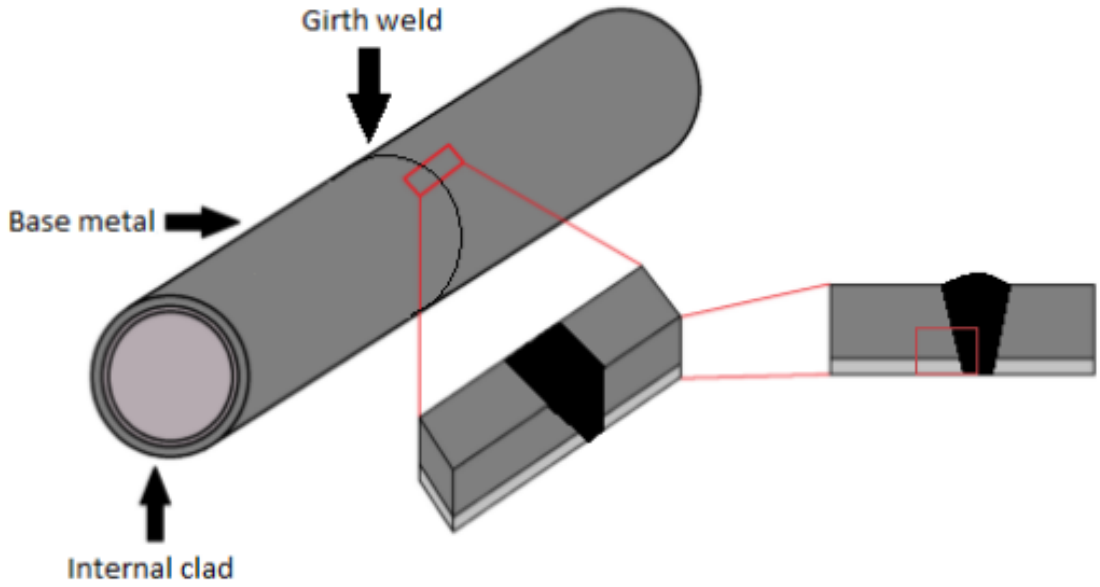

Figure 3.3: The A samples were extracted from a girth welded clad pipe [5].

As Degos [5] and Bjaaland [2] discovered cracks in their girth welded clad pipe samples, another method was chosen for the B samples in the current thesis. The B-samples were extracted from two clad plates that where stacked on top of each other with the clad layers facing each other, as shown in figure 3.4. One side of the plates was welded by a cold metal transfer weld (CMT) at the clad and a combination of pulse welding and CMT on the BM. The welding was done without a welding seam as the goal was only to extract samples from the heat affected zone and not to create a strong weld between the two clad plates.

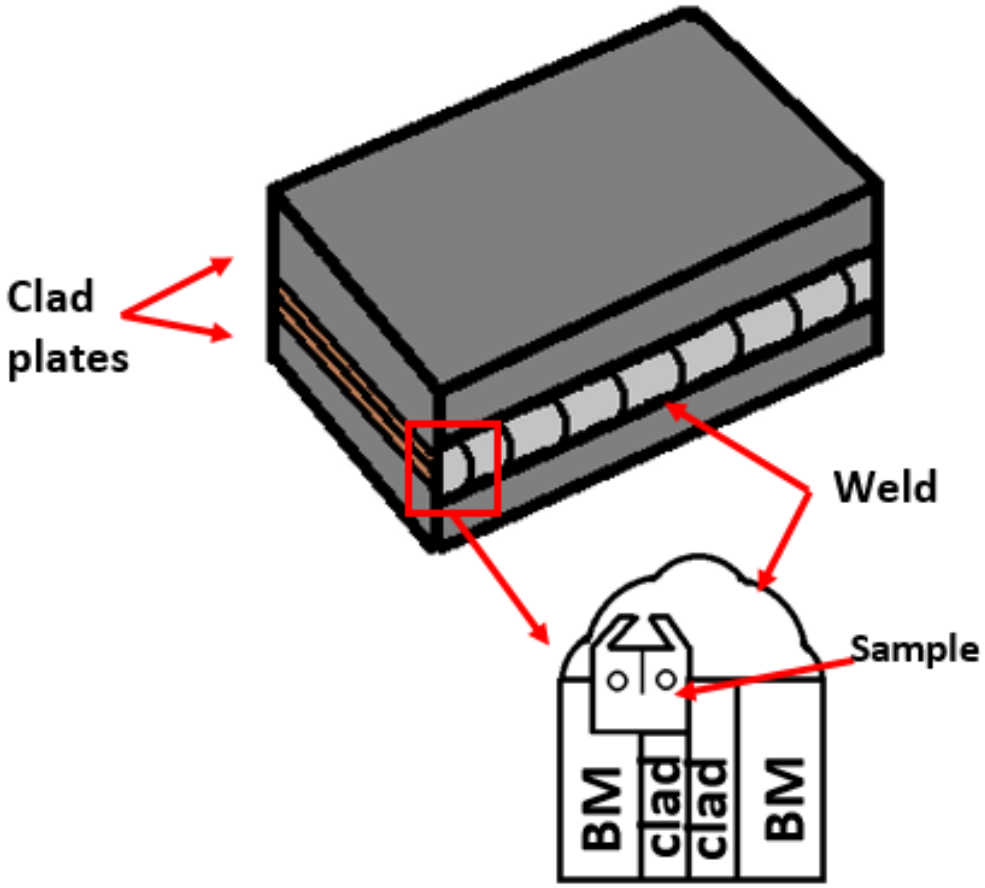

Figure 3.4: The B samples were extracted from two clad plates that had been welded together.

3.1.2 Sample treatment prior to testing

All the samples were measured prior to testing as explained in appendix A.2. All the B samples were checked in a light optical microscope for cracks and weld defects on the surface, as a new type of welded samples required extra caution. The placement of the notch related to the triple point in the B samples were also checked in LOM. The triple point are described in 3.2.

3.1.3 Testing procedure

C(T) fracture mechanical tests were done in a Cormet slow strain rate test rig, in accordance with BS7448-4 [31]. The testing was conducted in air and under CP. Load, displacement and CMOD where logged for every 1 second. The CMOD was measured by a clip gauge in air as shown in figure 3.5. This was not done under CP as it was not possible with the current equipment. Instead the CMOD was calculated from the displacement by Eq. 3.3 in section 3.1.5. The tests were load controlled with a loading rate of $0.7N/min$, corresponding to a stress intensity rate of $\frac{dK}{dt} = 6.4 * 10^{-}8$, calculated from Bjaaland's [4] results. 0.7 was used instead of 0.74 due to a one decimal limit on the used test machine. The loading rate was chosen to give hydrogen sufficient time to diffuse into the fracture process zone under CP. Based on the stress intensity rate found by previous work of Lee and Gangloff [50], who measured Hydrogen environment-assisted cracking (HEAC) on high-strength steel.

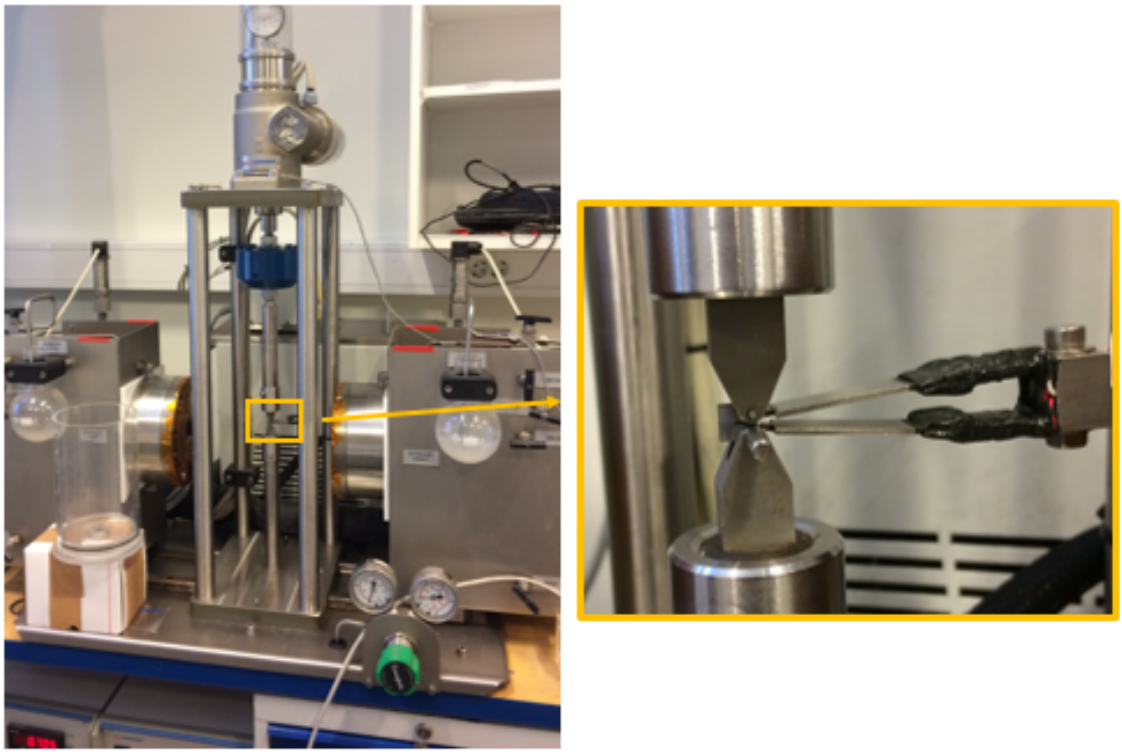

Figure 3.5: Cormet slow strain rate test rig, test setup in air.

Samples tested under CP were immersed in a 3.5% NaCl solution at room temperature, with an applied potential of $-1050mV_{SCE}$ to imitate the CP condition in seawater [51]. Measured by a saturated calomel electrode (SCE), connected to the test container through a salt bridge. The test setup is shown in figure 3.6. The machine was isolated from the test specimen by a polymer composite transition. The potentiostat was connected to the specimen by a isolated platinum wire and a platinum counter electrode. The sample was pre-charged for 24 hours before testing, to let a sufficient hydrogen concentration appear at the sample surface. 24 hours was decided sufficient based on Oldens findings on the diffusion coefficient for X70 steel [52].

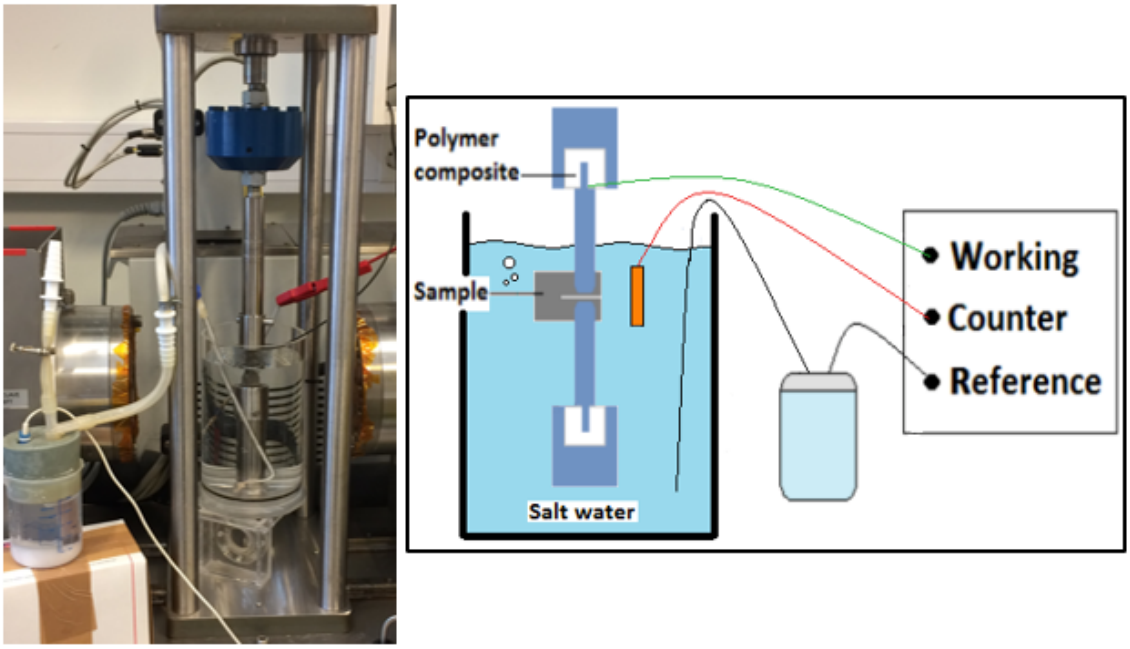

Figure 3.6: Cormet slow strain rate test rig, test setup under CP.

3.1.4 Sample treatment post testing

After testing, the fracture surface was looked upon for defects in LOM.

The A samples were heat tintet and then broken in liquid nitrogen to measure the stable crack growth, that had occurred during testing. Heat tinting causes oxidation on the fracture surface, which means that the fracture surface turns black, so it becomes measurable under LOM.

Sample A9, A10 and A11 were heat tintet under a propane gas flame until the samples were glowing red. This showed an insufficient result as no oxidation could be seen on the fracture surface, see appendix A.4. The rest of the A samples were heat tintet in an oven from room temperature and up to $600^{\circ}C$. This gave a successfully heat tinting as shown in appendix A.2.

One sample tested in air and one sample tested under CP of the B-samples was embedded into a 40mm mold. This was done to investigate the fracture path along the specimens ligament, with a light optical microscope (LOM). The samples were cold embedded by using Struers EpoFix®resin and EpoFix®hardener, with mixing ratio 25 and 3 respectively. Curing time was 8 hours. The samples were later manually grinded with SiC grinding paper 220, 320, 1000 and 2400, followed by polishing by a Dac cloth. The samples were washed by soap and water, rinsed in ethyl alcohol and dried by a blow drier between each grinding and polishing step. The samples were finally etched in 2 % nital for 20 seconds before investigation to reveal the BM.

3.1.5 Analysis of test data

A short description on the calculations done to find the fracture toughness of the test samples are given below. For a more thoroughly read are section A.3 in the appendix recommended.

The initial crack length and the crack growth was measured in accordance to BS7448-1 [53] and BS7448-4 [31] respectively. Due to the small size of the specimens were only five lengths measured instead of the recommended nine. For experimental work the theoretical initial crack length, a was replaced by a measured initial crack length a_0. a_0 is equal to the average of five initial crack lengths, measured after testing:

$$a_0 = \frac{1}{4}\left(\frac{a_1 + a_5}{2} + \sum_{i=2}^{i=4} a_i\right) \tag{3.1}$$

The crack growth Δa was found in a similar manner:

$$\Delta a = \frac{1}{4}\left(\frac{\Delta a_1 + \Delta a_5}{2} + \sum_{i=2}^{i=4} \Delta a_i\right) \tag{3.2}$$

See appendix section A.2 for a more detailed description on how a_i and Δa_i were measured.

The plastic CMOD for the tests under CP, $V_{p,CP}$ was found by the ratio between plastic CMOD $V_{p,air}$ and plastic displacement $d_{p,air}$ in air [1]:

$$V_{p,CP} = \left(\frac{V_{p,air}}{d_{p,air}}\right) d_{p,CP} \tag{3.3}$$

The CMOD of the samples tested under CP are found in a similar manner by curve fitting with the samples tested in air, see appendix A.3 for a detailed description.

The CTOD max was calculated by Eq. 2.27 at max force in accordance to BS 7448-1 [53]. The CTOD accounting for stable crack growth was calculated by Eq. 2.28 in accordance to BS 7488-4 [31].

3.2 Finite Element Analysis

3.2.1 Model framework

Modelling and FE-Simulation of plastic deformation and material damage was simulated by using the finite element code ABAQUS, Standard version 6.14. The FE-simulation was divided into seven steps:

1. Mesh refinement analysis to determine the mesh size.
2. Static analysis with implemented cohesive elements to verify the cohesive elements stiffness.
3. Simulate crack propagation with a linear elastic material through a temperature-displacement analysis.
4. Simulate crack propagation with an elastic- plastic material through a temperature-displacement analysis.
5. Simulate the crack propagation occurring in the dissimilar material interface samples experimentally tested in air by Jemblie [1], without Ni-interlayer.
6. Verify the dissimilar material interface simulation with experimental results from Jemblie [1].
7. Check the material effect on the R-curve.

The simulations were only done without hydrogen influence on the TSL, Due to numerical difficulties occurring when sufficiently high cohesive parameters were used, compared to experimental results.

3.2.2 FE-model description

A 2D FE-model was modelled to imitate the C(T) fracture mechanical tests done at the lab. The FE-model was dimensioned by following the machine drawing for the experimental specimens given in figure 3.1, with the exception of the sharp crack. The relation between crack and notch was based on the drawing shown in figure B.1 in appendix B.1.1.

The FE-model was fully constrained in the node corresponding to the bottom pin hole and horizontally constrained in the node corresponding to the top pin hole, as shown in figure 3.7. The FE-model was load controlled with a vertical load in the node corresponding to the top pin hole. The load was set equal to 403.2 N/mm for the static analysis and $436.8 N/mm$ for the coupled temperature displacement analysis. $436.8 N/mm$ corresponds to $0.7 N/min$ for 26 hours for the coupled temperature-displacement analysis.

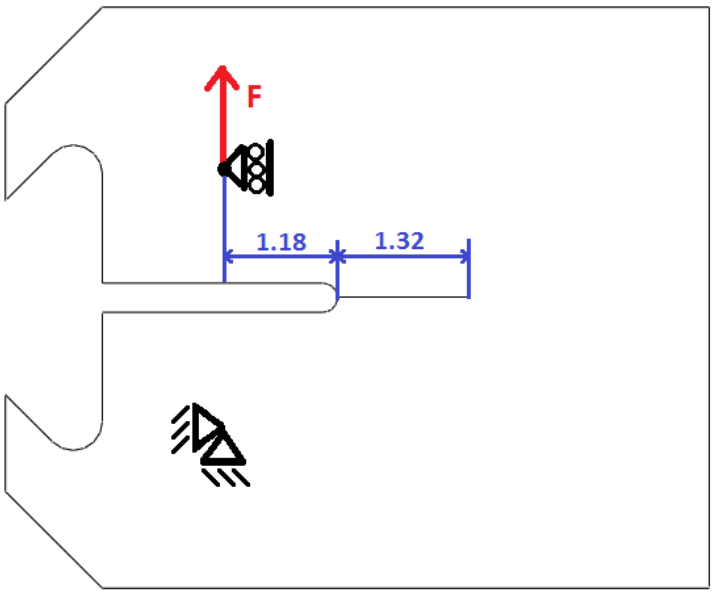

Figure 3.7: Loading, constraints and dimensions of notch and crack in the FE-model.

The FE-model was divided into 10 material sections as shown in figure 3.8, to make it possible to run the simulation with different materials added in the model simultaneously. The dimensions of the sections are given in figure B.2 in appendix B.1.2. Elastic materials was placed around the constrained and loaded nodes to avoid concentrated plastic deformation, which would increase the simulation time. For the simulations with clad steels the carbon depleted BM was introduced in sections BM, Ni_1, Ni_2, Ni_3, Ni_4, Ni_5, and the clad was introduced in section Ni_6 and clad. This was based on Bjaaland's [4] findings, which showed that the crack propagated slightly into the carbon depleted BM, for the specimens without Ni-interlayer tested in air.

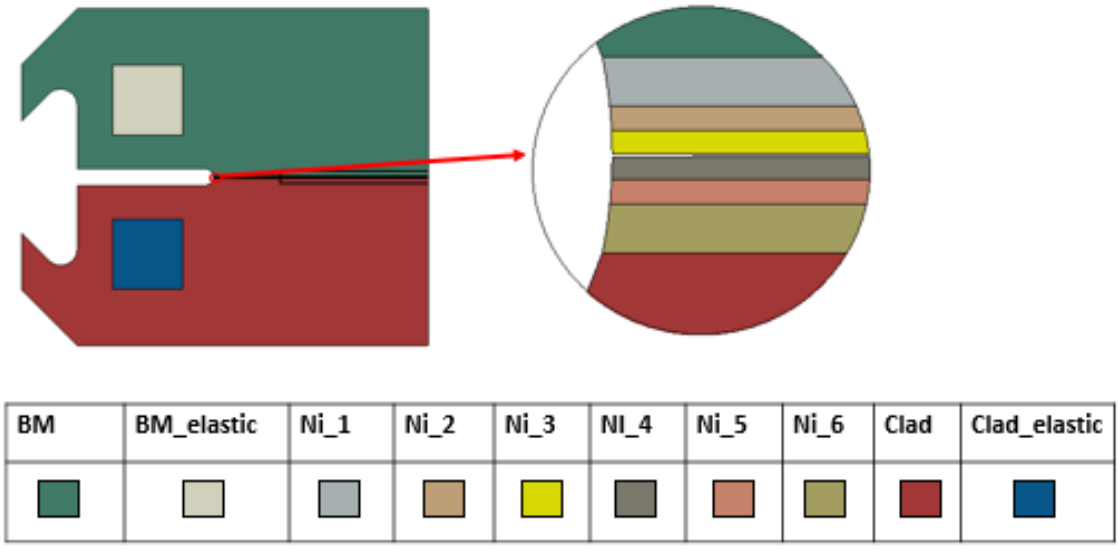

Figure 3.8: Material sections in the FE-model.

4-node bilinear plane strain continuum elements were used in the static analysis. Temperature-

displacement plane strain continuum elements, CPE4RT was used in the coupled Temperature-displacement analysis. The mesh size was $0.12mm$ and refined in two steps too $7.5\mu m$ close to the initial crack tip and along the crack ligament, the size of the refined area are shown in figure B.3 and B.4, given in appendix B.1.3. The mesh refinement was generated by using a Phyton script, plug-in tool in ABAQUS.

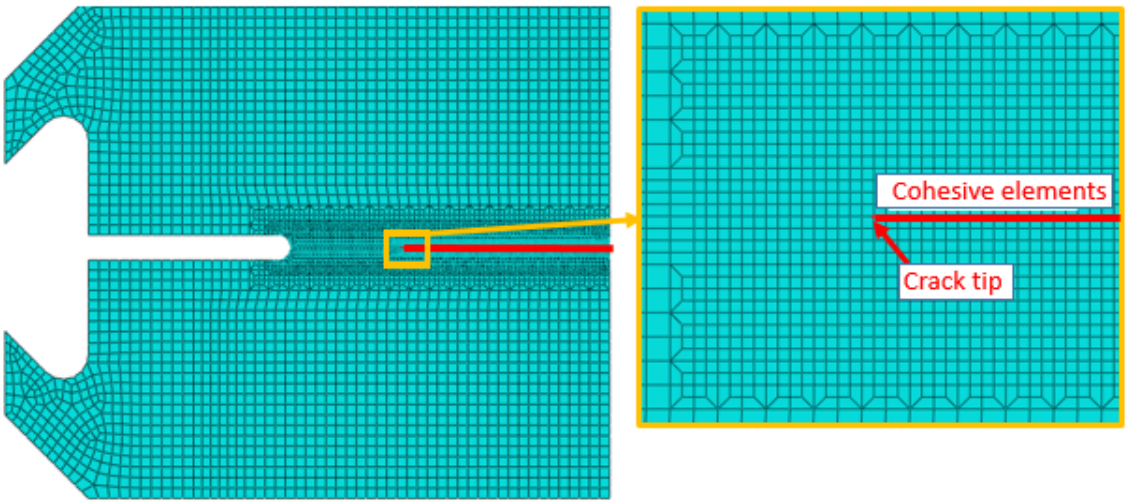

Figure 3.9: Mesh and cohesive elements.

3.2.3 Mesh refinement analysis

To get accurate results the element size needs to be correct. If the mesh size is too large it will not be able to accurately capture the stress/strain field at the crack tip, and a small element size is computer costly. A too small element size might also be affected by the displacement at the crack tip and become unstable, which again will give an inaccurate stress/strain field. A static analysis was done with Base material (BM) to find the most suiting element size for the simulations. Four analyses were done with the refined element size equal to $30\mu m$, $15\mu m$, $7.5\mu m$ and $3.75\mu m$. The opening stress and the hydrostatic pressure was plotted for a linear path along the crack ligament. Opening stress and hydrostatic pressure were chosen because of their effect on hydrogen influence simulations. The opening stress affects the strength of the cohesive elements, while the hydrostatic pressure affects the hydrogen lattice concentration C_L, which again affect‘s the TSL curve with hydrogen influence.

3.2.4 Cohesive Zone Modelling

2D four-node user defined cohesive zone elements (hereinafter called cohesive elements) CZL2H2 were implemented in ABAQUS through the user subroutine UEL, as described in [54]. Due to an error in the script the cohesive elements were manually attached to the continuum elements. The results were outputted from two integration points in each element. Only the results from integration point one were used in this thesis. The cohesive elements were placed along the crack ligament as shown in figure 3.9. The cohesive

elements behavior were defined by a traction separation law in the normal direction and by an elastic stiffness in the tangential direction, as shown in figure 3.10 Needleman's TSL with viscous regulation scheme, Eq. 2.38 was mostly used, except for one coupled temperature-displacement simulation with a bilinear TSL with viscous regulation scheme.

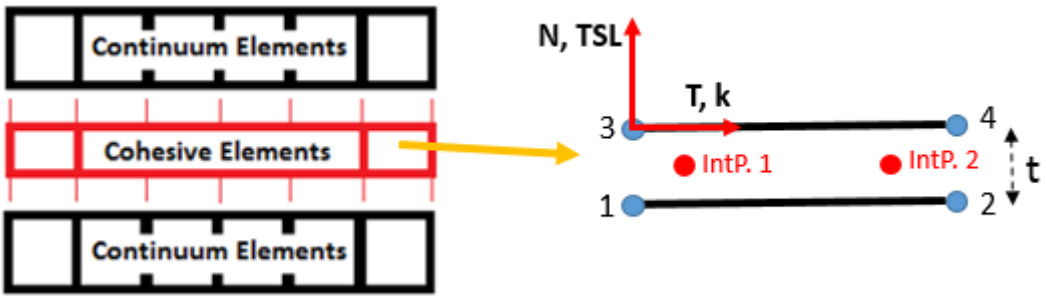

Figure 3.10: Description of the cohesive elements used in the current thesis.

The geometrical thickness t of the cohesive element is is initially zero.

The initial cohesive element stiffness was calculated from Eq. 2.34 for Needleman's TSL and by Eq. 2.36 for the bilinear TSL, setting the geometrical cohesive element stiffness equal to 1. It is important to note that the initial cohesive element stiffness is only used as a parameter to find a sufficient stiffness for the cohesive elements and does not represent any physical value. An effort in improving the crack propagation was done by using a bilinear TSL curve. By using a bilinear TSL curve it is possible to have a initial steep slope to achieve a high enough stiffness, and at the same time get a gentle slope in the unloading part of the curve. This is important as a steep unloading slope is known to cause divergence problems [55].

3.2.5 Stiffness verification of the Cohesive Elements

As stated by Alvaro [56] the initial stiffness of the cohesive zone elements (CZE) may affect the result. If the stiffness is too low it will soften the model and give a lower hydrostatic stress and equivalent plastic strain, consequently affecting the lattice and trapped hydrogen population. To verify the cohesive stiffness the opening stress and the equivalent plastic strain at the crack tip needs to be checked and compared with a model without cohesive elements. The initial cohesive element stiffness was increased until a god fit with the simulation without cohesive elements occurred. Two simulations with different initial cohesive element stiffness were done. Initial cohesive element stiffness equal to 10^6 and 10^7. 10^6 was first used based on Alvaro's [56] and Jemblie's [6] findings. The initial stiffness was then increased to 10^7 when 10^7 showed an insufficient result. The initial cohesive stiffness was calculated by Eq. 2.34 in section 2.5.2. setting the cohesive element stiffness equal to one. Table 3.2 shows the initial cohesive element stiffness with the associated cohesive element parameters. The cohesive parameters are chosen at random to achieve the specific initial cohesive element stiffness.

Init. CZE stiffness [MPa]	σ_c[MPa]	δ_c[mm]
10^6	5000	0.0135
10^7	5000	0.00135

Table 3.2: Simulations done to verify the cohesive element stiffness.

3.2.6 Implementation of Hydrogen in the FE model

The hydrogen diffusion as described in section 2.3.4 was implemented through the user subroutine UMATHT, as described in [57]. The subroutine takes advantages of the similarities between the equations for heat and mass diffusion, Fourier's and Fick's law. It implements hydrogen diffusion by replacing temperature with hydrogen concentration. To simulate the tests in air done at the lab, the hydrogen's degree of freedom was removed in the input file. This sets hydrogen concentration, $C_H = 0$ which means that the hydrogen should have no effect on the TSL.

3.2.7 Crack Growth

Cohesive elements makes it possible to simulate crack growth in the FE-model, due to the element separation defined by the TSL. The crack tip was defined as the element closest to the initial crack tip that has not reached the critical cohesive separation δ_c (in integration point 1), as shown in figure 3.11.

The crack growth was calculated by:

$$\Delta a = (E_1 - E_0) * S \tag{3.4}$$

Where E_0 is the element at the crack tip, E_1 is the element closest to the initial crack tip that has not reached δ_c and S is the element size at the crack tip.

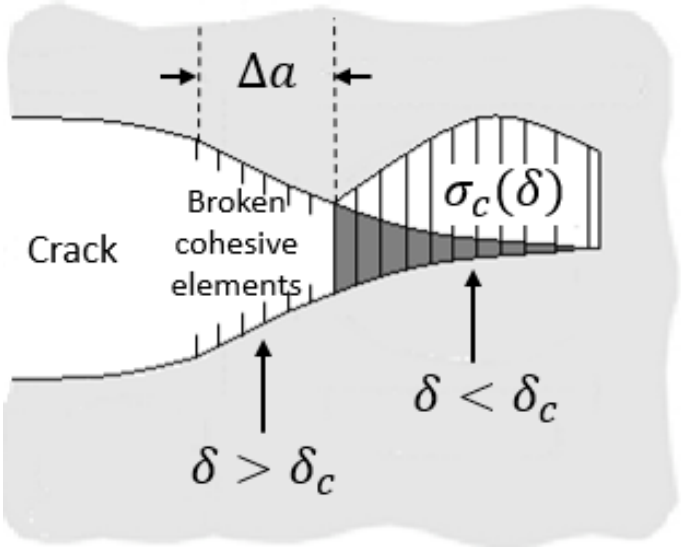

Figure 3.11: Definition of the current crack tip in FE-simulation and the following crack growth length.

The following crack growth simulations were done:

#	Material	TSL	σ_c[MPa]	δ_c[mm]	δ_1[mm]
1	Linear elastic	Needleman	1500	0.001	[-]
2	BM	Needleman	1500	0.001	[-]
3	BM	Needleman	1000	0.000675	[-]
4	clad & C-depl. BM	Needleman	1000	0.0010	[-]
5	clad & C-depl. BM	Needleman	1500	0.0015	[-]
6	clad & C-depl. BM	Needleman	1800	0.0018	[-]
7	clad & C-depl. BM	Needleman	2500	0.0025	[-]
8	clad & C-depl. BM	Bilinear	1500	0.0015	0.00022

Table 3.3: The crack growth simulations done in the current thesis.

Needleman‘s TSL were used for simulation 1-7 and a bilinear TSL was used for simulation 8. The cohesive parameters gives an initial cohesive stiffness of $k_i = 10^7$ for simulation number 1-3 and $k_i = 6.75 * 10^6$ for simulation number 4-7, calculated by Eq. 2.34 in section 2.5.2. $k_i = 6.75 * 10^6$ for simulation number 8 calculated by Eq. 2.36 for bilinear TSL in section 2.5.2. The viscosity parameter ζ was set equal to $5 * 10^{-6}$ for all the eight simulations. The bilinear TSL was used in simulation 8 to check if it was the TSL geometry which was the cause of the numerical simulation problem.

Another improvement attempt was made by changing the viscosity parameter as shown in table 3.4.

Simulation 5	Simulation 2	Simulation 1
10^{-8}	10^{-8}	$2*10^{-8}$
10^{-7}	10^{-7}	10^{-7}
$5*10^{-6}$	$5*10^{-6}$	$5*10^{-6}$
10^{-6}	10^{-5}	10^{-6}
10^{-5}	10^{-4}	
10^{-4}		
10^{-5}		
10^{-2}		
10^{-1}		
1		
10		

Table 3.4: Different viscosity parameters used to improve the crack growth simulation.

$\mathbf{k_i}$**[MPa]**	10^6	$2*10^6$	$6.75*10^6$	$8.4*10^6$	10^7	$2*10^7$

Table 3.5: Different cohesive element initial stiffness used to improve crack growth on clad & C-depl. BM

3.2.8 Material effect on the R-curve

The materials effect on the R-curve were studied by changing the material type in the material sections of the model, as shown in figure figure 3.8 and 3.12.

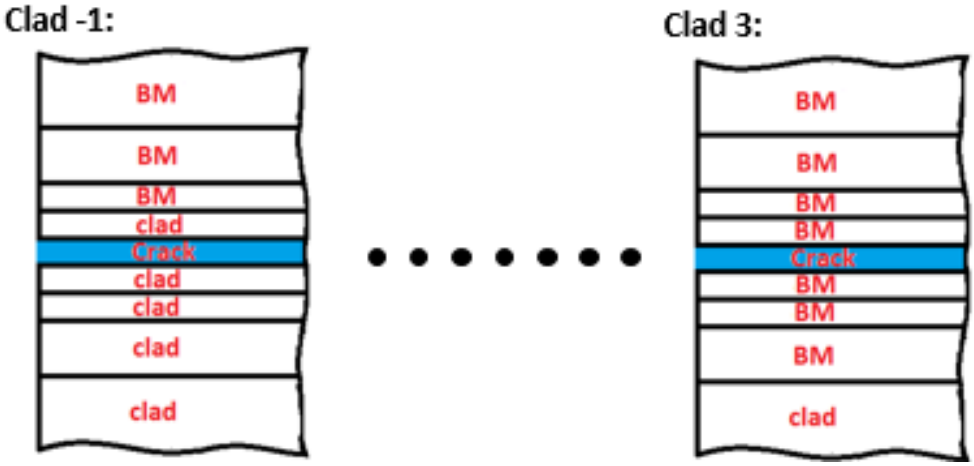

Figure 3.12: Changing material in the different material sections, in the FE-model.

3.3 Materials

The material used in the current thesis are divided into two different sections, given below. The materials used in the experiments and the materials used in the simulations are given their own sections.

3.3.1 Experimental materials

The material types, composition and heat treatment of the samples are given below.

Sample	BM	clad	WM	Interlayer
A	X65	316L	IN625	Nickel
B	X70	316L	Alloy 59, UTP A 759	[-]

Table 3.6: Material types for the test samples.

			[%wt]		
El.	**316L**	**X70**	**X65**	**IN625**	**Alloy 59**	**UTP A 759**
C	0.035	0.16	0.16	0.1	0.001	< 0.01
Cr	16-18	≤ 0.5	≤ 0.5	20-23	22-24	22.5
Ni	10-14	≤ 0.5	≤ 0.5	≥ 58	Bal.	Bal.
Mo	2-3	≤ 0.5	≤ 0.5	8-10	15-16.5	15.5
Si	1	0.1	0.45	0.5	0.1	0.1
Mn	2	1.74	1.65	0.5	0.5	[-]
P	0.045	0.01	0.02	[-]	0.015	[-]
S	0.03	0.001	0.01	[-]	0.01	[-]
V	[-]	[-]	0.09	[-]	[-]	[-]
Nb	[-]	0.03	0.05	3.1-4.1	[-]	[-]
Ti	[-]	0.01	0.06	0.04	[-]	[-]
Cu	[-]	0.21	≤ 0.5	0.5	0.5	[-]
Al	[-]	[-]	[-]	0.4	0.1-0.4	[-]
Other	[-]	[-]	[-]	Fe:5.0	Fe:1.5	Fe:$<$1

Table 3.7: Materials chemical compositions.

	Sample A	**Sample B**
Quenching	$950-980°$, 55min water cooled	N/A
Tempering	$560-590°$C, 1h 25min air cooled	N/A

Table 3.8: Heat treatments of test samples.

3.3.2 Simulation materials

The materials used in the FE-simulations are given below. Note that that the hydrogen diffusion parameters given in table 3.9 does not have any influence on the simulation results. The hydrogen's degree of freedom was removed in all the simulations, which sets the total hydrogen concentration equal to zero, $C_H = 0$.

The material input properties for the FE-simulations are given in table 3.9 and figure 3.13. The Linear elastic material and the carbon depleted BM used the same input data as given for the BM in table 3.9. The material data in figure 3.13 was obtained from experimental tensile tests done by SINTEF. Bjaaland [3] [2] discovered a carbon depleted zone in the base material (BM) along the dissimilar interface, which has a different mechanical property then the BM. The stress-strain curve of the C-depleted BM was found by Jemblie [6] through power law and iteration procedure between numerical simulations and experimental results.

Properties	**Symbol**	**BM**	**clad**
Young's modulus [MPa]	E	208000	167000
Poisson's ratio	ν	0.3	0.3
Diffusitivity $[mm^2/s]$	D_L	$7.6*10^{-5}$ [58]	$2.21*10^{-18}$ [59]
Trap binding energy [kj/mol]	E_B	37 [58]	12 [60]
Molar volume of host lattice $[mm^3/mol]$	V_M	7106	7106
Partial molar volume of H $[mm^3/mol]$	$\bar{V}_H$	2000 [61]	2000
Universal gas constan $[J/Kmol]$	R	8.314	8.314
Temperature (K)	T	293.15	293.15
number of lattice cites per host atom	β	6	6
Initial H concentration $[mol/mm^3]$	C_{LO}	$4.01*10^{-12}$ [62]	$4.01*10^{-12}$
Gibbs energy [Kj/mol]	ΔG_b^0	30 [46]	[-]

Table 3.9: Material inputa data for the FE-simulations.

Properties	Symbol	BM	Clad	C-depl. BM
Yield strength [MPa]	σ_{ys}	493	440	328
Ultimate tensile strength [MPa]	σ_u	595	646.8	[-]

Table 3.10: Other mechanical values.

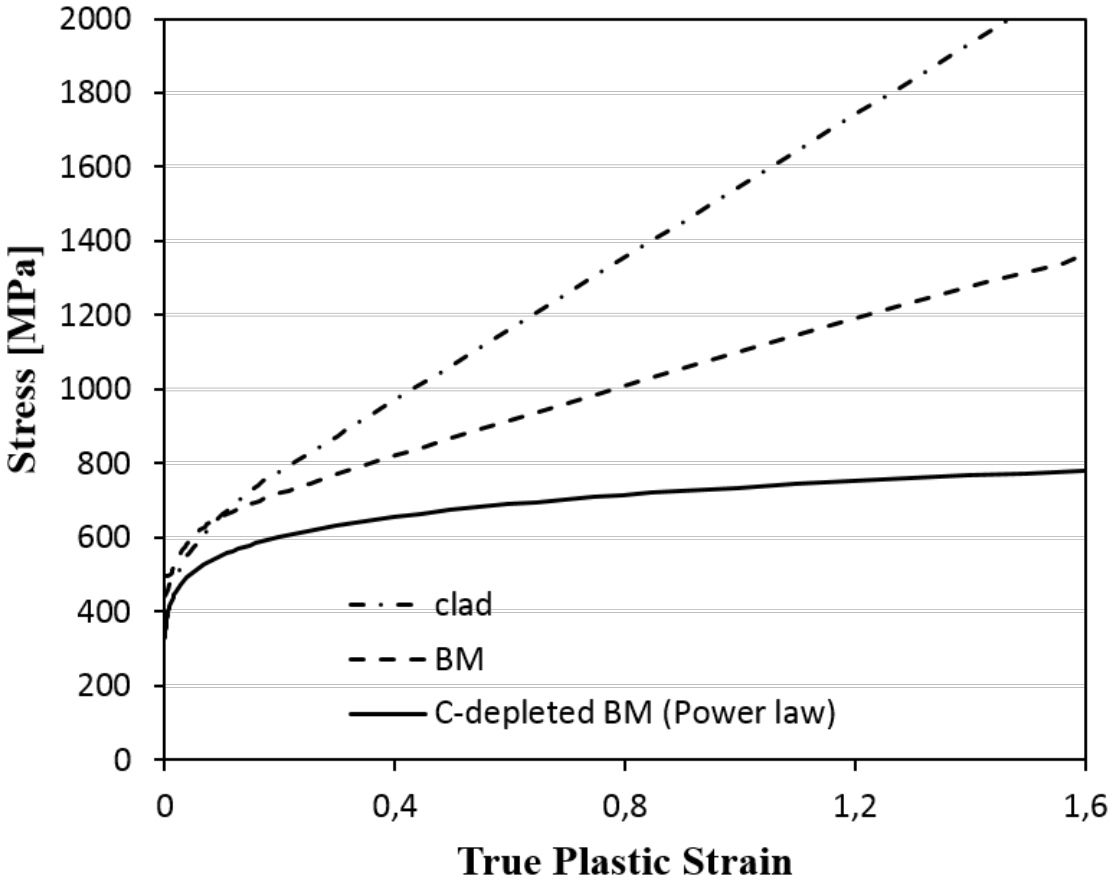

Figure 3.13: Tensile curves

.

4. Results

4.1 Experiments

Experimentally fracture mechanical C(T) tests were successfully conducted in air and under cathodic protection (CP). The experimentally results are tabulated and plotted below. The experiments has also been compared with previous results by Jemblie [1][6] and Bjaaland [4]. The crack path in the B samples are given in section 4.1.3. The crack path in both environments has been investigated in optical light microscope (LOM).

4.1.1 Fracture toughness results

Table 4.1 shows the CTOD at maximum load obtained from tests on sample A and B. Table 4.2 shows the CTOD for the samples tested for fracture resistance curve at the last logged load before the experiment was stopped. The fracture toughness in table 4.1 gives an average reduction in fracture toughness of 0.13% for sample A and 98% for sample B, from testing in air to testing under CP.

Sample	**Environment**	$\mathbf{P_{max}}$ **[N]**	$\mathbf{V_P}$ **[mm]**	$\boldsymbol{\delta_{max}}$ **[mm]**
A9	air	778	0.334	0.071
A10	air	782	0.320	0.07
A11	air	783	0.255	0.056
A15	air	757	0.202	0.046
A12	CP	794	0.247	0.056
A13	CP	796	0.176	0.042
A14	CP	901	0.391	0.084
B6	air	610	0.381	0.188
B9	air	746	1.833	0.321
B10	air	619	0.220	0.108
B3	CP	500	0.029	0.009
B4	CP	542	0.056	0.024

Table 4.1: Values at maximum load for the tested specimens.

Sample	Environment	P_{last} [N]	V_P [mm]	δ_{last}[mm]
A9	air	742	0.368	0.086
A10	air	776	0.325	0.078
A11	air	676	0.321	0.077
A15	air	548	0.358	0.087
A12	CP	790	0.253	0.063
A13	CP	715	0.237	0.060
A14	CP	746	0.648	0.158

Table 4.2: Values at the last logged load before the tests were stopped.

Figure 4.1 and 4.2 shows the load-CMOD curves for the A samples tested in air and in CP respectively. Figure 4.3 shows the load-CMOD curves for the B samples tested in air and under CP. The continuous curves are the specimens tested in air and the dotted curves are the specimens tested under CP. Figure 4.4 shows the fracture resistance curve for the A sample tested under CP. each dot is one test. The blue dot is a test done in air.

Only one test in air was plotted as the crack growth in A9, A10 and A11 were not possible to measure, due to insufficient heat tinting shown in appendix A.4. The fracture resistance curve for the tests in CP is the regression line between the three tests done. The three points gives the following regression line:

$$y = 0.3371X - 0.071 \tag{4.1}$$

Eq. 4.1 gives a fracture initiation toughness equal to, $\delta_{IC} = -0.071mm$.

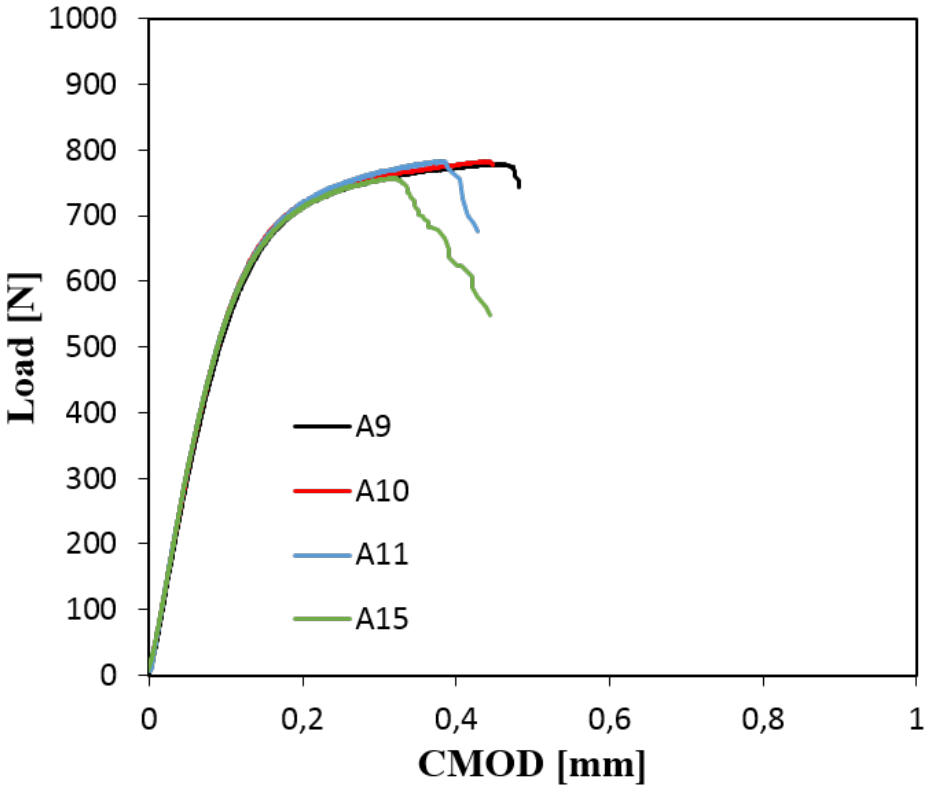

Figure 4.1: Load-CMOD curves for the A samples tested in air.

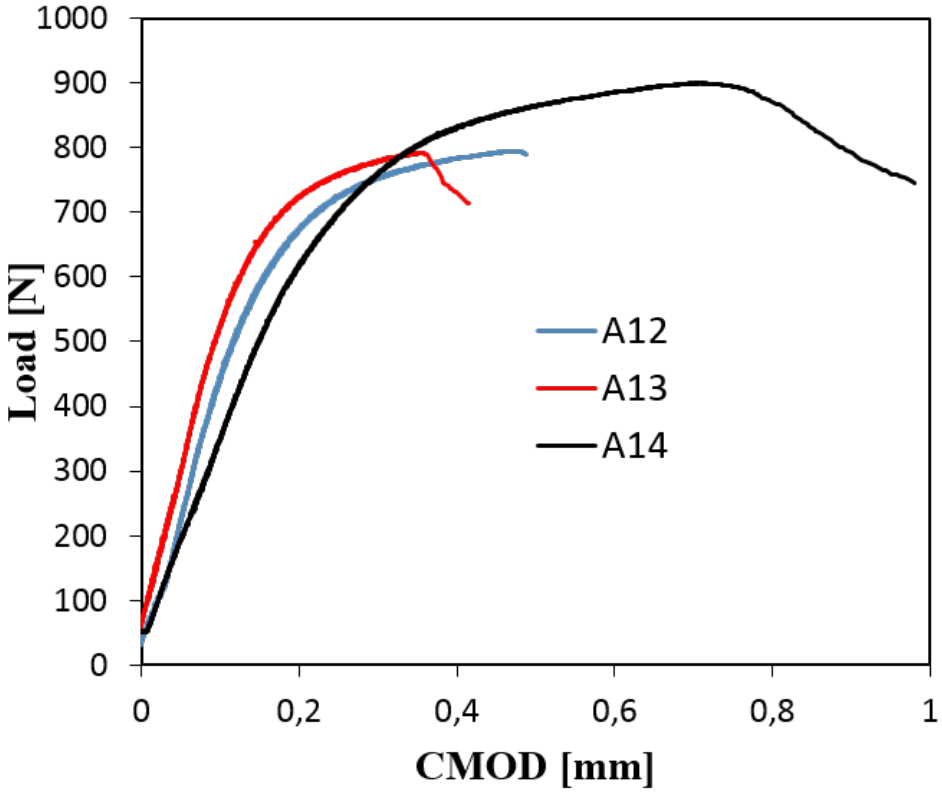

Figure 4.2: Load-CMOD curves for the A samples tested under CP.

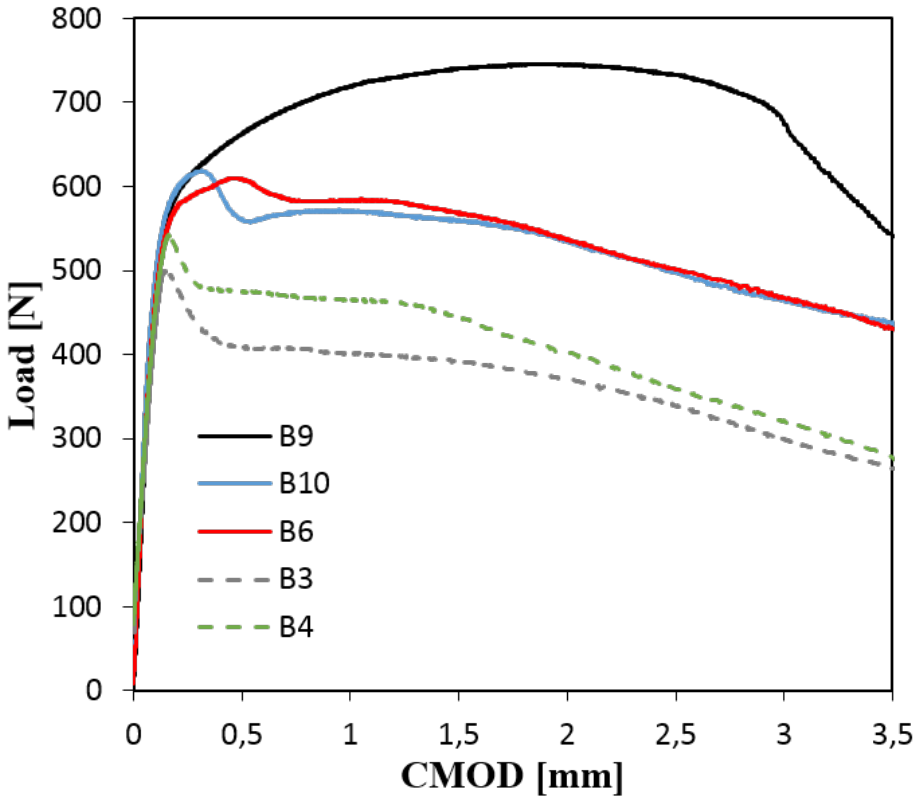

Figure 4.3: Load-CMOD curves for the B samples tested. The continuous curves are the samples tested in air and the dotted curves are the samples tested under CP.

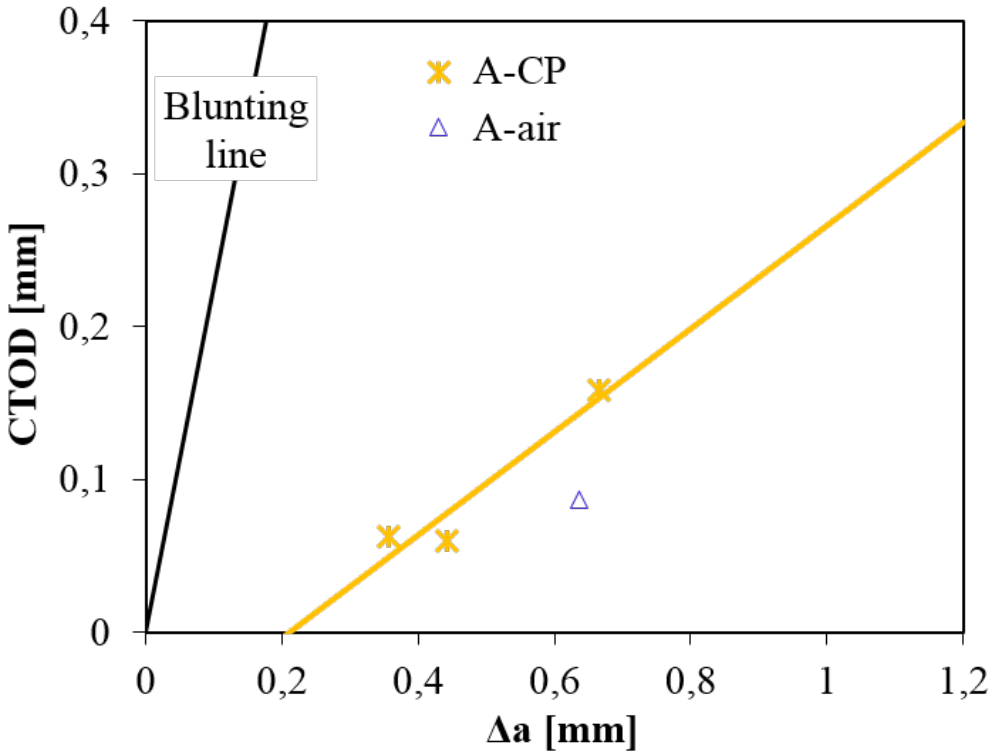

Figure 4.4: Fracture resistance curves for sample A tested in air and under CP.

4.1.2 Comparing with previous results

Figure 4.5 shows the maximum CTOD versus maximum load for the samples tested. The samples called IA is the dissimilar interface samples tested by Jemblie [1] and Bjaaland [4]. Figure 4.6 and 4.7 shows the associated Load-CMOD curves from Jemblie [6]. Pure base material samples (FA,FB) are also included in the Load-CMOD curves.

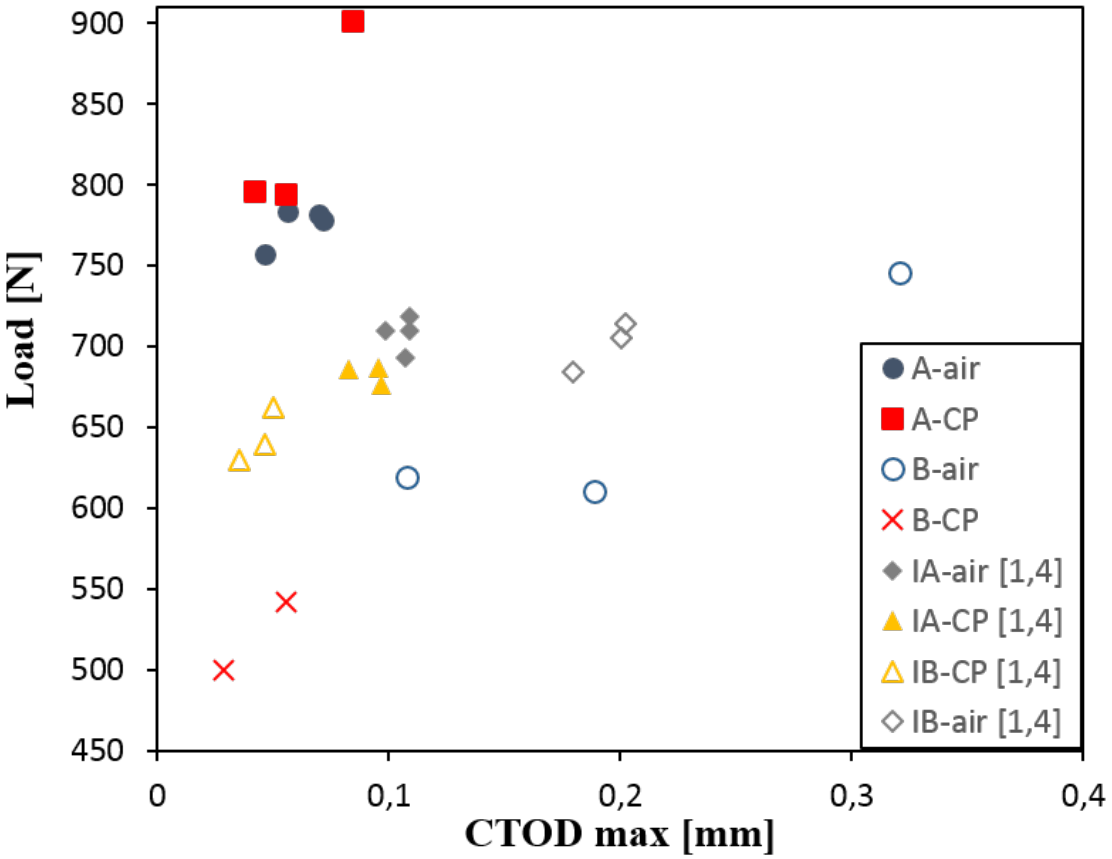

Figure 4.5: Comparing fracture toughness values with previous results by Jemblie [1] and Bjaaland [4].

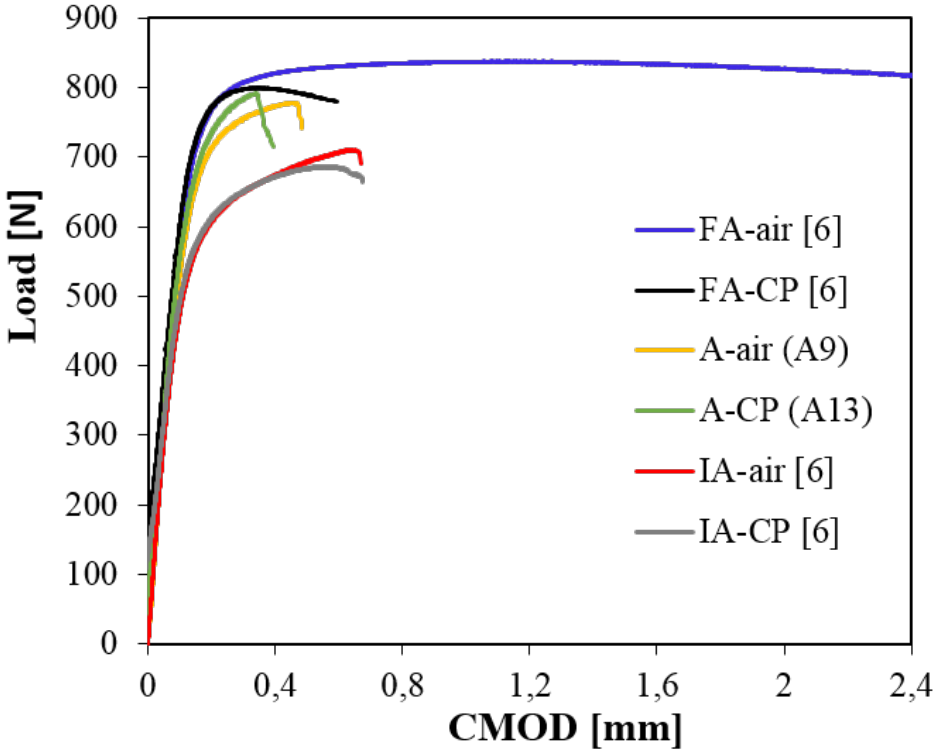

Figure 4.6: Comparing Load-CMOD curves for the A samples with previous results, by Jemblie [6].

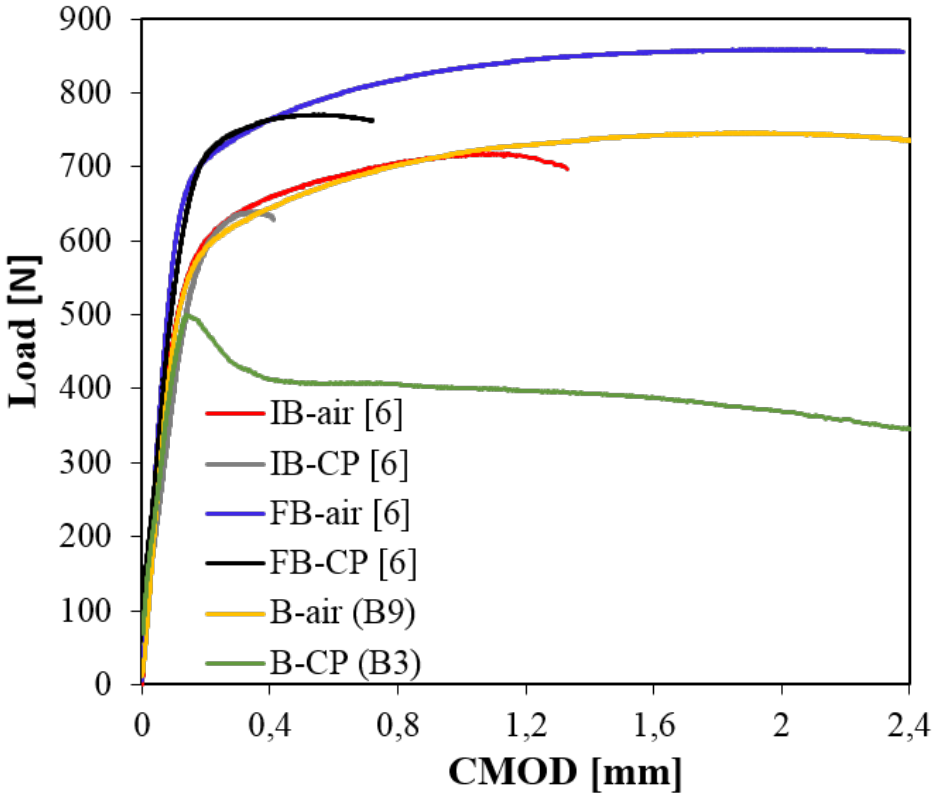

Figure 4.7: Comparing Load-CMOD curves for the B samples with previous results, by Jemblie [6].

4.1.3 Crack path

Figure 4.8, 4.9 and figure 4.10, 4.11 shows the cross section of sample B9 and B3 respectively, investigated in LOM. The figures reveals the crack path close to the machined notched for sample B9 tested in air and sample B3 tested under CP. This was assumed to be the crack initiation area as the stress is presumed highest in the area close to the initial crack tip.

Figure 4.8 and 4.9 shows that the crack has propagated shifting between BM and clad for the sample tested in air. The sample tested under CP seems to have propagated more into the clad as shown in figure 4.10 and 4.11. Figure 4.8 and 4.9 reveals a large plastic deformation at the initial crack tip, on the sample tested in air.

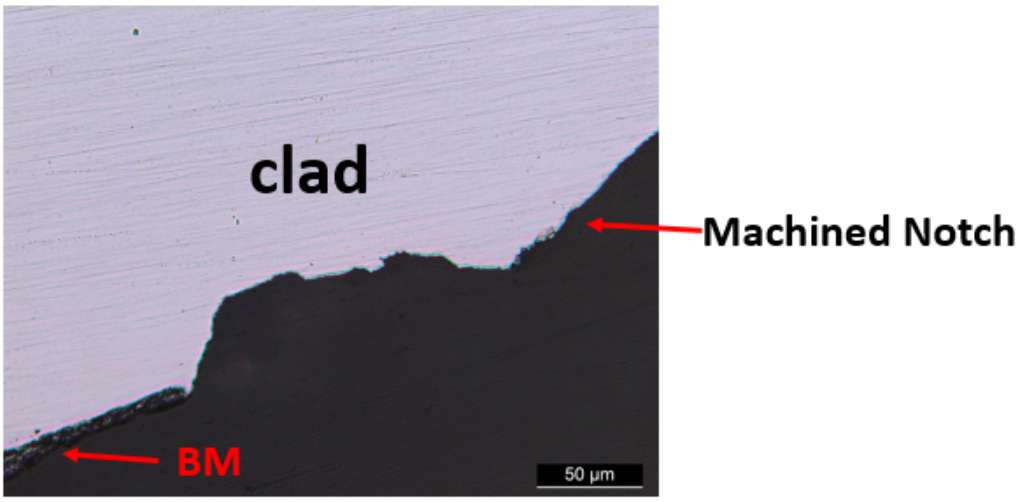

Figure 4.8: Crack path for sample B9 tested in air, clad side.

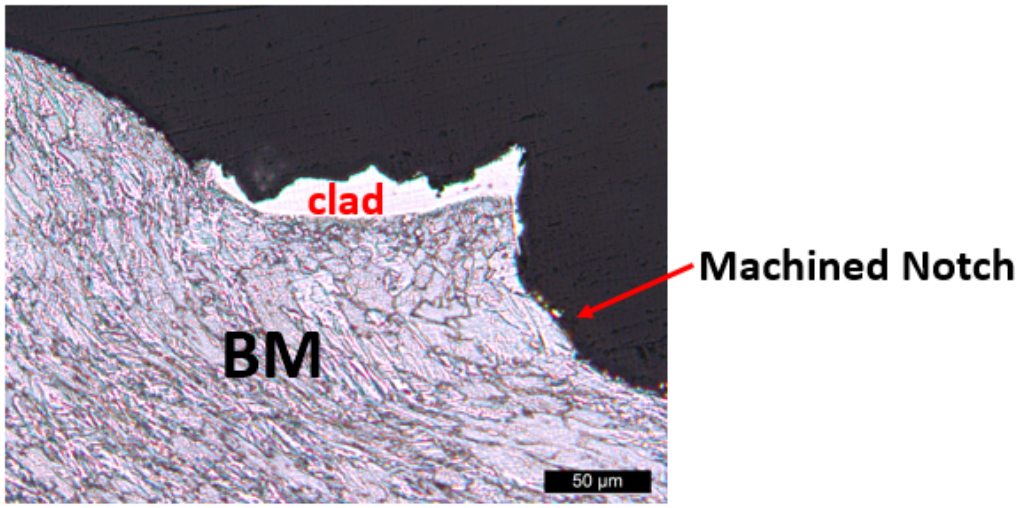

Figure 4.9: Crack path for sample B9, tested in air, BM side.

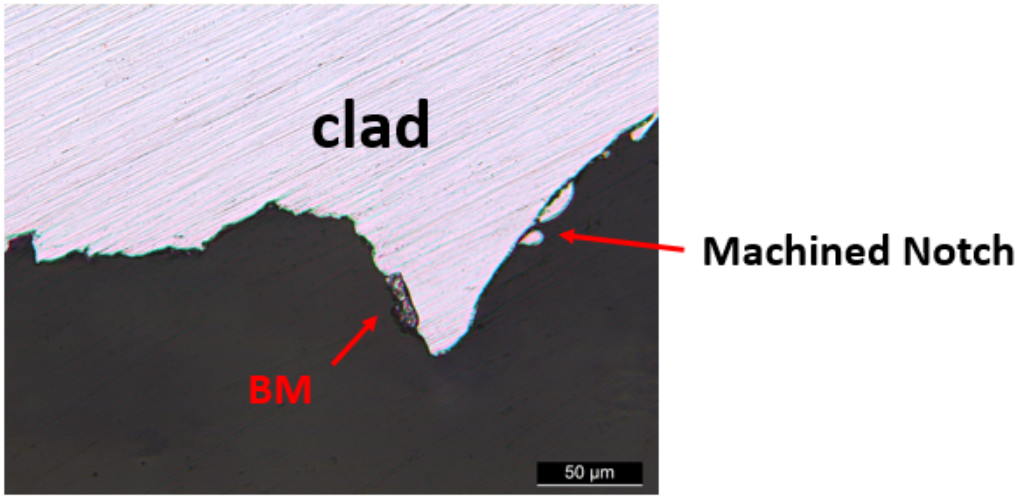

Figure 4.10: Crack path for sample B3, tested under CP, clad side.

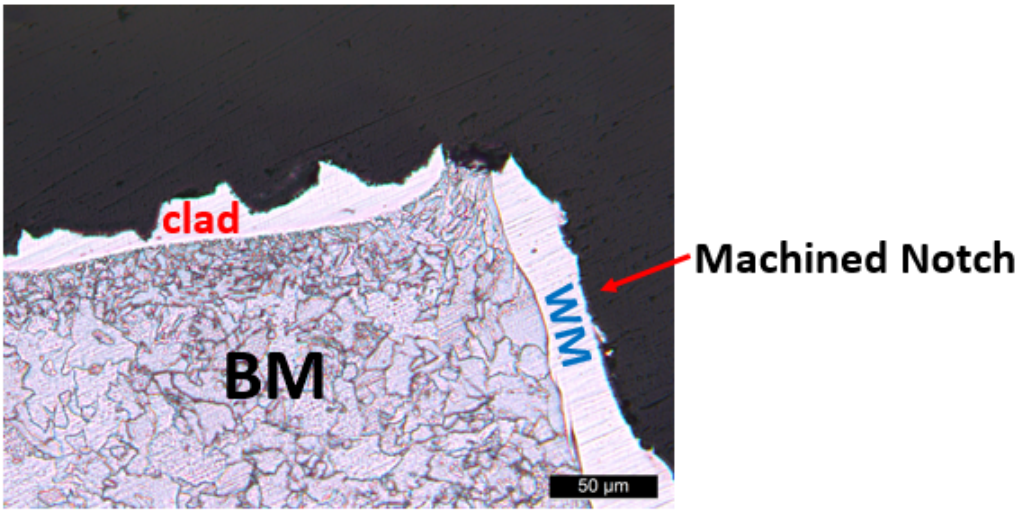

Figure 4.11: Crack path for sample B3, tested under CP, BM side.

4.2 Simulations

The results for the FE-simulations are given in this section. Section 4.2.1 and 4.2.2 shows the results used to find the appropriate element size at the crack tip and the minimum initial cohesive element stiffness, respectively. The crack growth simulations has been numbered to make the simulations more understandably for the reader. A detailed description of the simulation numbers are given in table 3.3 in section 3.2.7. Simulation 6 and 7 were only done for comparison with previous experimental results and is therefore only included in the comparing section 4.2.9. Numerical difficulties occurred when the cohesive parameters were given a more correct value compared to experimentally results. A solution was not found, so no effort was given in trying to run the simulation under hydrogen influence.

4.2.1 Mesh refinement analysis

A Mesh refinement study at the crack tip was conducted too validate the element size. The four simulations with different element size along the crack ligament and at the crack tip are plotted in figure 4.12 and 4.13. Figure 4.12 shows the opening stress and figure 4.13 shows the hydrostatic pressure in a straight line along the crack ligament. The curves in Figure 4.12 and 4.13 are converging between the element sizes equal to $7.5\mu m$ and $3.75\mu m$. Another thing to notice is the dip at the peak opening stress curve for element size $3.75\mu m$.

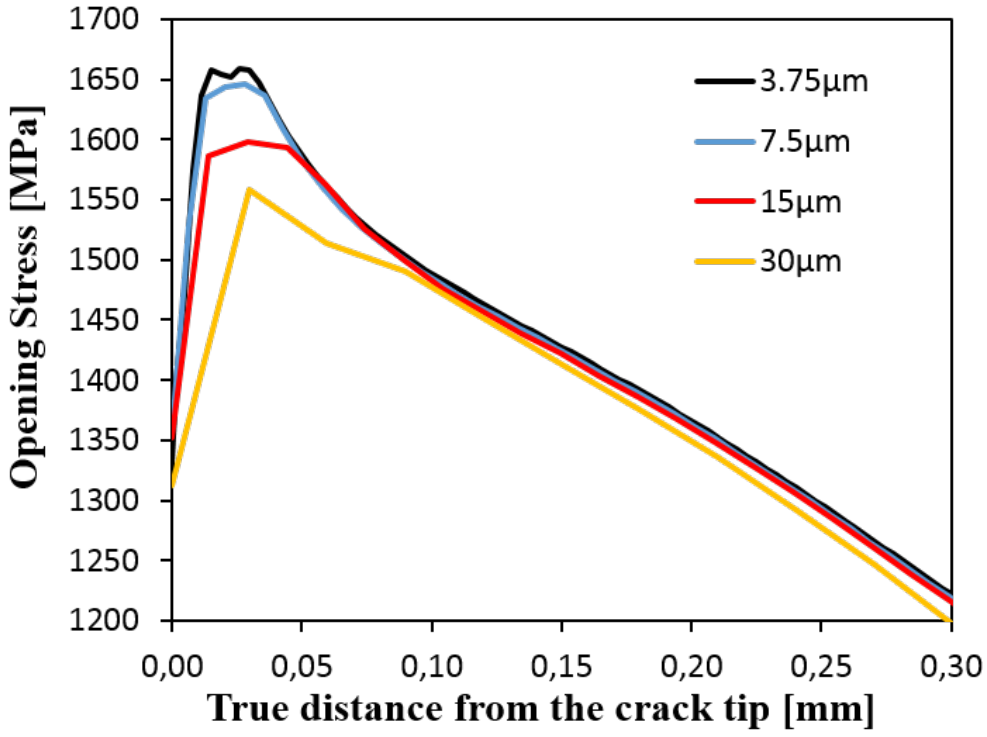

Figure 4.12: Mesh refinement plot, opening stress vs. true distance from the crack tip.

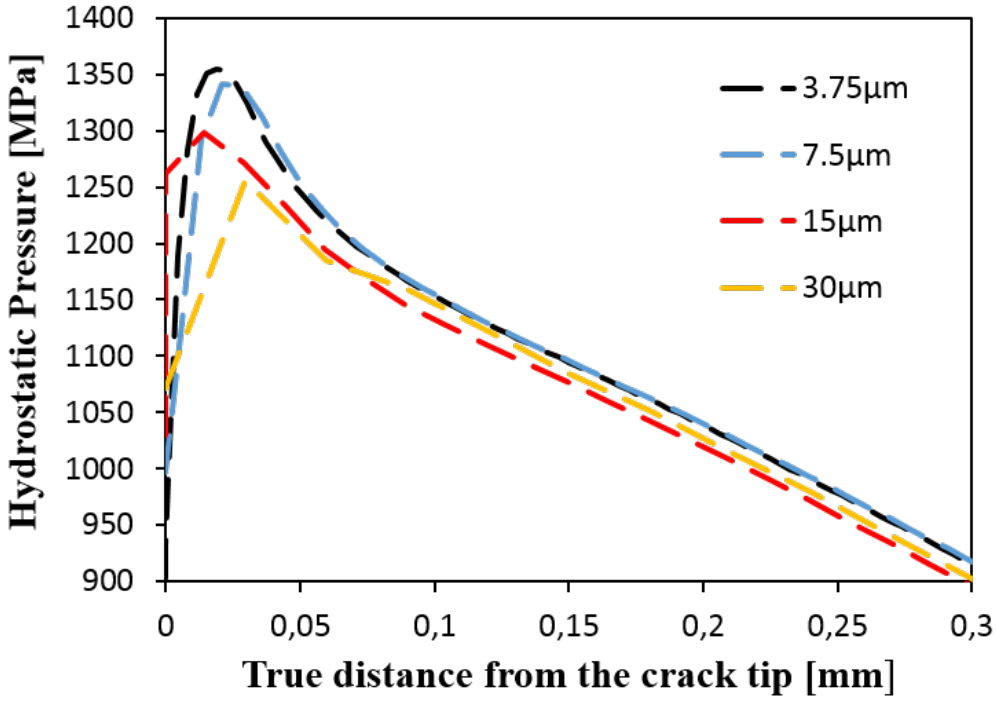

Figure 4.13: Mesh refinement plot, hydrostatic pressure vs. true distance from the crack tip.

4.2.2 Stiffness Verification of the Cohesive Elements

The stiffness of the cohesive elements were verified against a simulation without cohesive elements. The simulations with different initial cohesive element stiffness, and the simulation without cohesive elements are given in figure 4.14 and 4.15. Figure 4.14 shows the opening stress and figure 4.15 shows the equivalent plastic strain in a straight line along the crack ligament. Figure 4.14 and 4.15 shows a god fit between the simulations with and without cohesive elements at a initial cohesive element stiffness of $k_i = 10^7$.

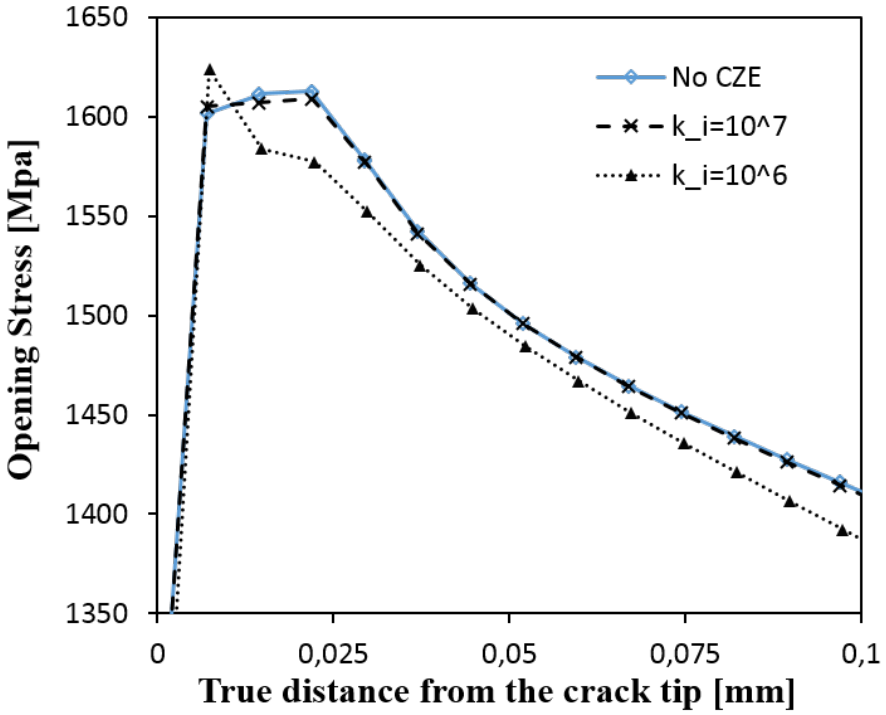

Figure 4.14: Cohesive element stiffness verification plot, opening stress, the continuous curve is the simulation without cohesive elements.

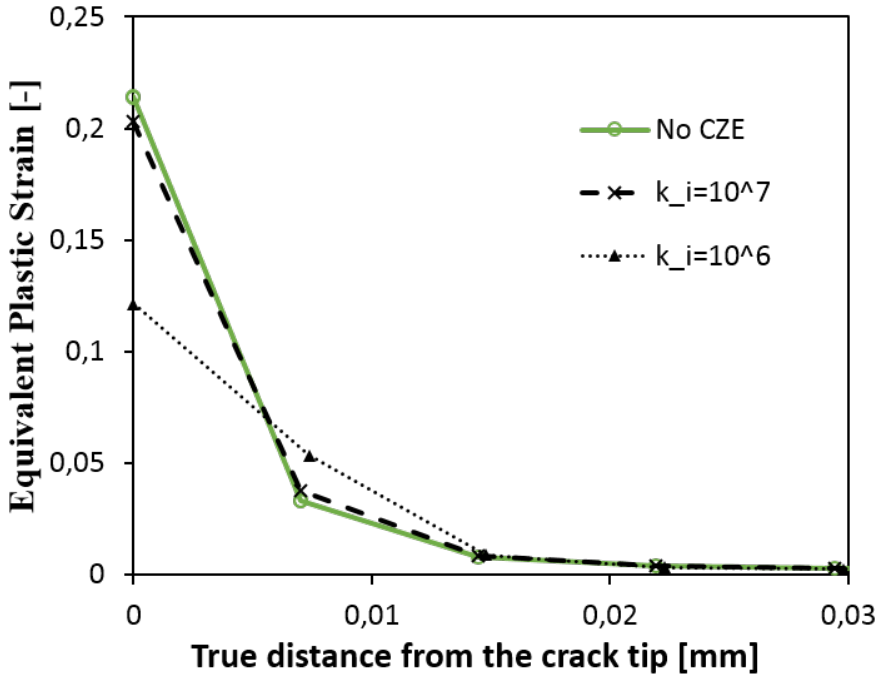

Figure 4.15: Cohesive element stiffness verification plot, equivalent plastic strain, the continuous curve is the simulation without cohesive elements.

4.2.3 Crack growth Simulation 1

The crack was able to propagate through the ligament, as shown in figure 4.16. The simulation was purposely stopped when the crack length was determined long enough. Figure 4.17 shows that the maximum cohesive strength increases as the crack propagates. Figure 4.18 shows the effect of the viscosity parameter on the TSL curve for the element 0.8mm from the initial crack tip. Figure 4.16 shows the stress field in the FE-simulation at the last increment before the simulation was purposely stopped. See table 3.3 in section 3.2.7 for a detailed description of simulation 1's parameters.

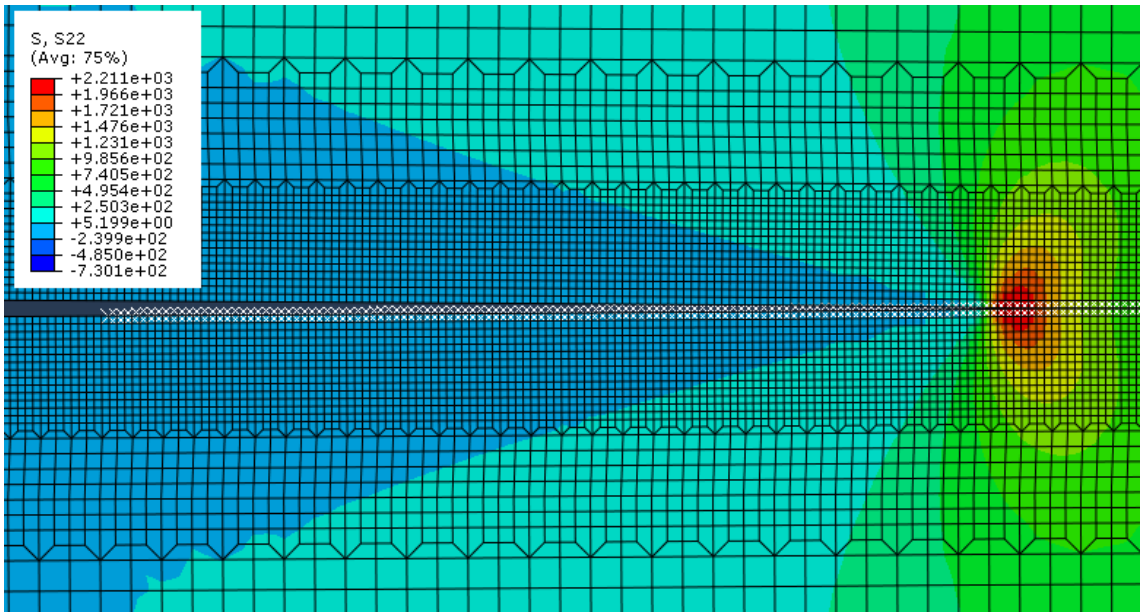

Figure 4.16: Opening stress field in simulation 1 at the last increment before the simulation was purposely stopped. The white crosses is the cohesive element nodes.

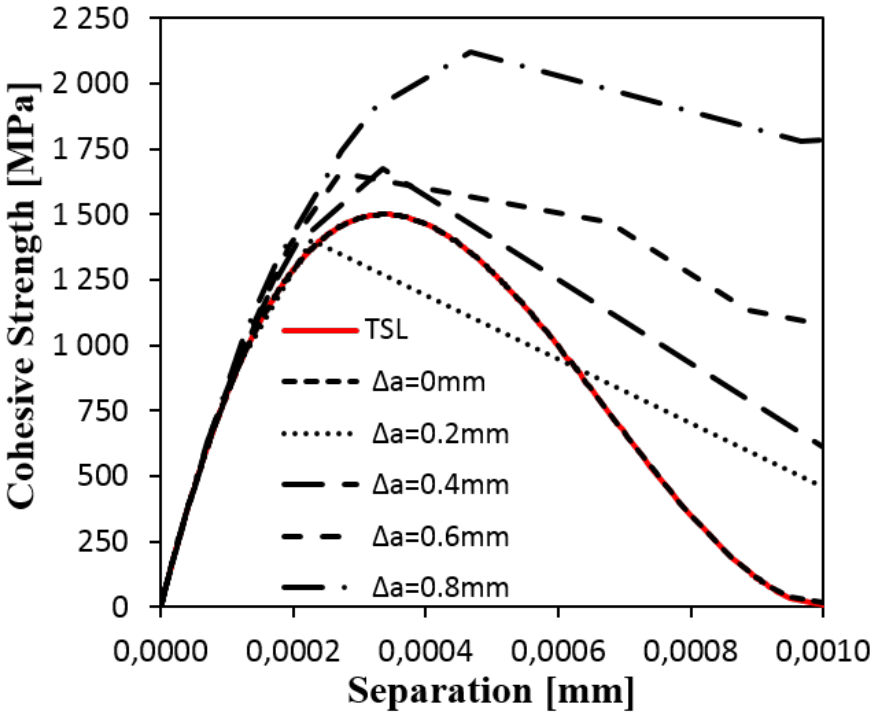

Figure 4.17: TSL curves for simulation 1 for cohesive elements along the crack ligament, with a given distance from the initial crack tip.

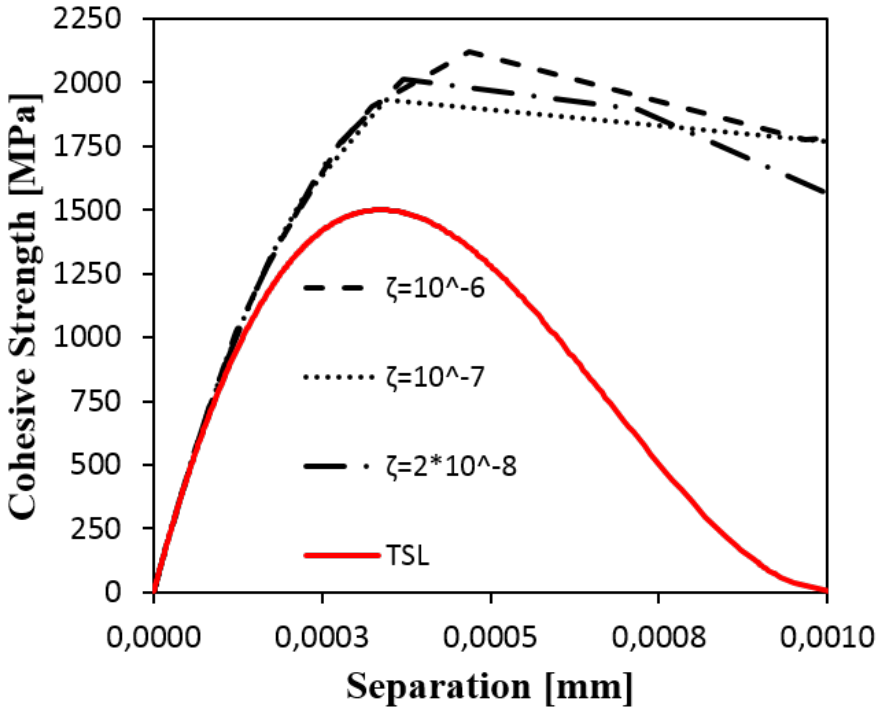

Figure 4.18: Viscosity term‘s effect on the TSL curve at the element 0.8mm from the initial crack tip. The red curve is the theoretical TSL curve.

4.2.4 Crack Growth Simulation 2

The simulation got numerical divergence problems after five cohesive elements failed. Figure 4.19 shows the TSL curve for the element at the crack tip, when the divergence occurred. See table 3.3 in section 3.2.7 for a detailed description of simulation 2's parameters.

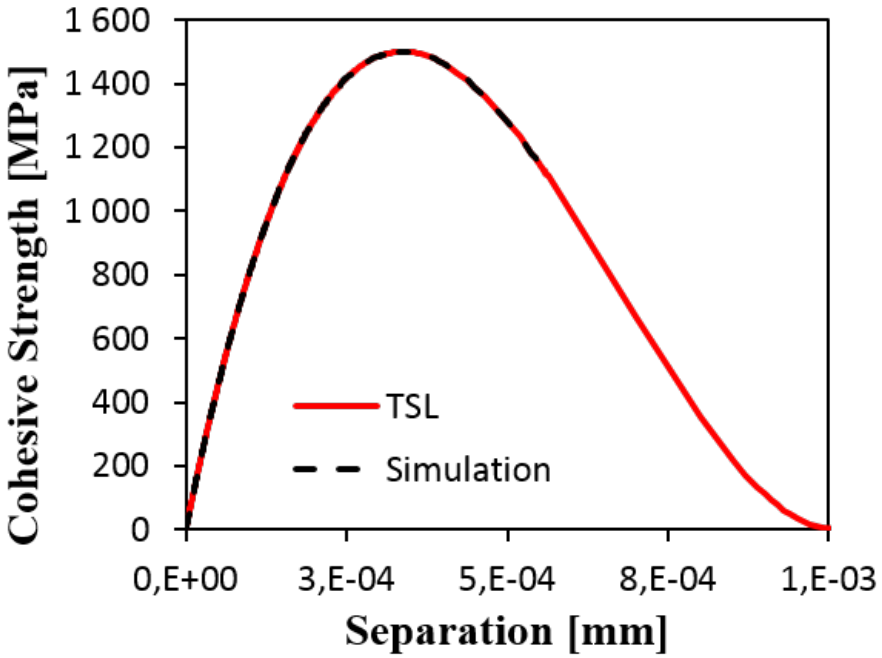

Figure 4.19: TSL curve for simulation 2, the red cure is the theoretical TSL.

An effort in improving the results was done by increasing the viscosity parameter as shown in the appendix section B.2.1.

4.2.5 Crack Growth Simulation 3

The crack propagated successfully until the simulation was purposely stopped. See table 3.3 in section 3.2.7 for a detailed description of simulation 3‘s parameters.

Figure 4.20 and 4.21 shows the opening stress and equivalent plastic strain field at the last increment before the simulation was purposely stopped. Figure 4.22 shows how the maximum cohesive strength increases as the crack propagates.

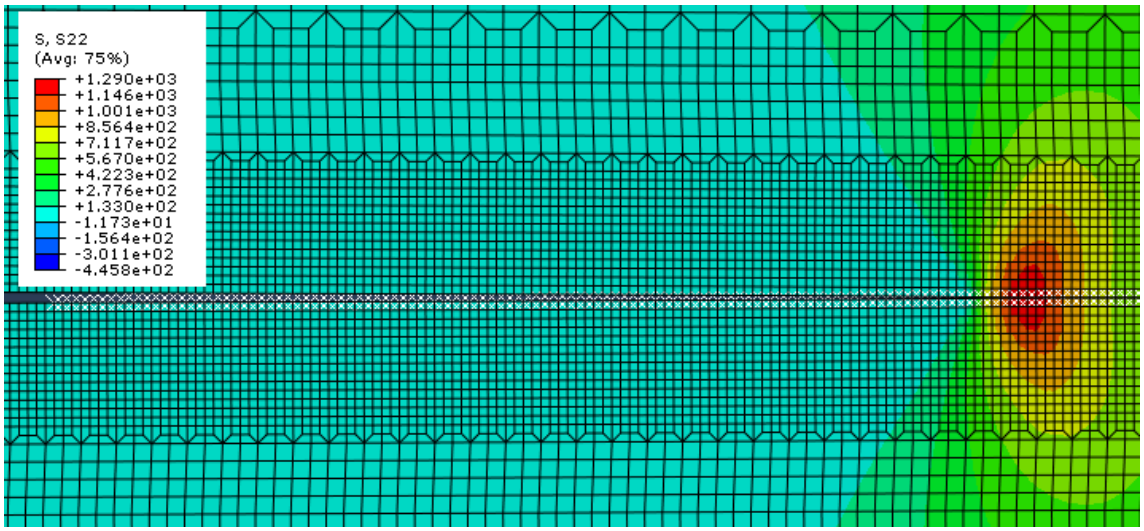

Figure 4.20: Opening stress field for simulation 3 at the last increment before the simulation was purposely stopped.

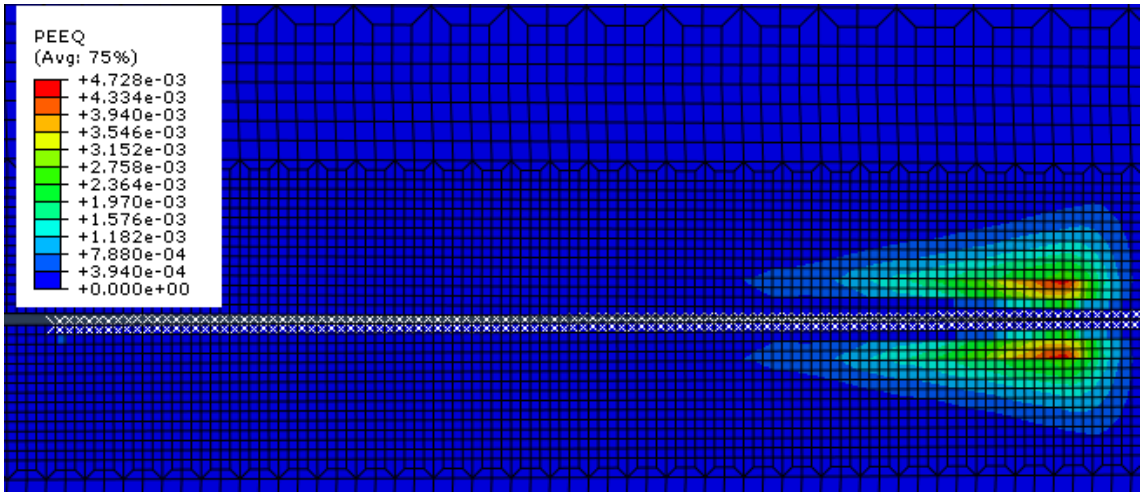

Figure 4.21: Equivalent plastic strain field for simulation 3 at the last increment before the simulation was purposely stopped.

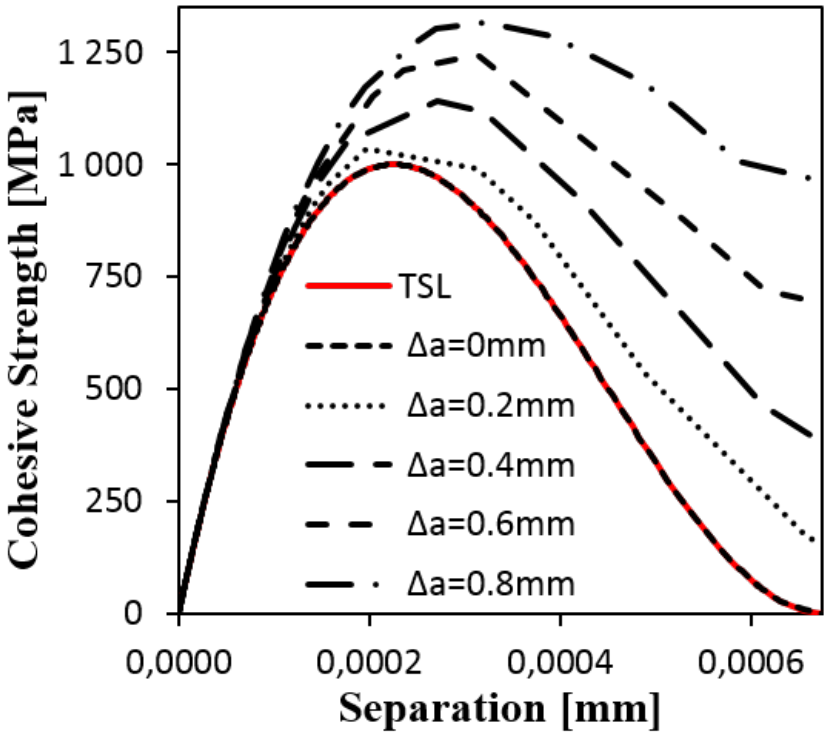

Figure 4.22: TSL curves for simulation 3 for cohesive elements along the crack ligament, with a given distance from the initial crack tip.

4.2.6 Crack Growth Simulation 4

The crack propagated successfully along the crack ligament until it was purposely stopped. Figure 4.23 and 4.24 shows the stress and equivalent plastic strain field in the FE-model respectively, at the last increment before the simulation was purposely stopped. Figure 4.25 shows the fracture resistance curve for simulation 4. See table 3.3 in section 3.2.7 for a detailed description of simulation 4‘s parameters.

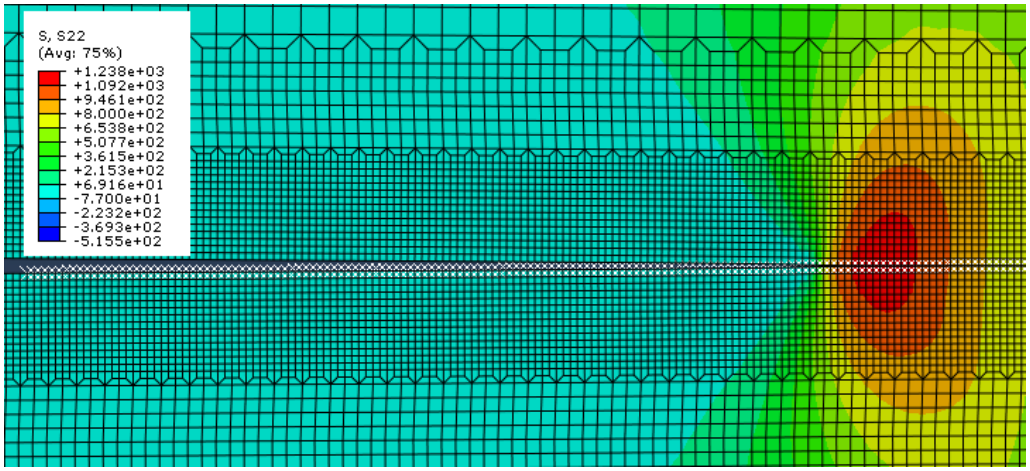

Figure 4.23: Opening stress field in simulation 4 at the last increment before the simulation was purposely stopped.

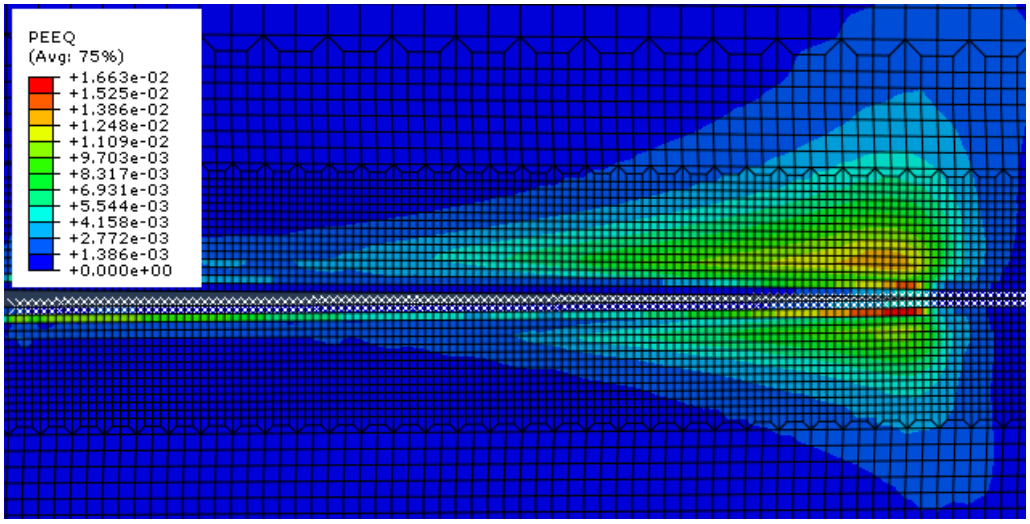

Figure 4.24: Equivalent plastic strain field in simulation 4 at the last increment before the simulation was purposely stopped.

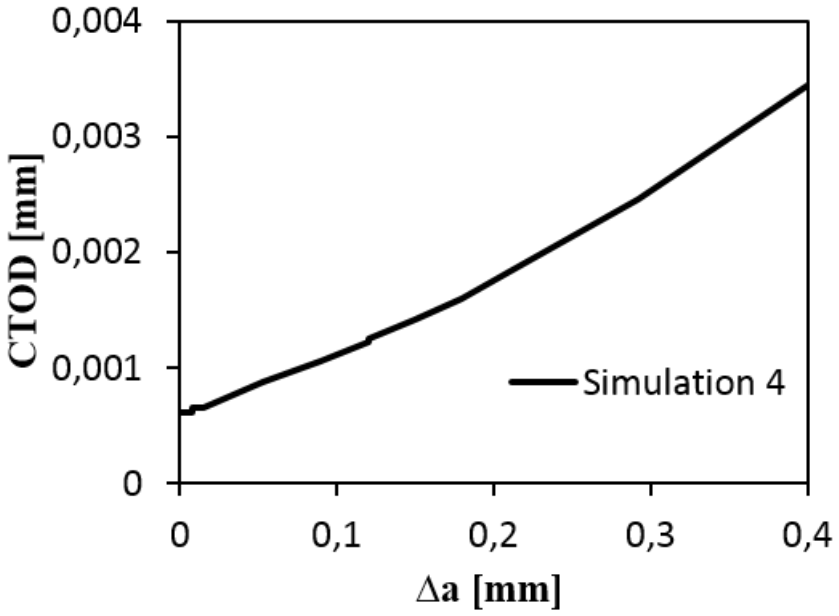

Figure 4.25: Fracture resistance curve in simulation 4.

4.2.7 Crack Growth Simulation 5 and 8

The simulation stopped due to numerical difficulties. Figure 4.26 shows the TSL curve for the element at the crack tip when the simulation stopped. See table 3.3 in section 3.2.7 for a detailed description of simulation 5‘s and 8‘s parameters.

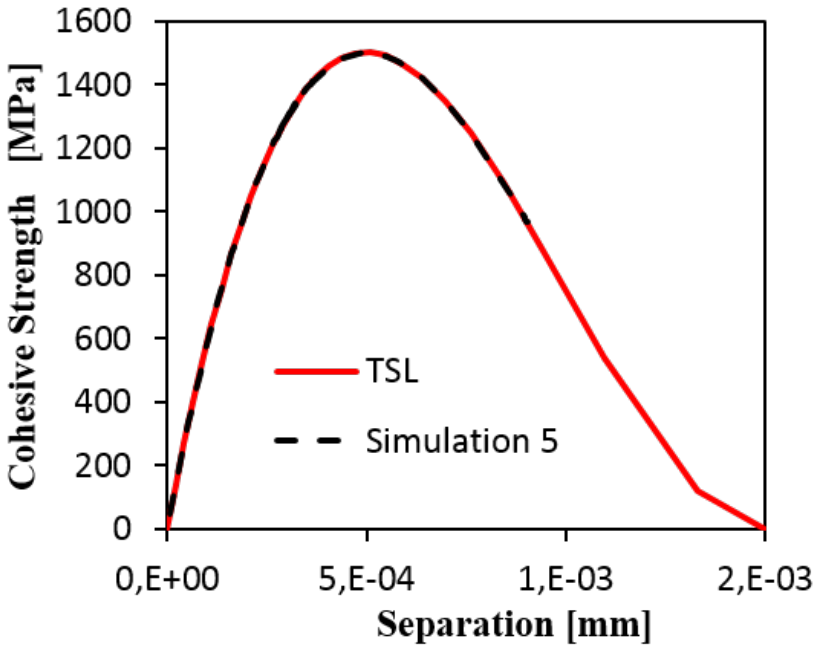

Figure 4.26: TSL curve for the element at the crack tip when the divergence occurred at simulation 5. The red line is the theoretical TSL.

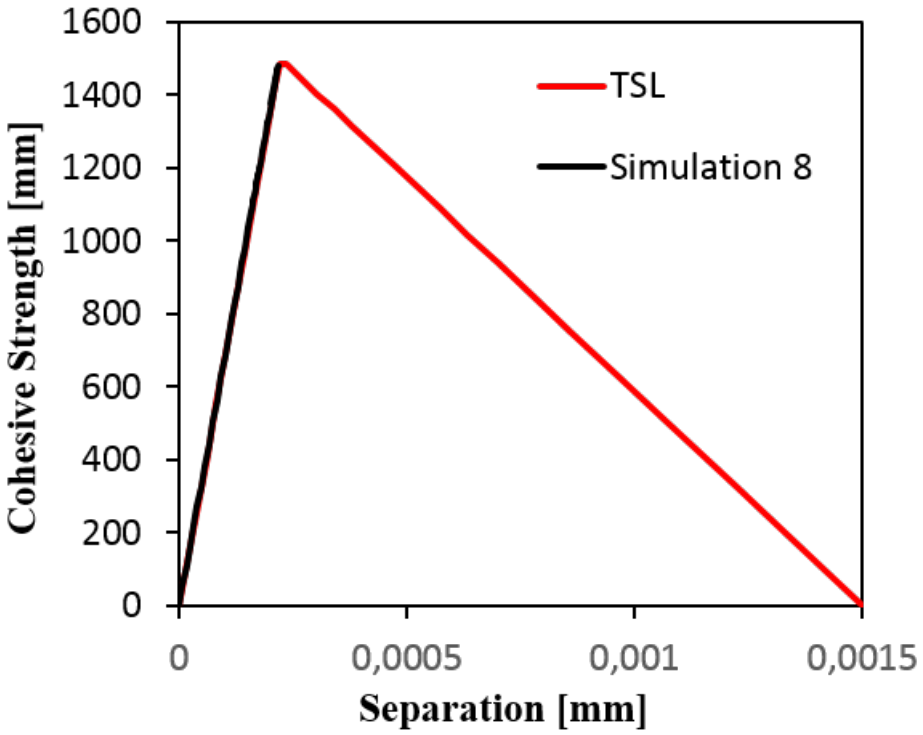

Figure 4.27: Bilinear TSL curve for simulation 8.

4.2.8 Material Effect on the R-curve

Figure 4.28 shows how the CMOD and crack propagation is affected by changing the materials in the material section as shown in section 3.2.2 and 3.2.8.

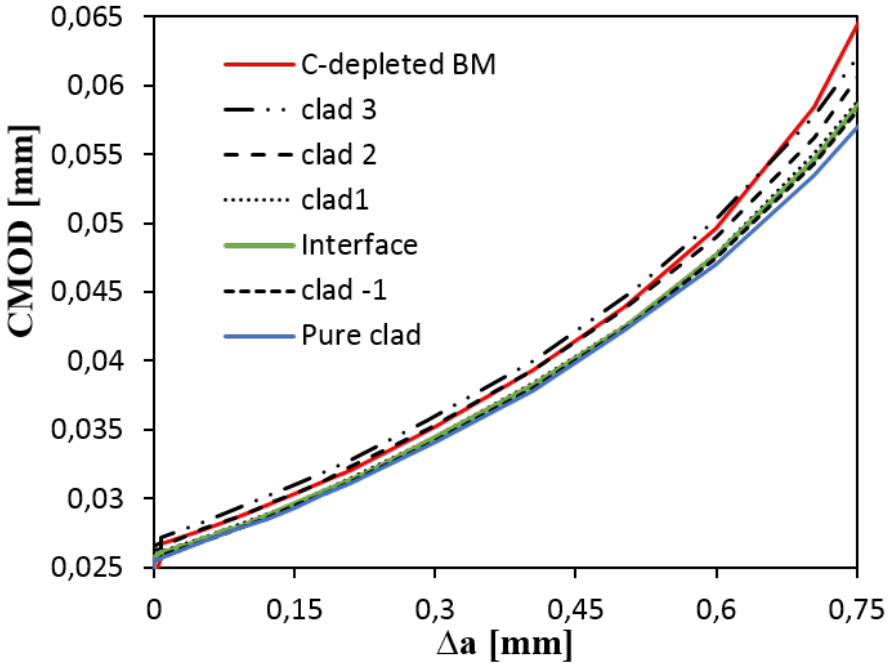

Figure 4.28: Material effect on the R-curve.

4.2.9 Comparing simulations with previous experimental results

A comparison has been done with Jemblie‘s [1][6] results on dissimilar interface samples, without Ni-interlayer, tested in air, to verify the FE-simulations.

The fracture resistance curve from simulation 4 is compared with Jemblie‘s [1] experimental results in figure 4.29. The Load-CMOD curves from simulation 4-7 are similarly compared with experimental results from Jemblie [6] in figure 4.30.

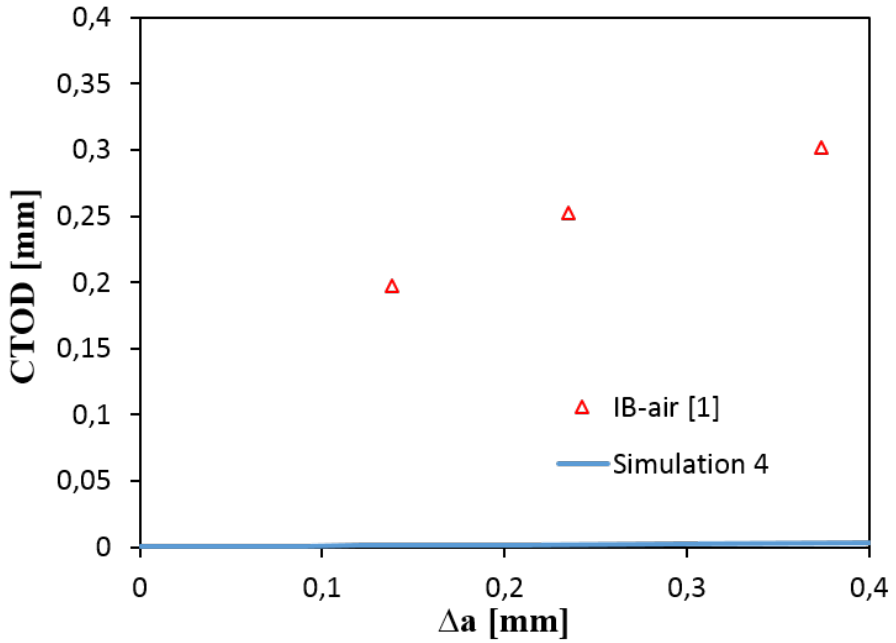

Figure 4.29: Fracture resistance curve from simulation 4 compared with Jemblie‘s [1] experimental results.

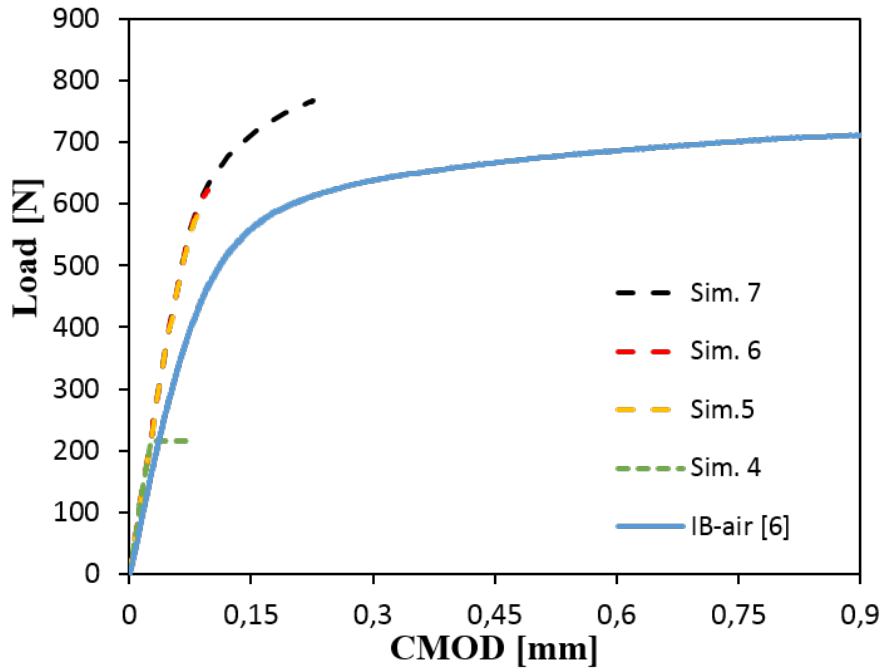

Figure 4.30: Load-CMOD simulation results compared with Jemblie‘s [6] experimental results.

5. Discussion

The Experimental and simulation results are discussed below in individual sections. The experimental samples with Ni-interlayer (sample A) and the samples without Ni-interlayer (sample B) are discussed individually and compared. The crack path are discussed based on the crack path findings in the current thesis and previous results.

5.1 Experiments

5.1.1 A samples

Table 4.1 shows no noticeably difference in the fracture toughness of the A samples at maximum load, with an average reduction in fracture toughness equal to 0.13%, from the tests done in air to the tests done under CP. This indicates that the A samples are not much affected by HISC. This is in accordance with Degos work [5], which also revealed no noticeably hydrogen effect on the fracture toughness, nor on the fractography. A explanation for this is that the crack as shown by Degos [5] propagates along the Ni-interlayer. Nickel is known to not be much affected by hydrogen embrittlement. The clad and Base material might be affected by the Hydrogen but as the crack propagates in the Ni-interlayer, has it not any noticeably influence on the overall fracture toughness. This is also in accordance with Bjaaland‘s [4] and Jemblie‘s [1] findings on the fracture toughness of the dissimilar interface, with Ni-interlayer, which showed only a small reduction in the fracture toughness tested under CP, as shown in figure 4.5.

Comparing the fracture toughness results with Jemblie‘s [1] and Bjaaland‘s [4] results, given in figure 4.1, shows . This is as expected as welding might cause an reduction in the fracture toughness of the clad pipe, as described in section 2.2. Figure 4.6 also reveals a more brittle behavior of the A samples compared to pure BM samples and the interface samples by Jemblie [1] and Bjaaland [4].

Unfortunately, it was only possible to measure the stable crack growth in one sample tested in air, due to insufficient heat tinting shown in appendix A.4. So no fracture resistance curve for the A-sample tested in air could be drawn. The fracture resistance curve under CP gives a negative fracture initiation toughness. This is an unrealistic value as this tells that the crack will already start to grow without adding any load. The negative fracture initiation toughness is caused by test sample A14 which deviated remarkable in fracture toughness, related to the other samples. Some deviation in the results are expected because the weld might have introduced defects and residual stress. This tells that more tests needs to be done to draw a more accurate and realistic fracture resistance curve.

5.1.2 B samples

Table 4.1 shows a large reduction in the fracture toughness of the samples without Ni-interlayer, with an average reduction in fracture toughness equal to 92%, tested under CP compared to tested in air. This indicates that hydrogen influence has occurred during testing. Jemblie [1] and Bjaaland [4] found a reduction in fracture toughness when tested under CP, on the dissimilar interface, without Ni-interlayer, with an average fracture toughness reduction of 77%. This shows that an higher reduction in fracture toughness occur on welded clad pipe samples tested under CP, which indicates that welded clad pipes are more susceptible to HE. This might be explained by theory as the heat affected zone in the carbon steel might be more susceptible to hydrogen embrittlement, as explained in section 2.2. The B sample tested in air shown in figure 4.3, shows an nearly identical curve shape compared to a pure BM. This might only be a coincident but suggests that the carbon steel dominates the fracture behavior when tested in air.

5.1.3 Comparing sample A and B

The samples without Ni-interlayer shows a higher fracture toughness then the specimens with Ni-interlayer. The reason for this might be that the nickel acts as a weak spot for the specimens with Ni-interlayer. When the crack first initiates in the Ni-interlayer it propagates quickly trough the ligament. By the other hand does the Ni-interlayer seem to reduce the risk of HISC, as no noticeably reduction in the fracture toughness could be observed during testing under CP.

5.1.4 Crack path

The crack path on the samples without Ni-interlayer has been successfully studied in a light optical microscope(LOM) .

Figure 4.8 and 4.9 figure shows a shifting crack path between the clad and BM interface, for the sample tested in air. The crack propagates along the clad material in the test done under CP, shown in figure 4.10 and 4.11. This is different then what Bjaaland [4] found for the interface samples. To understand why the crack goes into the clad one needs to study the microstructure of the samples, which is beyond the scope of this thesis. From theory in section 2.2 we known that welding causes a heat affected zone in the base material (BM), which might lead to an embritteled zone in the BM. Bjaaland [2] studied the microstructure of welded clad pipes and found an increased local hardness in the clad close to the interface, which might make the clad more susceptible to cracking. The temperature increase from the welding might also cause residual stresses along the interface due to different temperature expansion coefficient for the BM and clad. The local brittleness of the carbon steel becomes further increased by hydrogen as carbon steel with BCC crystal structure is more susceptible to hydrogen embrittlement than the stainless steel with FCC crystal structure, described in section 2.3.4. As the brittleness of the carbon steel increases the clad might become more susceptible to cracking in relation to the base material. This is in accordance with what was experienced, as figure 4.10 and

4.11 shows that the crack propagates more into the clad when subjected to hydrogen.

The air sample investigated in LOM shows a much more ductile behavior then the two other samples, shown in figure 4.5. This questions if this sample are representative for the condition occurring in welded clad pipes, so more samples should be investigated in LOM to check if the crack follows a similar path.

5.1.5 Hydrogen susceptibility

More samples needs to be tested and be examined in LOM and scanning electron microscope (SEM) before any conclusion can be drawn on the hydrogen susceptibility of welded clad pipes.

4.1 shows a large scatter in the results, especially B samples tested in air, which sets the need for more tests to find a more representative fracture toughness. The fractography should also be examined in SEM to reveal changes in the fracture, between tests done in air and under CP. The microstructure must also be checked to verify that the B samples are representative to the welded condition occurring in welded clad pipes. Welding and several individual materials in the samples gives a complex picture, so caution must be made before concluding on hydrogen susceptibility of welded clad pipes.

Appendix A.4 shows samples that contained large welding defects. Even if no defects are currently found in the samples plotted in the results, are undetected defects quite plausible.

5.2 Simulations

5.2.1 Model verification

The FE-model consists of several parameters that needs to be calibrated in order to get accurate results. The curves in Figure 4.12 and 4.13 shows that the stress and hydrostatic pressure respectively are converging between the element sizes $7.5\mu m$, $3.75\mu m$ at the crack tip. One should also notice the dip at the peak opening stress curve for element size $3.75\mu m$. A reason for the dip in the curve might be as mentioned earlier that the displacement in the crack tip elements becomes to high so they becomes unstable. Based on this results does the elements size of $7.5\mu m$ at the crack tip seem to be the correct element size for this simulation. Figure 4.14 and 4.15 shows that the opening stress and equivalent plastic strain are converging against the simulation without cohesive elements at $k_i = 10^7$. Based on this does the initial cohesive stiffness of $k_i = 6.75 * 10^6$ seem to be okay.

5.2.2 Crack growth simulations

Simulation 1,3 and 4 were able to propagate successfully along the crack ligament until they were purposely stopped. The opening stress plot in figure 4.16 and 4.20 shows that a high stress concentration occurs at the crack tip. Figure 4.21 shows that an plastic wake occurs as the crack propagates. This is in contrast to Islam's [55] parameter study on cohesive element, which showed no plastic wake as the crack propagated. Figure 4.17 and 4.22 shows that the maximum cohesive stress increases as the crack propagates. This is most likely caused by the viscosity scheme. As the crack propagates the more and more energy becomes absorbed by the viscosity scheme which pushes the maximum cohesive strength more and more above the predetermined critical cohesive stress. An effort in improving the TSL curve was done by decreasing the viscosity parameter, but with an quite small effect as shown in figure 4.18, for the element 0.8mm from the initial crack tip.

Simulation 2 and 5-8 stopped due to numerically difficulties after only a few elements had failed. The numerical difficulties seems to appear in the softening part of the curve for simulation 2 and 5 and at the top point in simulation 8. Changing the viscosity parameter shows close to zero effect on the divergence problem, shown in appendix B.2. This tells that the viscosity scheme is not able to affect the element that reaches divergence. If the viscosity scheme was affecting the TSL curve, we should see an increase of the maximum cohesive strength. Due to an increased absorption of energy, as explained in section 2.5.3. The problem might rather be caused by a global instability occurring in the model. The viscosity scheme has only been developed to stop local instabilities and might not be able to stop the instability if it is global. The bi-linear TSL curve also reached divergence after a few elements had failed, which indicates that the TSL geometry is not the source of this problem. Changing the initial cohesive element stiffness was also done without any improvement in the results, shown in appendix B.3.

The problem seems to be in handling the plastic strain, as simulation 1, 3 and 4 was able to propagate the crack successfully along the ligament. Given simulation 1 had only linear elastic materials implemented, and simulation 3 and 4 had a quite low critical cohesive stress, so element failure occurred with only a small plastic displacement in the cohesive elements. The root cause of this problem is beyond the scope of this thesis and needs to be further studied. Figure 4.30 shows that a higher critical cohesive stress needs to be used in order to simulate a realistic crack propagation compared to experimental results. The cohesive element tool is primarily developed to simulate crack initiation and not crack propagation [55], so this tool might simply not be usable for this cause. But a deeper study on this problem must be done to draw any absolute conclusion. The user-subroutine [57] are newly developed and might contain errors. Scheider [63] seems to have been able to to use cohesive elements to simulate crack propagation, but by the look of his curves that shows a step-wise form it seems to have been done by doing multiple crack initiation simulations and removing cohesive elements [63]. Due to the numerical problems occurring without hydrogen influence was it not given an effort in trying to run simulations with hydrogen introduced.

The material effect on the R-curve was checked by changing the materials in the material sections. Figure 4.28 shows only a small change in the R-cuve when changing the ma-

terials. The small change in the R-curve might mean that the cohesive elements are not much affected by the mechanical properties of the continuum elements, surrounding the cohesive elements.

6. Conclusion

6.1 Experiments

Fracture mechanical testing of welded clad pipe C(T) samples have been successfully conducted, in air and under cathodic protection (CP). The cross-section of samples tested in both environemt have been investigated in a light optical microscope (LOM), to reveal the crack path. Based on the experimental work and discussion can the following conclusion be drawn:

- The samples with Ni-interlayer showed an average reduction in fracture toughness of 0.13%, from the tests done in air to the tests done under CP. The small reduction in fracture toughness may be explained by the crack path found in previous work by degos [5]. The crack propagates along the Ni-interlayer which is not much influenced by hydrogen embrittlement.
- The crack growth curves for the samples with Ni-interlayer was not possible to establish, due to a large scatter and non measurable stable crack growth results.
- The samples without Ni-interlayer showed an average reduction in fracture toughness equal to 92%, from the tests done in air to the tests done under CP. 92% reduction in fracture toughness is higher then what was shown by previous results on the dissimilar material interface, and might suggest that welded clad pipes are more susceptible to hydrogen embrittlement.
- The Ni-interlayer seems to successfully reduce the risk of hydrogen induced stress cracking on welded clad pipe samples (HISC), but simultaneously decrease the fracture toughness.
- The samples without Ni-interlayer investigated in LOM showed a crack path shifting between clad and base material tested in air, and a crack path going primarily into the clad tested under CP. Due to a large scatter in the fracture toughness results should the cross-section of more samples be checked before concluding on a given crack path.

More samples must be tested and examined in LOM and SEM before conclusions on hydrogen susceptibility of welded clad pipes can be drawn, due to the complexity of the samples, the few number of samples tested and the large scatter in the results.

6.2 Simulations

FE-modelling of a 2D C(T) sample containing a sharp crack has been modeled. Crack propagation simulations have been done through implemented cohesive zone elements (CZE), along the crack ligament, based on a traction separation law (TSL). Coupled temperature-displacement simulations have been done with materials representative for clad pipes, at the dissimilar material interface, without Ni-interlayer. An effort in improving the simulation results compared to previous experiments has been done through calibration of cohesive elements. Due numerical difficulties were only simulations without hydrogen influence done. Based on the simulation work and discussion can the following conclusions be drawn:

- The element size and cohesive element stiffness was successfully calibrated.
- The simulations managed to simulate crack propagation successfully with linear elastic materials or with only a small degree of plasticity in the simulation.
- The coupled temperature-displacement simulation seems to have some limitations regarding simulating crack propagation with elastic-plastic materials, stopping due to numerical difficulties after a few elements has failed.
- Due to the numerical problem was it not possible to simulate the crack propagation occurring in previous tested dissimilar material interface clad pipe samples, without Ni-interlayer, tested in air.
- Viscous regulation scheme showed no effect on the numerical simulation problem, indicating a global instability problem.
- The R-curve seems to not be much affected by changing the materials in the material sections. Indicating a small material impact from the continuum elements on the cohesive elements.

7. Further Work

- Do more fracture toughness C(T) test in both air and under CP to find a more representative fracture toughness and draw the fracture resistance curve for the A and B samples, both with and without hydrogen influence.
- Study the fractography of all the tested samples in SEM to look for welding defects and type of fracture. A more brittle fracture in the CP samples then in the air samples will back up prof of hydrogen influence.
- investigate the cross section of all the samples in LOM to check if the crack follows the same path for all the samples.
- Investigate the microstructure of the B samples to check if the B samples can be representative for welded clad pipes.
- Try to run this FE-model through Yu‘s [44] script, which is based on scheiders script [40], to check if the crack propagation simulation works in a static analysis.
- Study why plastic strain might cause numerical difficulties in a cohesive element simulation.
- Overlook the user subroutine [54] for possible errors.

References

[1] L Jemblie et al. “Fracture toughness and hydrogen embrittlement susceptibility on the interface of clad steel pipes with and without a Ni-interlayer”. In: *Materials Science and Engineering: A* 685 (2017), pp. 87–94.

[2] Helana Bjaaland. “Metallurgical reactions in welding of clad X60/X65 pipelines”. Norwegian University of Science and Technology (NTNU), 2014.

[3] Helena Bjaaland et al. “Metallurgical reactions in welding of clad X60/X65 pipelines”. In: *The Twenty-fifth International Offshore and Polar Engineering Conference*. International Society of Offshore and Polar Engineers. 2015.

[4] Helana Bjaaland. “Evaluation of Welded Clad Pipes- Microstructure and Properties”. MA thesis. Norwegian University of Science and Technology (NTNU), 2015.

[5] Martin Degos. “Influence of hydrogen embrittlement on welded clad X60/65 pipelines”. unpublished internship report at SINTEF. 2016.

[6] Lise Jemblie et al. “Hydrogen Embrittlement susceptibility of Clad Steel Pipes”. In: *ASME 2017 Pressure Vessels and Piping Conference* (2017). **IN PRESS**.

[7] Offshore Standard. *Submarine Pipeline Systems*. Tech. rep. DNV-OS-F101, DNV, 2000.

[8] Thilo Reichel et al. “Production of Metallurgically Cladded Pipes for High End Applications in the Oil and Gas Industry”. In: *ASME 2008 27th International Conference on Offshore Mechanics and Arctic Engineering*. American Society of Mechanical Engineers. 2008, pp. 179–186.

[9] Yu-an Jing et al. “A novel reduction-bonding process to fabricate stainless steel clad plate”. In: *Journal of Alloys and Compounds* 617 (2014), pp. 688–698.

[10] Dominique Kaplan and Guy Murry. “Thermal, Metallurgical and Mechanical Phenomena in the Heat Affected Zone”. In: *Metallurgy and Mechanics of Welding: Processes and Industrial Applications* (2008), pp. 89–131.

[11] Ted L Anderson and TL Anderson. *Fracture mechanics: fundamentals and applications*. CRC press, 2005.

[12] Alexander R Troiano. “The role of hydrogen and other interstitials in the mechanical behavior of metals”. In: *Metallography, Microstructure, and Analysis* 5.6 (2016), pp. 557–569.

[13] Richard A Oriani. “The diffusion and trapping of hydrogen in steel”. In: *Acta metallurgica* 18.1 (1970), pp. 147–157.

[14] WW Gerberich, PG Marsh, and JW Hoehn. “Hydrogen induced cracking mechanisms—are there critical experiments?” In: *Hydrogen Effects in Materials* (1996), pp. 539–554.

[15] Stan Lynch. “Hydrogen embrittlement phenomena and mechanisms”. In: (2012).

[16] SP Lynch et al. “Progress towards understanding mechanisms of hydrogen embrittlement and stress corrosion cracking”. In: *CORROSION 2007*. NACE International. 2007.

[17] Howard K Birnbaum and Petros Sofronis. “Hydrogen-enhanced localized plasticity—a mechanism for hydrogen-related fracture”. In: *Materials Science and Engineering: A* 176.1-2 (1994), pp. 191–202.

[18] Vigdis Olden, C Thaulow, and R Johnsen. “Modelling of hydrogen diffusion and hydrogen induced cracking in supermartensitic and duplex stainless steels”. In: *Materials & design* 29.10 (2008), pp. 1934–1948.

[19] Einar Bardal. *Korrosjon og korrosjonsvern*. Tapir Akadameisk Forlag, 2001.

[20] Roy Johnsen. “Catodic protection”. Lecture notes in Corrosion TMM4170. 2015.

[21] Roy Johnsen, Bård Nyhus, and Stig Wästberg. “Hydrogen Induced Stress Cracking (HISC) of Stainless Steels Under Cathodic Protection in Seawater: Presentation of a New Test Method”. In: *ASME 2009 28th International Conference on Ocean, Offshore and Arctic Engineering*. American Society of Mechanical Engineers. 2009, pp. 55–67.

[22] DE Jiang and Emily A Carter. “Diffusion of interstitial hydrogen into and through bcc Fe from first principles”. In: *Physical Review B* 70.6 (2004), p. 064102.

[23] P Sofronis and RM McMeeking. “Numerical analysis of hydrogen transport near a blunting crack tip”. In: *Journal of the Mechanics and Physics of Solids* 37.3 (1989), pp. 317–350.

[24] L Jemblie, V Olden, and OM Akselsen. “A coupled diffusion and cohesive zone modelling approach for numerically assessing hydrogen embrittlement of steel structures”. In: *International Journal of Hydrogen Energy* (2017).

[25] AJ Kumnick and HH Johnson. “Deep trapping states for hydrogen in deformed iron”. In: *Acta Metallurgica* 28.1 (1980), pp. 33–39.

[26] Helmut Mehrer. *Diffusion in solids: fundamentals, methods, materials, diffusion-controlled processes*. Vol. 155. Springer Science & Business Media, 2007.

[27] AHM Krom, RWJ Koers, and A Bakker. “Hydrogen transport near a blunting crack tip”. In: *Journal of the Mechanics and Physics of Solids* 47.4 (1999), pp. 971–992.

[28] Joshua Pelleg. *Mechanical properties of materials*. Vol. 190. Springer Science & Business Media, 2012.

[29] Harshal Patil. “Introduction to fracture Mechanics”. Presentation in Mechanical System Design 13ME63R26. 2014.

[30] A_A_ Wells. “Unstable crack propagation in metals: cleavage and fast fracture”. In: *Proceedings of the crack propagation symposium*. Vol. 1. 84. 1961.

[31] *British Standard BS7448-4, Fracture mechanics toughness tests - Part 4: Method for determination of fracture resistance curves and initiation values for stable crack extension in metallic materials*. 1997.

[32] Karhaloo B. Milne I. Ritchie R.O. *Comprehensive Structural Integrity, Volume 1-10*. Elsevier, 2003.

[33] Andrew Seagraves and Raúl Radovitzky. “Advances in cohesive zone modeling of dynamic fracture”. In: *Dynamic failure of materials and structures*. Springer, 2009, pp. 349–405.

[34] Donald S Dugdale. “Yielding of steel sheets containing slits”. In: *Journal of the Mechanics and Physics of Solids* 8.2 (1960), pp. 100–104.

[35] Grigory Isaakovich Barenblatt. “The mathematical theory of equilibrium cracks in brittle fracture”. In: *Advances in applied mechanics* 7 (1962), pp. 55–129.

[36] Arne Hillerborg, Mats Modéer, and P-E Petersson. “Analysis of crack formation and crack growth in concrete by means of fracture mechanics and finite elements”. In: *Cement and concrete research* 6.6 (1976), pp. 773–781.

[37] Alan Needleman. “A continuum model for void nucleation by inclusion debonding”. In: *Journal of applied mechanics* 54.3 (1987), pp. 525–531.

[38] Viggo Tvergaard and John W Hutchinson. “The relation between crack growth resistance and fracture process parameters in elastic-plastic solids”. In: *Journal of the Mechanics and Physics of Solids* 40.6 (1992), pp. 1377–1397.

[39] Karl-Heinz Schwalbe, Ingo Scheider, and Alfred Cornec. *Guidelines for applying cohesive models to the damage behaviour of engineering materials and structures*. Springer Science & Business Media, 2012.

[40] I Scheider and W Brocks. “Simulation of cup-cone fracture using the cohesive model”. In: *Engineering Fracture Mechanics* 70.14 (2003), pp. 1943–1961.

[41] Ingo Scheider. “Cohesive model for crack propagation analyses of structures with elastic–plastic material behavior Foundations and implementation”. In: *GKSS research center, Geesthacht* (2001).

[42] Philippe H Geubelle and Jeffrey S Baylor. “Impact-induced delamination of composites: a 2D simulation”. In: *Composites Part B: Engineering* 29.5 (1998), pp. 589–602.

[43] Lofti Hamitouche, Mostapha Tarfaoui, and Alain Vautrin. “An interface debonding law subject to viscous regularization for avoiding instability: application to the delamination problems”. In: *Engineering Fracture Mechanics* 75.10 (2008), pp. 3084–3100.

[44] Haiyang Yu et al. “Viscous regularization for cohesive zone modeling under constant displacement: An application to hydrogen embrittlement simulation”. In: *Engineering Fracture Mechanics* 166 (2016), pp. 23–42.

[45] YF Gao and AF Bower. “A simple technique for avoiding convergence problems in finite element simulations of crack nucleation and growth on cohesive interfaces”. In: *Modelling and Simulation in Materials Science and Engineering* 12.3 (2004), p. 453.

[46] S Serebrinsky, EA Carter, and M Ortiz. “A quantum-mechanically informed continuum model of hydrogen embrittlement”. In: *Journal of the Mechanics and Physics of Solids* 52.10 (2004), pp. 2403–2430.

[47] DE Jiang and Emily A Carter. “First principles assessment of ideal fracture energies of materials with mobile impurities: implications for hydrogen embrittlement of metals”. In: *Acta materialia* 52.16 (2004), pp. 4801–4807.

[48] ED Hondros and MP Seah. “The theory of grain boundary segregation in terms of surface adsorption analogues”. In: *Metallurgical and Materials Transactions A* 8.9 (1977), pp. 1363–1371.

[49] Antonio Alvaro, Vigdis Olden, and Odd Magne Akselsen. “3D cohesive modelling of hydrogen embrittlement in the heat affected zone of an X70 pipeline steel”. In: *international journal of hydrogen energy* 38.18 (2013), pp. 7539–7549.

[50] Yongwon Lee and Richard P Gangloff. “Measurement and modeling of hydrogen environment–assisted cracking of ultra-high-strength steel”. In: *Metallurgical and Materials Transactions A* 38.13 (2007), pp. 2174–2190.

[51] Det Norske Veritas. “Cathodic protection design”. In: *Recommended Practice DNV-RP-B401* (2005).

[52] Vigdis Olden, Anders Senumstad Hauge, Odd Magne Akselsen, et al. “The influence of plastic strain on the effective hydrogen diffusion coefficient and trapping in base metal and weld simulated heat affected zone of an X70 pipeline steel”. In: *The Twenty-second International Offshore and Polar Engineering Conference*. International Society of Offshore and Polar Engineers. 2012.

[53] *British Standard BS7448-1, Fracture mechanics toughness tests - Part 1: Method for determination of KIc, critical CTOD and critical J values of metallic materials*. 1991.

[54] Philipe Maincon. *Cohesive Zone Elements*. Tech. rep. SINTEF A26585, 2017.

[55] Sunny Islam. “Parameter study of the cohesive zone model”. Unbublished internship report at Norwegian University of Science and Technology. 2015.

[56] Antonio Alvaro, Vigdis Olden, and Odd Magne Akselsen. “3D cohesive modelling of hydrogen embrittlement in the heat affected zone of an X70 pipeline steel–Part II”. In: *International Journal of Hydrogen Energy* 39.7 (2014), pp. 3528–3541.

[57] Philipe Maincon Antonio Alvaro and Vigdis Osen. *FEM formulation for mass diffusion through UMATHT subroutine*. Tech. rep. SINTEF A26585, 2015.

[58] Magnus Skjellerudsveen et al. “Effect of Microstructure and Temperature on HydrogenDiffusion and Trapping in X70 grade Pipeline Steel and itsWeldments”. In: *EuroCorr 2010, Moskva*. 2010.

[59] Chris San Marchi, BP Somerday, and SL Robinson. “Permeability, solubility and diffusivity of hydrogen isotopes in stainless steels at high gas pressures”. In: *International Journal of Hydrogen Energy* 32.1 (2007), pp. 100–116.

[60] GJ Thomas. *Hydrogen trapping in FCC metals*. Tech. rep. Sandia National Labs., Livermore, CA (USA), 1980.

[61] John P Hirth. “Effects of hydrogen on the properties of iron and steel”. In: *Metallurgical Transactions A* 11.6 (1980), pp. 861–890.

[62] Richard P Gangloff and Brian P Somerday. *Gaseous Hydrogen Embrittlement of Materials in Energy Technologies: Mechanisms, Modelling and Future Developments*. Elsevier, 2012.

[63] I Scheider, M Pfuff, and W Dietzel. “Simulation of hydrogen assisted stress corrosion cracking using the cohesive model”. In: *Engineering Fracture Mechanics* 75.15 (2008), pp. 4283–4291.

**

A. Experiments

A.1 Position of triple point in the B-samples

To make sure that the notch was placed correct in relation to the triple point, were the surface of the B samples overlooked in LOM:

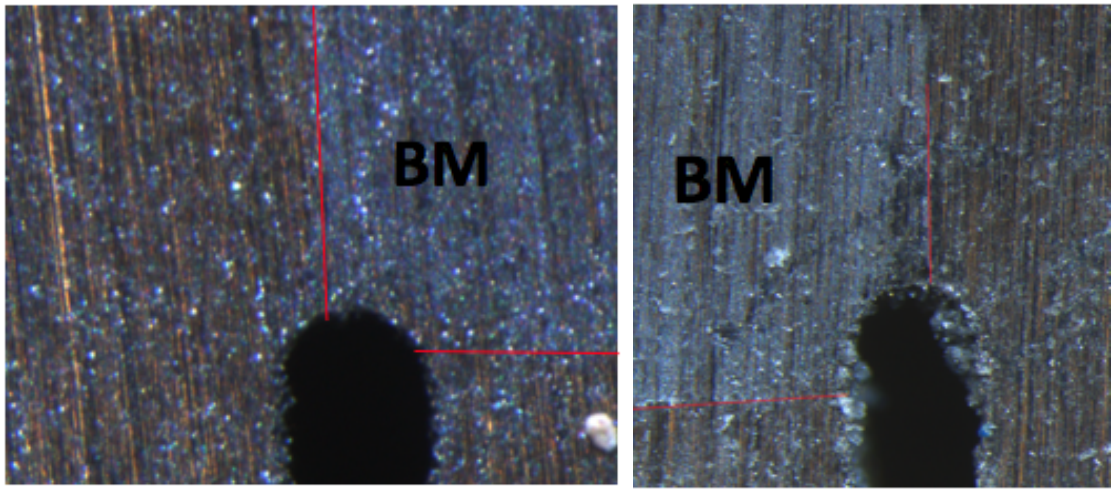

(a) (b)

Figure A.1: Triple point of samples studied in LOM, Sample B3 on the left and sample B4 on the right.

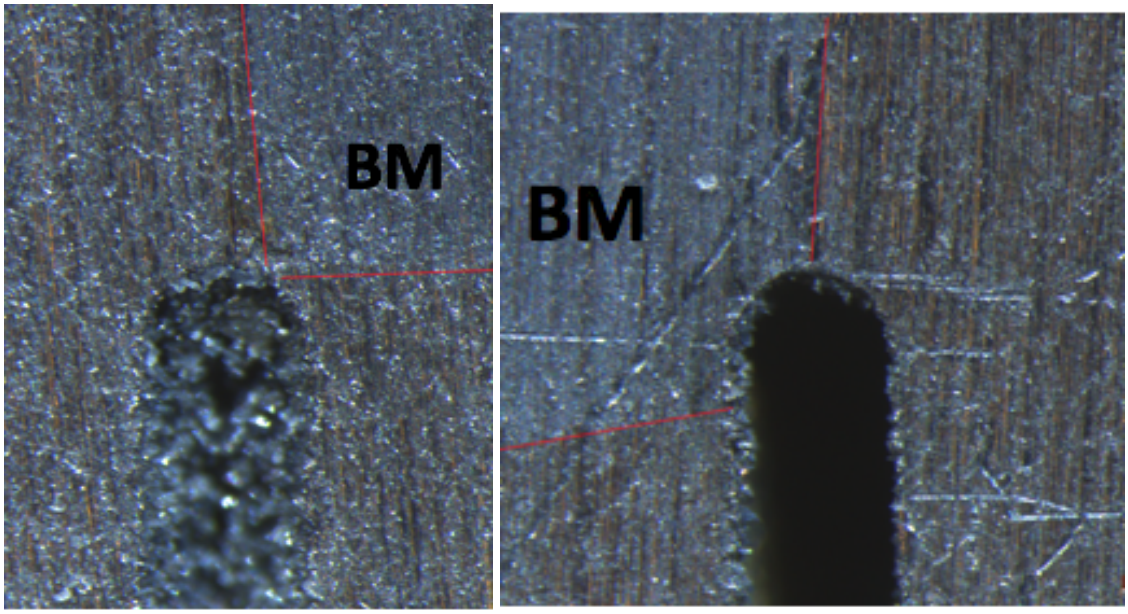

(a) (b)

Figure A.2: Triple point of samples studied in LOM, Sample B6 on the left and sample B9 on the right.

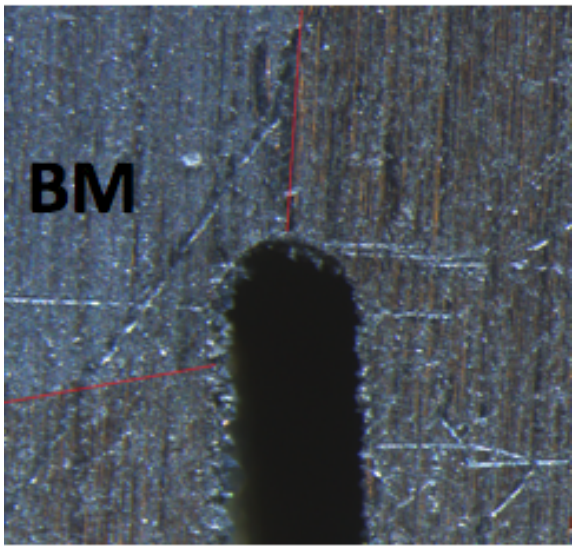

Figure A.3: B10 triple point studied in LOM

A.2 Measurements

The C(T) specimens are measured as indicated in figure A.4. The measurements are done as explained in Bjaaaland‘s [4] master thesis. All the dimensions except for the thickness were measured in a light microscope. The thickness was after discussion with a test engineer measured by a micrometer at one point instead of in three points with the light-microscope as explained in Bjaaland‘s [4] thesis. The different dimensions are measured

from the bottom of the specimen and up to the dotted lines, except for the thickness which was measured at the expected crack path. The measured dimensions are shown in table A.1 and A.2.

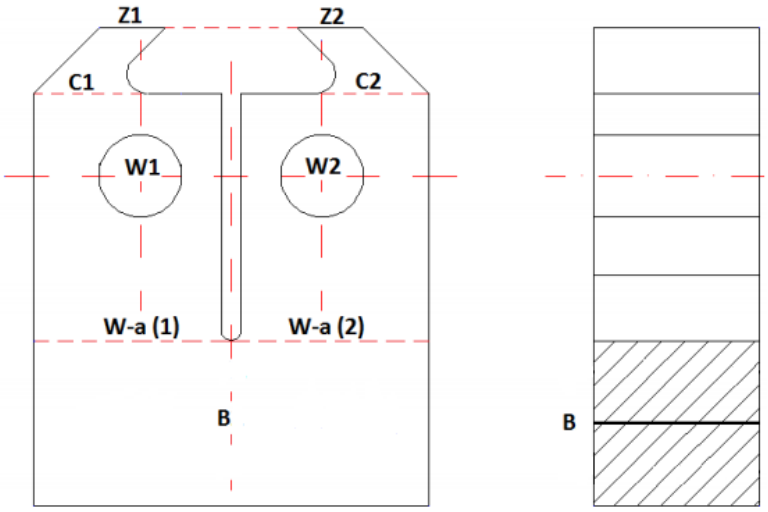

Figure A.4: C(T) specimen geometry with indicated measured dimensions [4].

Dim. [mm]	**A9**	**A10**	**A11**	**A12**	**A13**	**A14**	**A15**
B	**2.519**	**2.510**	**2.523**	**2.519**	**2.515**	**2.523**	**2.502**
W_1	5.013	5.008	4.998	4.995	5.000	4.985	5.013
W_2	4.988	4.988	4.975	4.993	4.995	4.980	5.025
W	**5.000**	**4.998**	**4.986**	**4.994**	**4.998**	**4.983**	**5.019**
$W - a_1$	2.510	2.540	2.500	2.500	2.490	2.510	2.57
$W - a_2$	2.495	2.510	2.460	2.515	2.490	2.520	2.515
W-a	**2.503**	**2.525**	**2.480**	**2.508**	**2.490**	**2.520**	**2.543**
a	**2.498**	**2.473**	**2.506**	**2.486**	**2.508**	**2.468**	**2.476**
C_1	6.250	6.265	6.230	6.235	6.225	6.250	6.270
C_2	6.225	6.250	6.215	6.240	6.230	6.225	6.255
C	**6.253**	**6.258**	**6.223**	**6.238**	**6.228**	**6.253**	**6.263**
Z_1	0.990	0.995	0.990	1.000	0.995	1.000	0.990
Z_2	0.980	0.990	1.000	1.000	0.995	1.000	0.990
Z	**0.985**	**0.993**	**0.995**	**1.000**	**0.995**	**1.000**	**0.998**

Table A.1: Measured dimensions for A samples, before testing.

Dim. [mm]	B3	B4	B6	B9	B10
B	**2.496**	**2.512**	**2.500**	**2.517**	**2.525**
W_1	5.015	4.993	4.993	4.980	4.980
W_2	4.955	5.020	4.903	4.978	4.833
W	**4.985**	**5.006**	**4.948**	**4.979**	**4.906**
$W - a_1$	2.550	2.460	2.600	2.515	2.570
$W - a_2$	2.505	2.580	2.505	2.530	2.500
W-a	**2.528**	**2.520**	**2.553**	**2.523**	**2.535**
a	**2.458**	**2.486**	**2.395**	**2.456**	**2.371**
C_1	6.280	6.220	6.340	6.240	6.320
C_2	6.230	6.300	6.225	6.275	6.250
C	**6.255**	**6.250**	**6.283**	**6.258**	**6.285**
Z_1	0.995	1.000	0.995	0.995	0.990
Z_2	1.005	0.995	1.00	1.010	0.990
Z	1.000	0.938	0.998	1.003	0.990

Table A.2: Measured dimensions for B samples, before testing.

The initial crack length a_0 and the stable crack growth Δa was measured after testing in accordance with standard BS. a_i and δa_i is the distance from the center of the holes to the start of the fracture surface and to the end of the heat tinting respectively, as shown in figure A.5. b was measured where the thickness of the specimens were smallest along the fracture surface. a_i and Δa_i was found by measuring the distance from the top (C shown in figure A.4 and then extract the distance from the top (C) to the center of the holes W $(C - W)$.

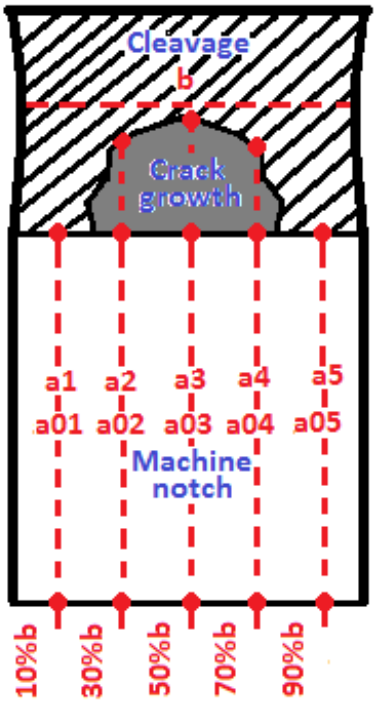

Figure A.5: Description on the initial crack length and stable crack growth procedure.

Dim. [mm]	**A9**	**A10**	**A11**	**A12**	**A13**	**A14**	**A15**
b	**2.390**	**2.395**	**2.400**	**2.375**	**2.375**	**2.395**	**2.27**
a_{01}	2.533	2.505	2.582	2.584	2.53	2.571	2.527
a_{02}	2.573	2.555	2.602	2.544	2.58	2.626	2.597
a_{03}	2.573	2.570	2.622	2.584	2.55	2.541	2.622
a_{04}	2.648	2.520	2.592	2.569	2.565	2.601	2.612
a_{05}	2.543	2.515	2.582	2.574	2.57	2.536	2.582
a_0	**2.583**	**2.539**	**2.599**	**2.569**	**2.561**	**2.581**	**2.596**
Δa_1	[-]	[-]	[-]	0	0	0	0
Δa_2	[-]	[-]	[-]	0.335	0.645	0.98	0.845
Δa_3	[-]	[-]	[-]	0.575	0.775	1.165	0.975
Δa_4	[-]	[-]	[-]	0.52	0.35	0.515	0.725
Δa_5	[-]	[-]	[-]	0	0	0	0
Δa	[-]	[-]	[-]	**0.358**	**0.443**	**0.665**	**0.636**

Table A.3: Measured dimensions for A samples, post, testing.

Dim. [mm]	**B3**	**B4**	**B6**	**B9**	**B10**
b	**1.975**	**1.955**	**1.615**	**1.485**	**1.555**
a_{01}	2.540	2.491	2.531	2.721	2.501
a_{02}	2.535	2.480	2.531	2.711	2.491
a_{03}	2.520	2.466	2.521	2.736	2.521
a_{04}	2.490	2.481	2.516	2.801	2.516
a_{05}	2.500	2.476	2.531	2.821	2.506
a_0	**2.516**	**2.478**	**2.525**	**2.755**	**2.508**

Table A.4: Measured initial crack lengths for B samples, post testing.

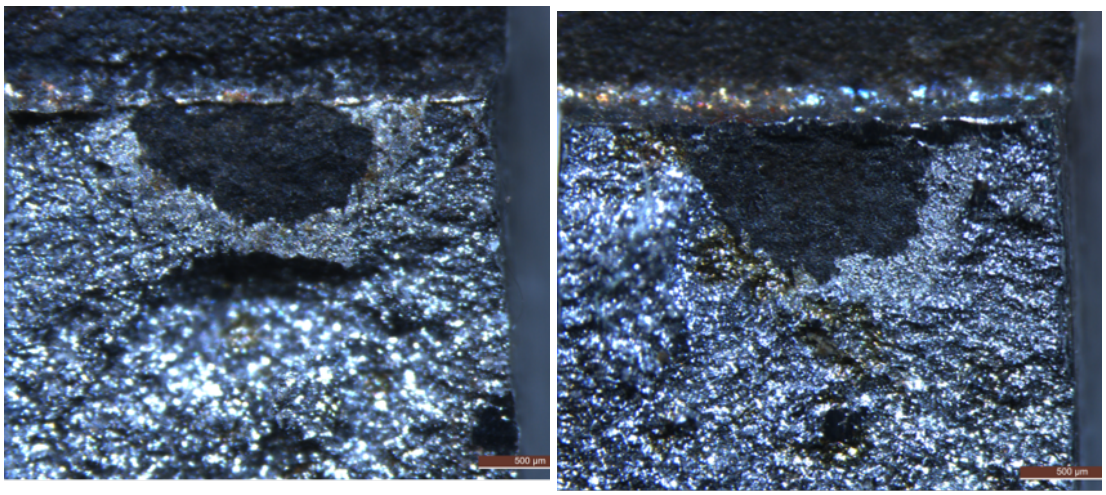

(a) (b)

Figure A.6: Stable crack growth on sample A12 on the left and A13 on the right (black area).

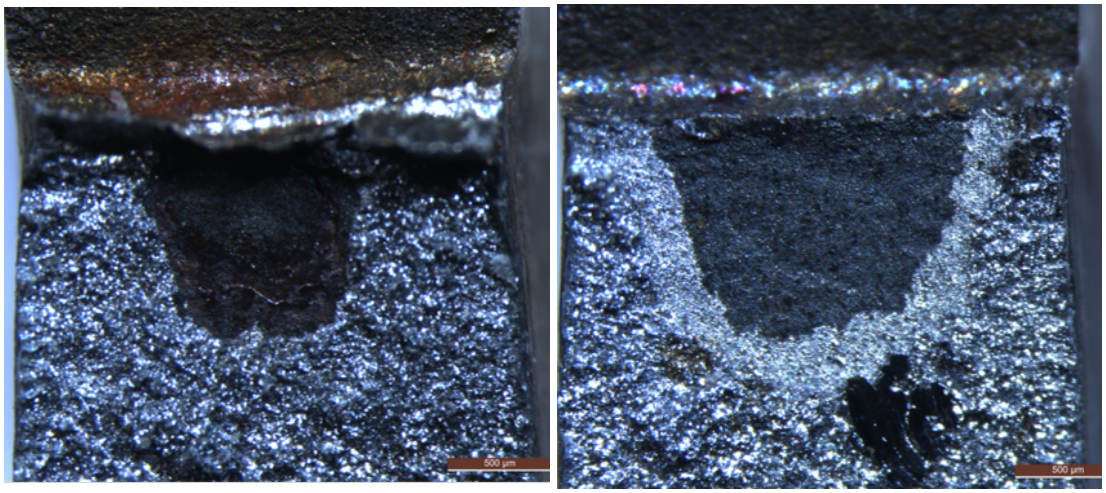

(a) (b)

Figure A.7: Stable crack growth on sample A14 on the left and A15 on the right (black area).

$$CTOD_{corr} = \frac{K_I^2(1-\nu^2)}{2ER_{p0.2}} + \frac{0.54\Delta a + 0.46(W-a_0)}{0.54(a_0+\Delta a)+0.46W+(W_t-W)+z} * V_p \tag{A.1}$$

A.3 Raw data processing

The displacement and CMOD was corrected graphically to fit the steepest part of the curve with the origin as shown in figure A.8a to A.13b and figure A.14a to A.17 respectively. A relation between the displacement and CMOD was found by curve fitting by Eq. A.4.

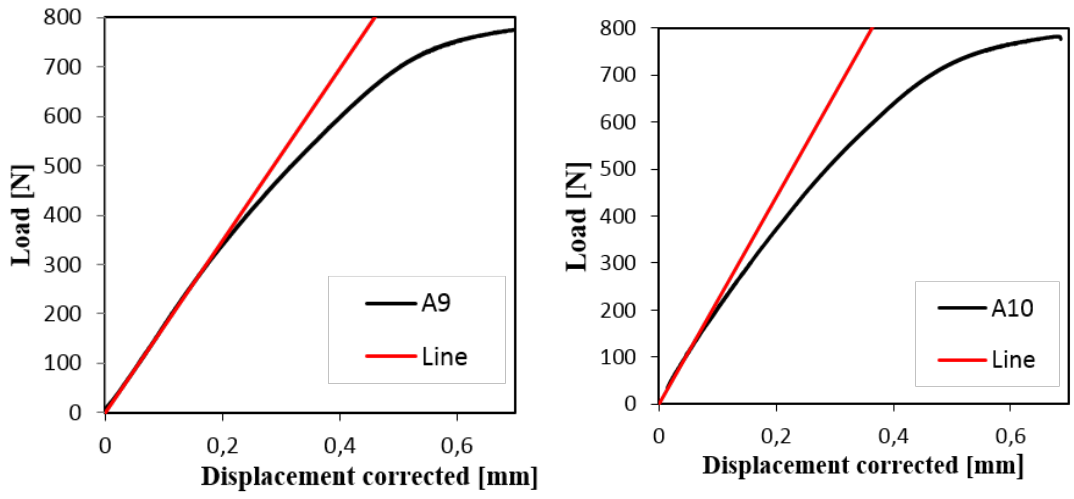

(a) (b)

Figure A.8: Load-displacement corrected for sample A9 on the left and sample A10 on the right.

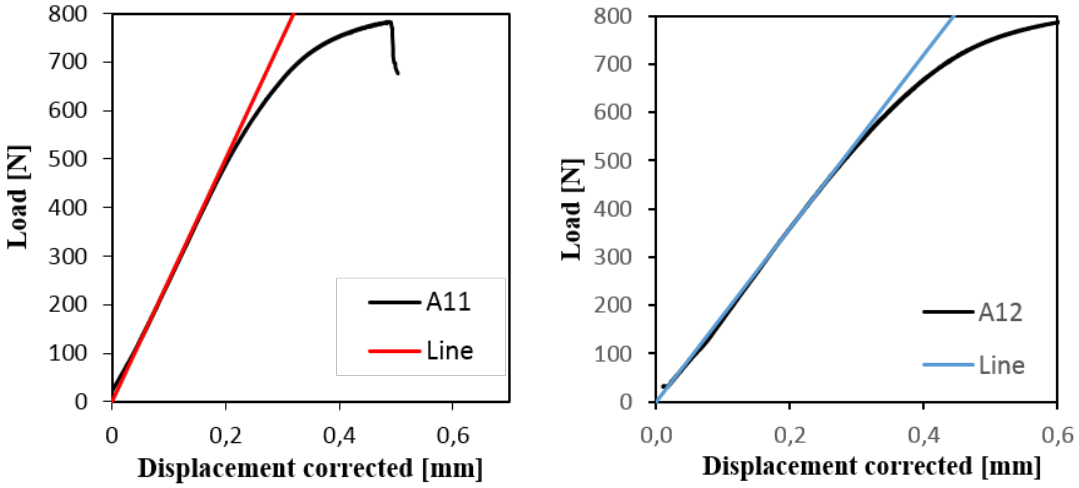

(a) (b)

Figure A.9: Load-displacement corrected for sample A11 on the left and sample A12 on the right.

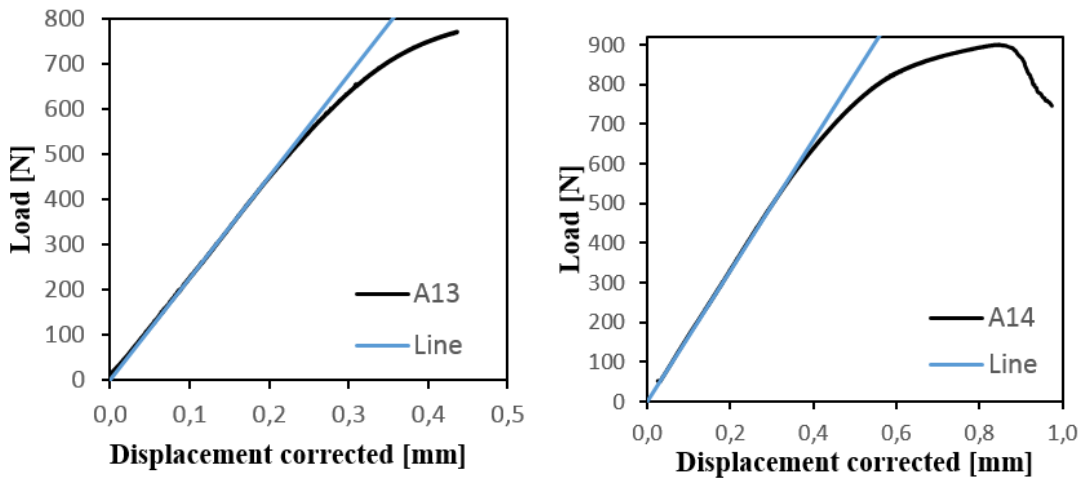

(a) (b)

Figure A.10: Load-displacement corrected for sample A13 on the left and sample A14 on the right.

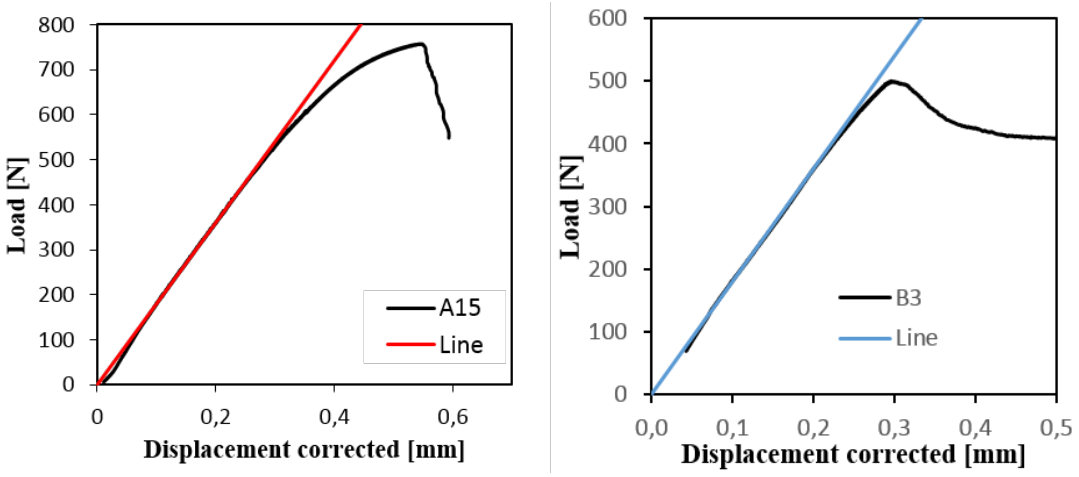

(a) (b)

Figure A.11: Load-displacement corrected for sample A15 on the left and sample B3 on the right.

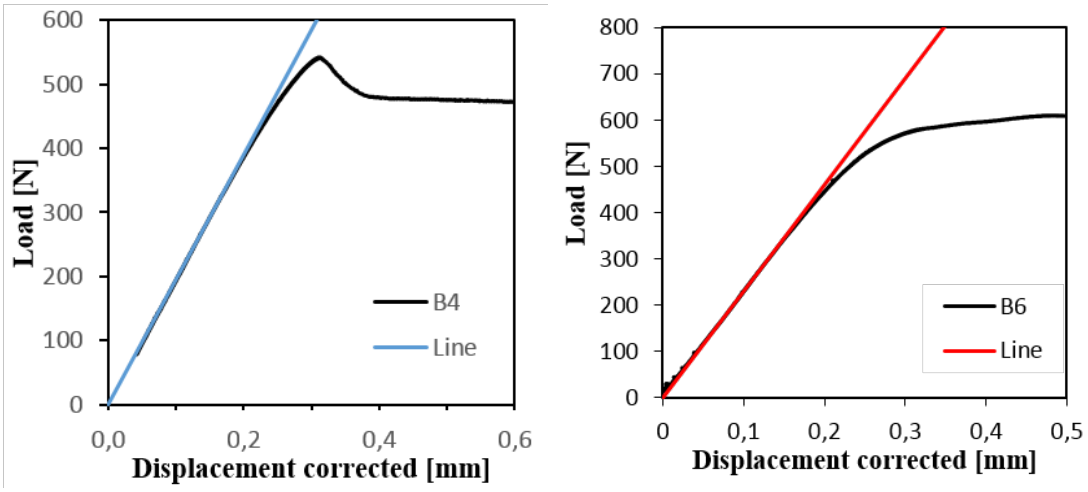

(a) (b)

Figure A.12: Load-displacement corrected for sample B4 on the left and sample B6 on the right.

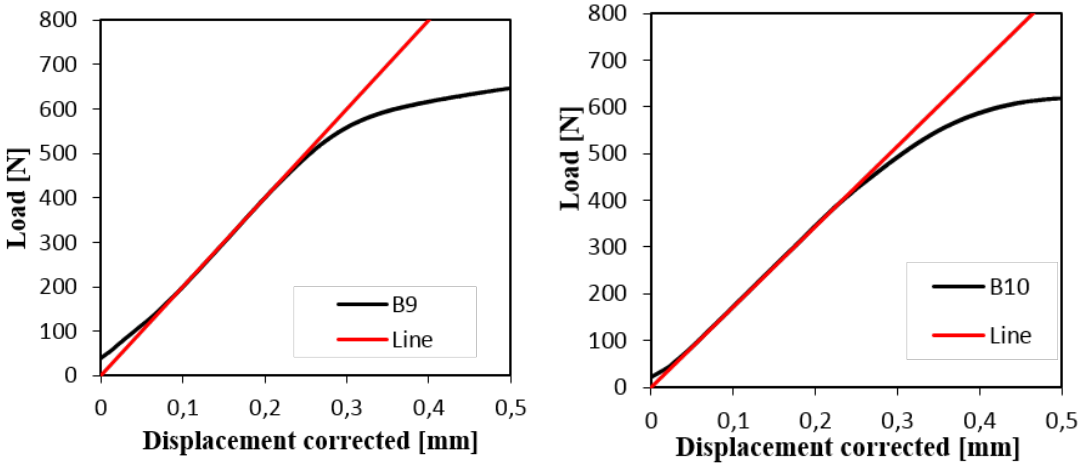

(a) (b)

Figure A.13: Load-displacement corrected for sample B9 on the left and sample B10 on the right.

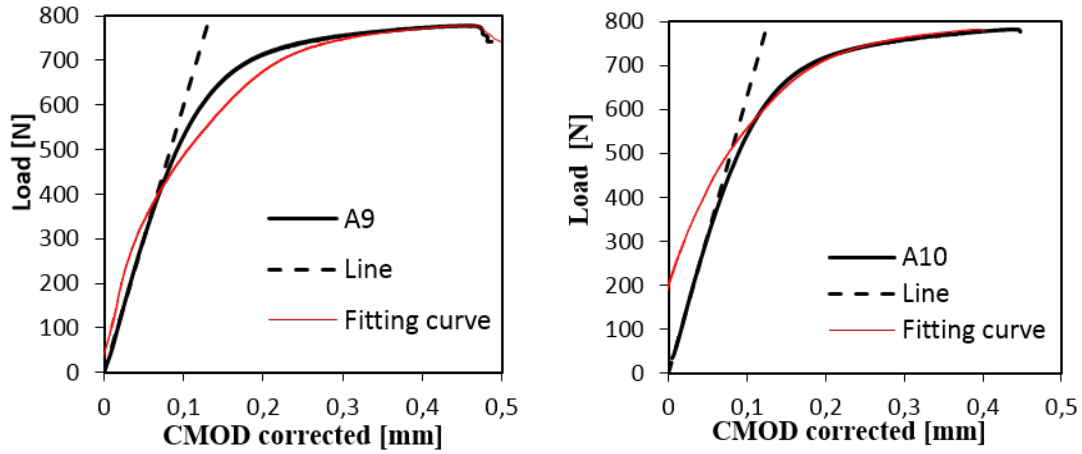

(a) (b)

Figure A.14: Load-CMOD corrected for sample A9 on the left and sample A10 on the right.

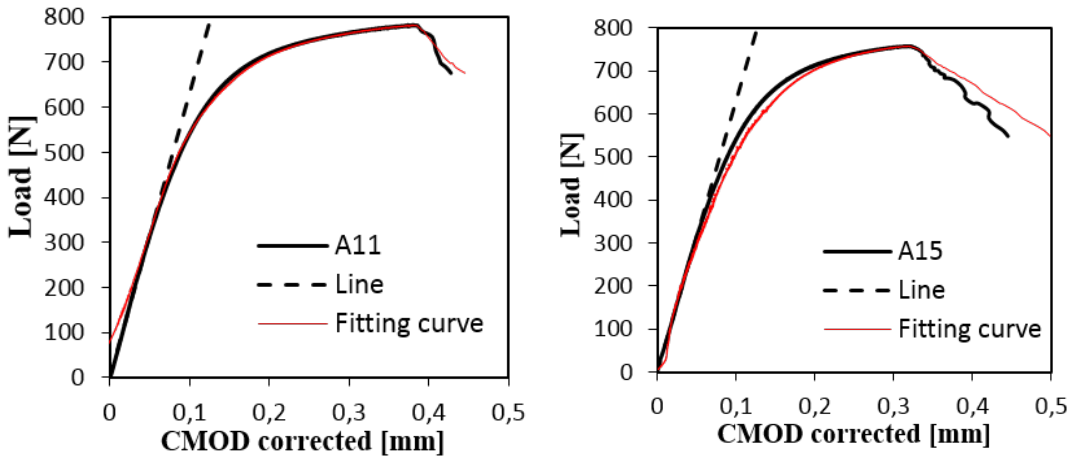

(a) (b)

Figure A.15: Load-CMOD corrected for sample A11 on the left and sample A15 on the right.

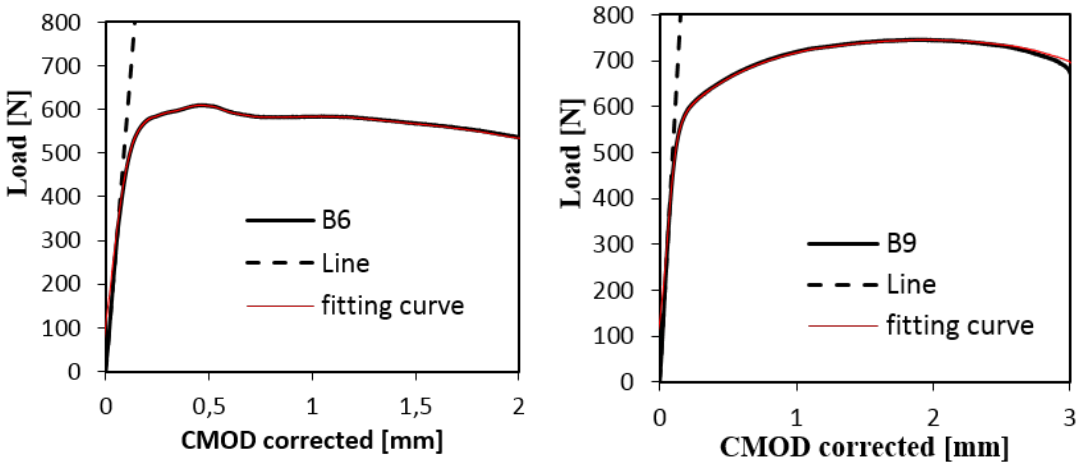

(a) (b)

Figure A.16: Load-CMOD corrected for sample B6 on the left and sample B9 on the right.

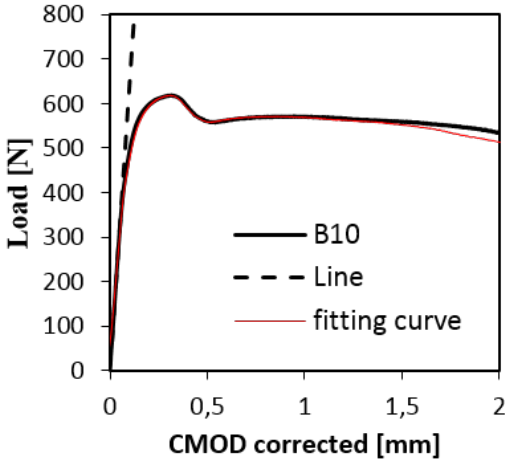

Figure A.17: Load-CMOD corrected for sample B10.

	A9	A10	A11	A12	A13	A14	A15	**Av.**
$slope_{Disp}$	1740	2200	2500	1800	2250	1800	1650	[-]
$slope_{CMOD}$	6000	6300	6300	[-]	[-]	[-]	6300	[-]
A	1.25	1.13	1.44	[-]	[-]	[-]	1.37	1.41
B	-0.005	-0.02	-0.009	[-]	[-]	[-]	-0.01	-0.01

Table A.5: Tabulated curve values for the A samples.

Note, A9 and A10 are not included in the A and B average in table A.5 because of bad fit with the CMOD curve, in figure A.14a and A.14b.

	B3	B4	B6	B9	B10	**Av.**
$slope_{Disp}$	1800	1950	2300	2000	1720	[-]
$slope_{CMOD}$	[-]	[-]	5700	5250	6400	[-]
A	[-]	[-]	1.55	1.55	1.35	**1.483**
B	[-]	[-]	-0.025	-0.031	-0.01	**-0.022**

Table A.6: Tabulated curve values for the B samples.

The plastic displacement d_p was calculated by:

$$d_p = displacement_{corr} - \frac{Load}{slope_{disp}} \tag{A.2}$$

The plastic CMOD V_p was calculated by:

$$V_p = CMOD_{corr} - \frac{Load}{slope_{CMOD}} \tag{A.3}$$

The fitting curves was constructed by Eq.:

$$CMOD_{displacement} = displacement_{CMOD} * \frac{Load}{slope_{disp}} \tag{A.4}$$

Where:

$$displacement_{CMOD} = displacement_{corrected} * A + B \tag{A.5}$$

The average of the factors calculated by the relation between the plastic CMOD, V_p and the plastic displacement d_p were found:

Sample	V_p [mm]	d_p [mm]	Factor
A9	0.33	0.29	1.17
A10	0.32	0.33	0.98
A11	0.23	0.17	1.47
A15	0.20	0.13	1.58
Average	[-]	[-]	**1.30**
B6	0.38	0.23	1.63
B9	1.83	1.20	1.53
B10	0.22	0.14	1.53
Average	[-]	[-]	**1.57**

Table A.7: The factor calculated from the relation between plastic CMOD and plastic displacement at maximum load.

Sample	V_p [mm]	d_p [mm]	Factor
A9	0.35	0.29	1.17
A10	0.33	0.33	0.98
A11	0.26	0.18	1.46
A15	0.21	0.14	1.56
Average	[-]	[-]	**1.29**

Table A.8: The factor calculated from the relation between plastic CMOD and plastic displacement at $P_{max} - 6N$

Sample	V_p [mm]	d_p [mm]	Factor
A9	0.36	0.32	1.14
A11	0.29	0.20	1.44
A15	0.23	0.16	1.48
Average	[-]	[-]	**1.35**

Table A.9: The factor calculated from the relation between plastic CMOD and plastic displacement at $P_{max} - 36N$

Sample	V_p [mm]	d_p [mm]	Factor
A11	0.32	0.23	1.38
A15	0.29	0.21	1.36
Average	[-]	[-]	**1.37**

Table A.10: The factor calculated from the relation between plastic CMOD and plastic displacement at $P_{max} - 107N$

Sample	V_p [mm]	d_p [mm]	Factor
A15	0.36	0.29	1.24
Average	[-]	[-]	**1.24**

Table A.11: The factor calculated from the relation between plastic CMOD and plastic displacement at $P_{max} - 209N$

A.4 Discarded samples

Unfortunately several of the tests was judged invalid due to errors. The following tests were not usable for stable crack growth results due to insufficient heat tinting:

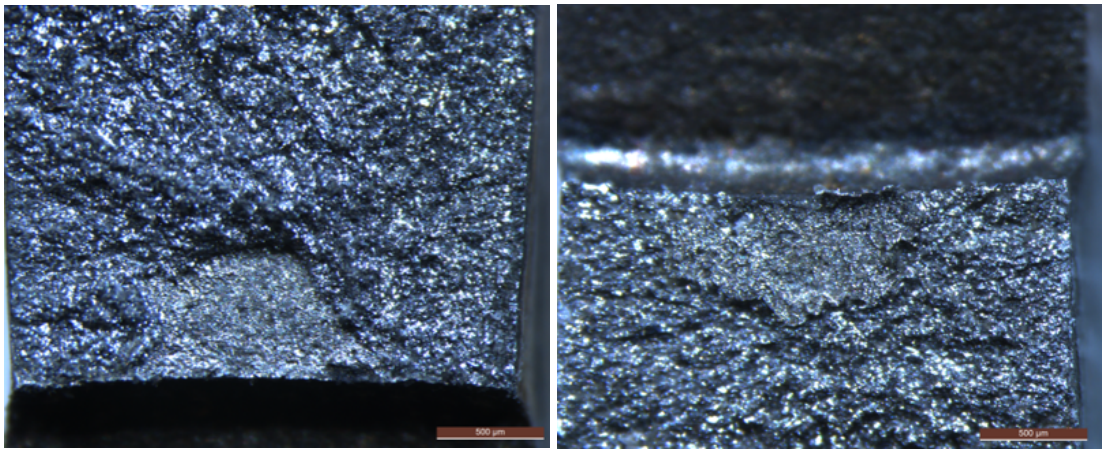

(a) (b)

Figure A.18: Insufficient heat tinting on sample A9 on the left and sample A10 on the right.

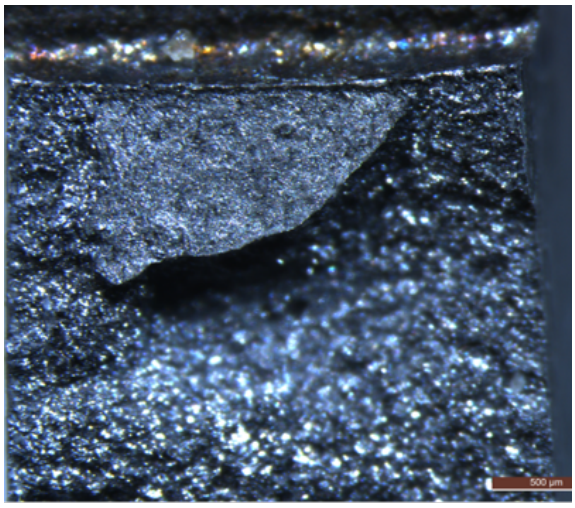

Figure A.19: Insufficient heat tinting on sample A11.

internal and surface flaws were also detected on some of the samples, which makes the results invalid:

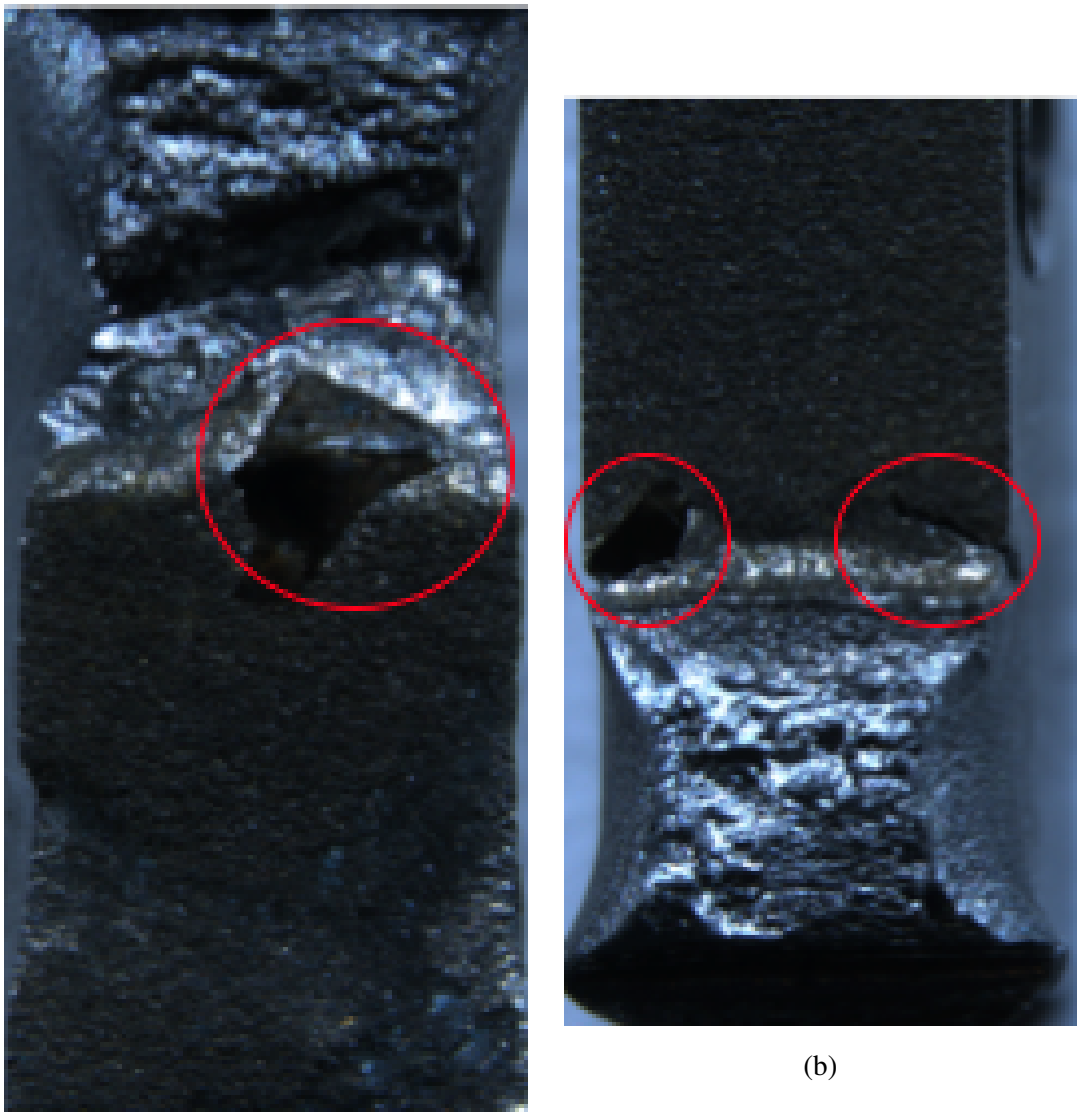

(a) (b)

Figure A.20: Slag inclusion, weld defects in sample B2 to the left and B11 to the right.

B. Simulations

B.1 FE-model

B.1.1 SENB FE-model

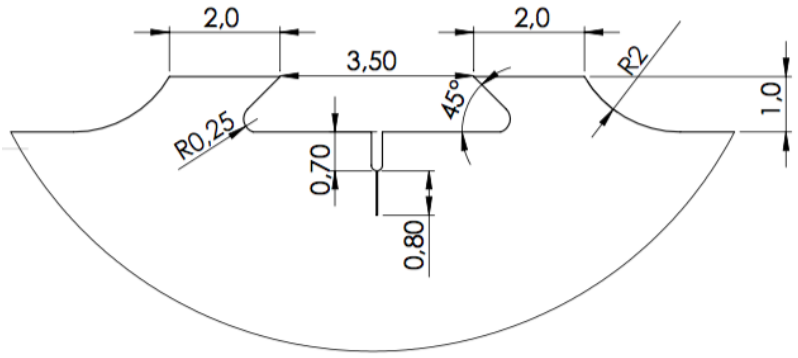

Figure B.1: SENB model

B.1.2 Dimensions of the sections in the FE-model

The dimensions of the sections in the FE-model are given in figure B.2. Only half of the model is shown because the section dimensions are symmetrical through the horizontal center axis. The dimensions are measured from the initial crack tip.

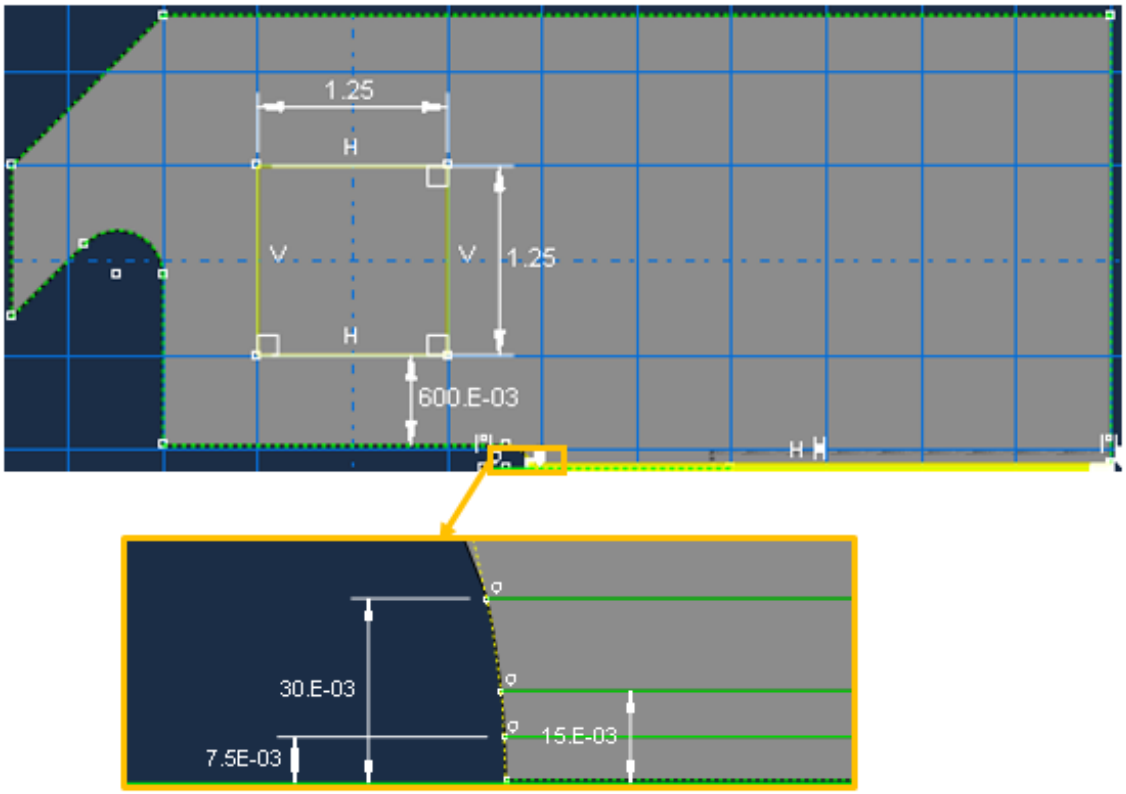

Figure B.2: dimensions on the sections in the FE-model

B.1.3 Mesh refinement dimensions

The dimensions of the mesh refinement are shown in figure B.3 and B.4. The refinement was divided into two steps. One coarse and one fine step. Figure B.3 shows the coarse step and figure B.4 shows the fine step refinement, measured from the initial crack tip. The mesh is refined from $0.15mm$ to $15\mu m$ in the coarse refinement step and refined to $7.5\mu m$ in the fine refinement step.

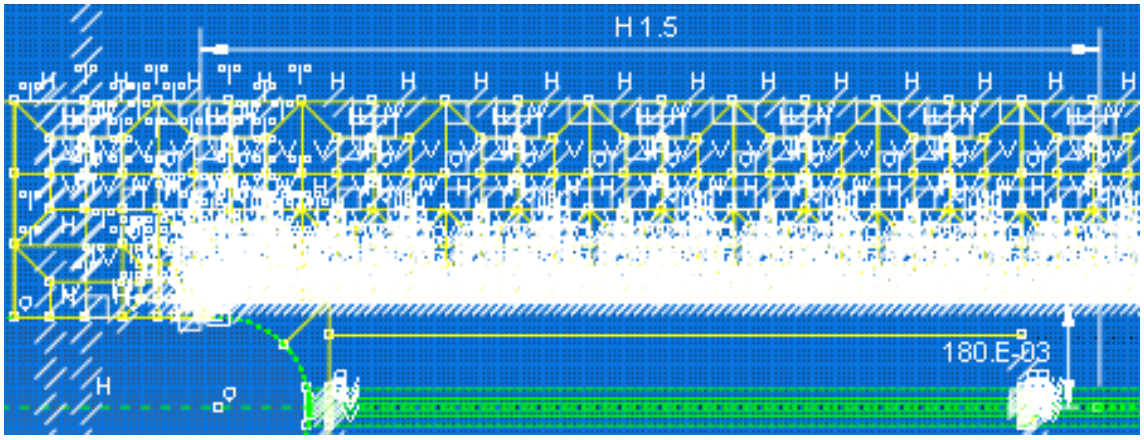

Figure B.3: Dimension of the coarse refinement step, measured from the initial crack tip.

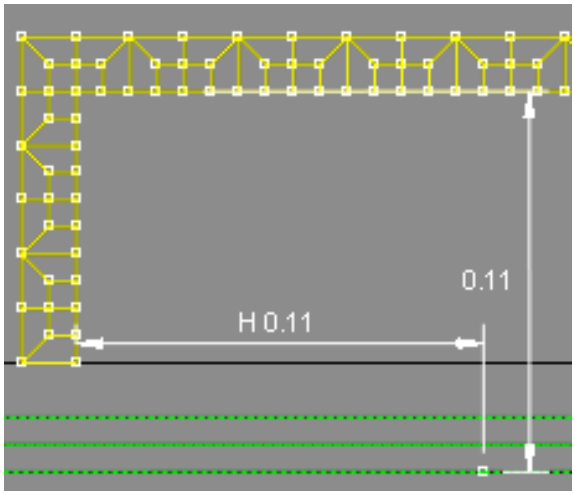

Figure B.4: Dimension of the fine refinement step, measured from the initial crack tip.

B.2 Changing the viscosity parameter

The TSL curve with different viscosity parameters in simulation 2 are given bellow. The red line is the theoretical TSL and the black dotted line is the simulation

B.2.1 BM

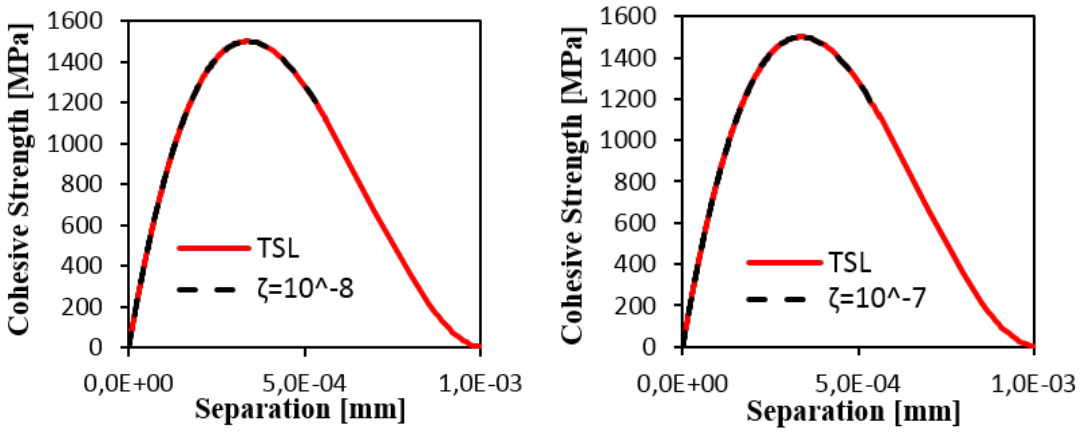

(a) (b)

Figure B.5: TSL curves simulation 2, changing viscosity parameter

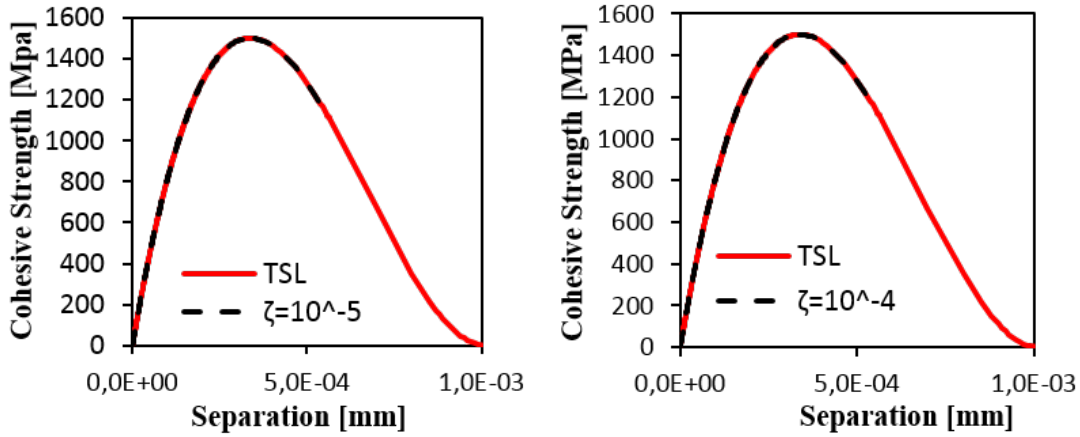

(a) (b)

Figure B.6: TSL curves simulation 2, changing viscosity parameter

B.2.2 Clad

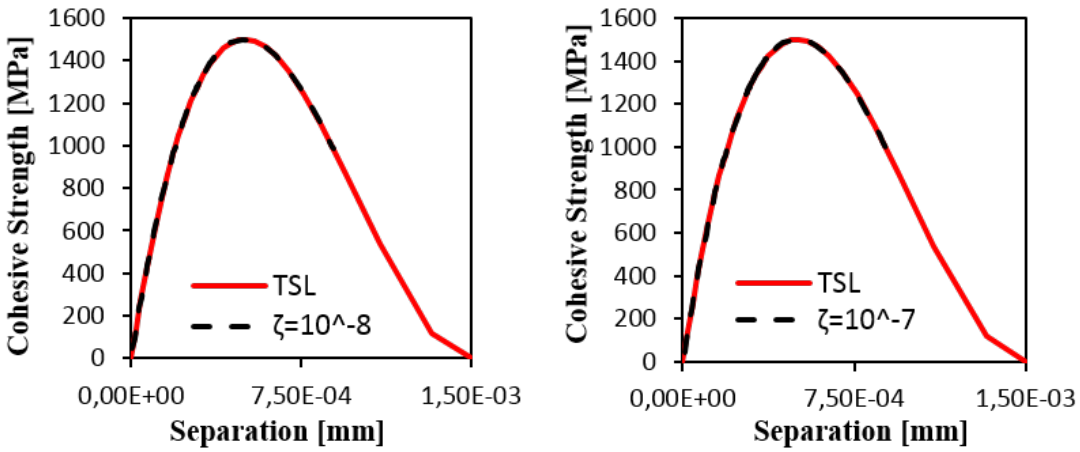

(a) (b)

Figure B.7: TSL curves simulation 5, changing viscosity parameter

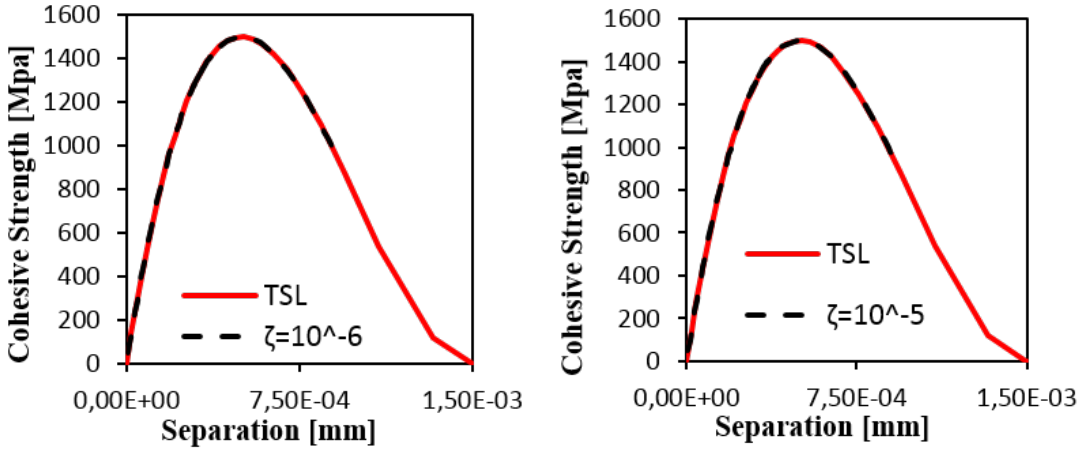

(a) (b)

Figure B.8: TSL curves simulation 5, changing viscosity parameter

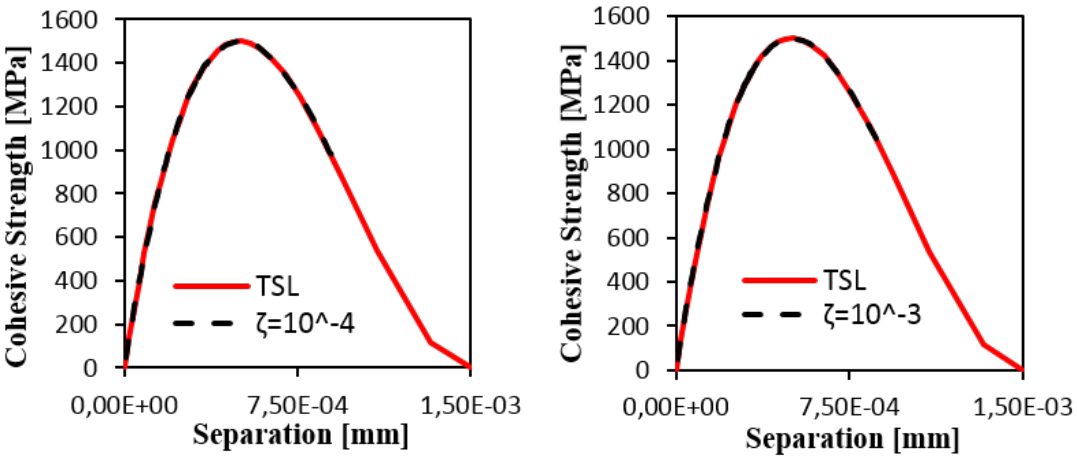

(a) (b)

Figure B.9: TSL curves simulation 5, changing viscosity parameter

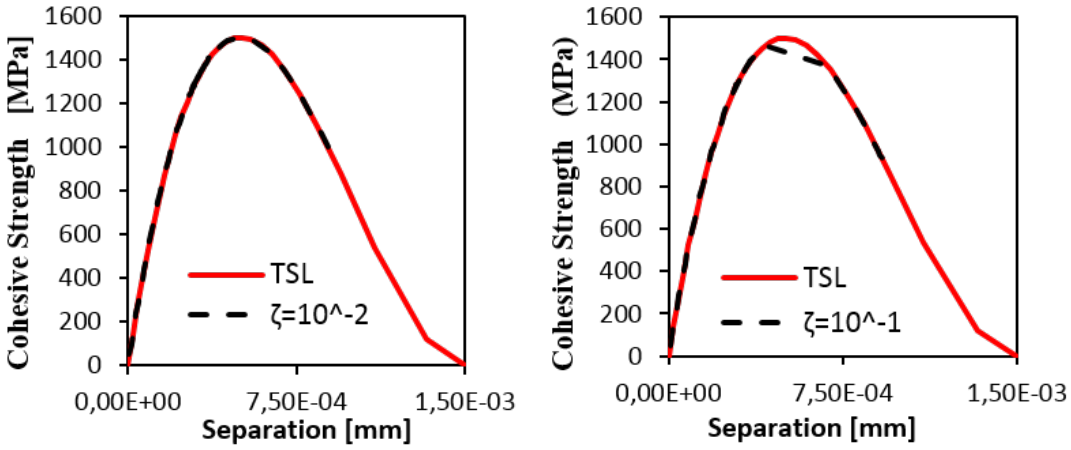

(a) (b)

Figure B.10: TSL curves simulation 5, changing viscosity parameter

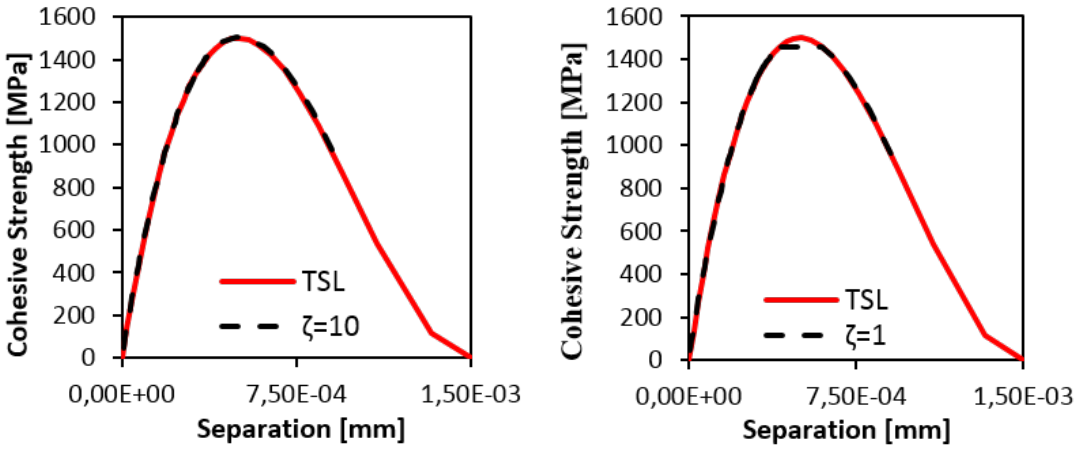

(a) (b)

Figure B.11: TSL curves simulation 5, changing viscosity parameter

B.3 Changing initial cohesive element stiffness

initial stiffness	Number of failed cohesive elements
10^6	1
$2 * 10^6$	1
$6.75 * 10^6$	4
$8.4 * 10^6$	4
10^7	6
$2 * 10^7$	4

Table B.1: Changing initial cohesive element stiffness, simulation 5